# CHAPTER 2. PERFORMANCE OF ARIFIYE OVERPASS REINFORCED EARTH WALLS DURING THE 1999 KOCAELI (TURKEY) EARTHQUAKE

## 1. INTRODUCTION

Reinforced soil structures, such as soil-nailed walls and mechanically stabilized embankments, have been shown to be feasible alternatives to conventional earth retaining structures. Recent years have seen an increased usage of these structures, and designs are becoming more aggressive with taller walls and a wider variety of reinforcing and facing materials. Although design methods for static conditions have been fairly well established, a particular concern is the gap in our knowledge regarding seismic performance and the relative lack of seismic design procedures. Current guidelines are very limited and based on generalized assumptions. No methods exist that have been grounded in actual performance during earthquakes or even detailed analytical study, such as numerical analysis. A primary disadvantage has been the scarcity of documented seismic field performance data for these structures. Further, although some centrifuge and shake table tests have been performed to simulate seismic loadings, these tests have been generalized and were not designed to yield specific results that could be used for the development of seismic design procedures. Thus, there is a critical need for case history analysis of these structures, combined with parametric numerical studies and model tests to fully understand their behavior and develop proper seismic design guidelines.

The behavior of reinforced soil structures under dynamic loading is not fully understood and current design methods are very limited due, in large part, to a lack of demonstrated field performance, an inadequate number of model tests, and few parametric numerical analyses. Current seismic design procedures typically involve what is essentially an extended version of static design methods. That is, both external and internal stability are analyzed in the same manner as for the static case, but with imposed pseudo-static lateral forces that are assumed

to adequately account for earthquake loading. Several current methods, with only minor differences in their approach, are used to estimate the dynamic component of lateral earth pressures induced by earthquake loading (AASHTO 1996; Whitman 1990). These procedures are all generalized pseudo-static limit equilibrium methods that do not represent actual earthquake loadings or account for certain aspects that influence behavior such as earthquake duration, frequency of motion, wall flexibility, and strain-dependent internal damping, etc. (In fact, the current FHWA guidelines suggest that current simplified procedures are not suitable for ground shaking levels above 0.3g, although many structures are located in areas expected to exceed these shaking levels). For instance, current approaches do not consider the seismic response of RSS's as composite, flexible structures, although our initial studies have shown that fundamental frequency of the structure relative to the characteristics of the base motion, along with duration of shaking are two key issues that should be addressed in the design procedures. Further, the flexibility of most reinforced soil systems allow them to undergo significant internal straining before they actually fail. It is a general observation that reinforced soil structures develop large displacements well before collapsing from reinforcement breakage and/or pullout under both static and dynamic loading conditions. In fact, permanent wall displacements can be the limiting criterion with respect to the serviceability of RSS's following earthquake loading. There are no current methods to predict RSS displacements. Current practice involves designing the RSS's with higher factors of safety and to tacitly rely on the extra capacity to limit displacements. A rigorous design method to predict seismically-induced permanent wall displacements is of obvious need.

Studies reported on the dynamic behavior of reinforced earth structures to date involve experimental work and numerical analysis. Experimental data from shake table and dynamic centrifuge model tests are available (Nova-Roessig and Sitar 1998). There is however, contradictory evidence from laboratory experiments. A main question is whether the dynamic failure modes of reinforced soil structures are large ductile displacements or collapse, with reinforcement pull-out/breakage. Shake table tests indicate that reinforced soil structures fail by the progressive development of a failure surface followed by reinforcement pullout and/or breakage (Fairless and Elms 1991; Matsuo et al. 1998). On the other hand, dynamic centrifuge tests reveal that large ductile movements are more predominant and reach

excessive levels well before the RSS actually collapses with reinforcement pull-out/breakage (Casey et al. 1991; Nova-Roessig and Sitar 1998). This study will attempt to shed light on these issues through numerical modeling analyses of these tests.

Several studies on the numerical analysis of dynamically loaded reinforced earth structures are also reported in the literature (Bathurst and Cai 1995; Bathurst and Hatami 1998a, 1998b, 1999; Cai and Bathurst 1995; Sakaguchi 1996). However, in these studies, it was not possible to corroborate the analysis results with actual measurements and/or performance observations. While it is recognized that numerical analyses were performed (Yogendrakumar and Bathurst 1990; Yogendrakumar et al. 1990) on earlier full-scale tests on reinforced soil structures that were shaken by explosives (Richardson et al. 1977), these tests are not considered the most appropriate for modeling for actual earthquake loadings.

Based on the current literature, there is an obvious gap in our knowledge and lack of consensus on the factors contributing to the dynamic behavior of reinforced soil systems. More research is needed clarify such issues. It is fortuitous that the RSS cases identified in the Turkey (Mitchell et al. 2000; Olgun and Martin 2003) and Taiwan earthquakes (Chen et al. 2000; Huang 2000) present a valuable opportunity to better understand the dynamic behavior of reinforced soil systems. The cases in Turkey have already provided significant information through initial field observations and preliminary analyses performed following 1999 earthquakes. Detailed analyses of these cases will improve our understanding of the dynamic behavior of such systems.

An earthquake of magnitude $M_w$=7.4 struck northwestern Turkey on August 17, 1999 resulting in widespread destruction and loss of life. Peak accelerations of up to 0.4g were measured in areas near the fault. Following the earthquake, the Virginia Tech research team traveled to Turkey to document the field performance of improved soil sites and mechanically-stabilized embankments (MSE) in the affected area. The findings indicated that MSE walls performed well in most cases. Of particular significance was the performance of two Reinforced Earth (RE) walls located at the site of the Arifiye Bridge overpass. These walls performed well and suffered little damage despite being subjected to strong ground shaking and large ground displacements.

The Arifiye Bridge is located along the Trans European Motorway that connects the two major cities Istanbul and Ankara. It is about 10 kilometers south of the town of Adapazari which suffered significant destruction during the earthquake (Bray and Stewart 2000). The site is located at the zone of energy release (N 40° 42 36.1 E 30° 22 55.7), as the surficial fault rupture passed directly beneath the site.

The bridge, which was constructed in 1988 and destroyed in the 1999 earthquake, consisted of four simply-supported spans resting on approach abutments and three mid-span pier supports. The two wing walls of the northern approach abutment were constructed using conventional Reinforced Earth (RE) with steel strips and compacted granular backfill. The abutment was supported on piles, and the RE walls and approach fills rested on a thin layer of fill overlying natural ground.

Four spans of the bridge collapsed in a "saw-tooth" manner due to lateral displacements of the piers and abutments, along with inadequate beam seat widths. However, the RE walls remained intact and experienced relatively little damage. The minor damage that occurred was associated with the foundation settlement and partial collapse of a culvert that ran beneath the wall and caused a loss of foundation support beneath one section of the wall. This resulted in separation and loss of interlocks between some of the lower wall panels which, in turn, caused some minor spillage of backfill material.

Because there are limited number of case histories regarding the seismic field performance of RE walls, the Virginia Tech team recognized the importance of this site and documented the behavior, including measurements of wall displacements and fault-related ground movements. The subsoil conditions and construction plans for the walls were also obtained during the investigation. Additional site investigations were performed at the site in October 2000 and shear wave velocity measurements were performed. These data made possible numerical analyses to predict the observed wall behavior.

This chapter provides a description of the RE walls and their seismic performance, along with the results of numerical analyses. As-built construction details of the reinforced soil structure are given as obtained from the Reinforced Earth® Company local office. Detailed site information pertinent to the performance of the RE walls is provided. Numerical analyses

were necessary to investigate the mechanisms leading to the observed behavior. Commercially available program FLAC (Fast Lagrangian Analysis of Continua) was used for these analyses (Itasca Consulting Group 2000). This is a finite difference program with explicit time integration scheme that can perform static and dynamic analysis of soil-structure systems. Pre-earthquake conditions of the structure are simulated by modeling the sequential construction procedure. Dynamic analyses were performed with the post-construction state of the model. General behavior of the model along with stresses and deformations were monitored throughout the analyses. The study is thought to provide insight into behavior of reinforced soil structures under seismic loading and yield data that can be used to improve our predictive capabilities and design procedures. Results are provided herein with full detail.

## 2. ARIFIYE BRIDGE OVERPASS

The Arifiye Bridge overpass, which was constructed in 1988 and destroyed in the 1999 Kocaeli Earthquake, consisted of four simply-supported spans resting on approach abutments and three mid-span pier supports. The northern approach embankment was constructed using Reinforced Earth ® technology. The reinforced concrete abutment was supported on piles, and the RE wing walls and approach fills rested on natural ground. The southern approach embankment was built with a conventional earth embankment with sloping sides. The site is located along the Trans European Motorway at the zone of energy release, as the surficial fault rupture passed directly beneath the site as seen in Figure 2-1. A schematic of the site, developed from an aerial photograph is shown in Figure 2-2. The figure shows the motorway and the location of the overpass along with the approach abutment structures. As seen, the site is directly adjacent to the zone of energy release as the fault rupture passed within a few meters of the northern abutment. Maximum horizontal and vertical ground displacements near the northern abutment were estimated at 350 cm and 45 cm, respectively. These movements were inferred from the measured displacement of a buried pipe that was ruptured by the fault about 50 m from the wall, as seen in Figure 2-3.

The wing walls of the northern approach abutment were constructed using Reinforced Earth ® (RE) technology. The bridge deck rests on a reinforced concrete abutment on pile

foundations. The northern approach ramp is about 145 meters long. Elevation difference between the ramp and the ground is about 9 meters at its highest. The RE walls were of conventional design, consisting of cruciform (and square at some locations), interlocking reinforced-concrete panels as facing elements. Facing panels of A-4 were used in most of the wall facing. This naming is company terminology where "A" represents the panel type and "4" is the number of steel strips per panel (Reinforced Earth Co. 2000). The side view of the structure is shown in Figure 2-4. There is a 4.8-meter wide reinforced-concrete culvert passing beneath the RE wall. The culvert is located in a creek channel that runs beneath the site. Suspected liquefaction in the creek-bed soils beneath this culvert, along with other foundation settlements, led to significant vertical movements in the wall.

Slip joints were used along the height of the wall on both sides of the concrete culvert. In addition, there was a slip joint between the RE wall and the reinforced concrete bridge abutment. The RE wall reached its maximum height of 10 meters near the culvert. At this section there is a 1-meter high fill in front of the wall. The plan view of the structure is shown in Figure 2-5. The approach ramp is 12.5 meters wide with one traffic lane in each direction.

The facing panels were 150 cm x 150 cm in frontal area, and the reinforcing elements were ribbed, galvanized steel strips with a cross section of 40 mm x 5 mm. Typically, four strips were used per panel at a horizontal spacing of 75 cm. The backfill soil was of good quality, consisting of sand and gravel that was compacted in lifts during wall construction. A cross-section of the maximum section of the double-walled abutment is given in Figure 2-6. At this maximum wall section, the wall is 10 m high and steel strips with a cross-sectional area of 40 mm x 5 mm and length of 7 m were used. Design drawings indicate that the reinforcements were placed with a horizontal-to-vertical grade of 5%. Five strips were used per panel for the two lower panels and four strips were used per panel for the upper panels at this maximum wall section being modeled. The embankment is 12.5 m wide, resulting in a 1.5-m reinforcement overlap at the wall center for the cross section considered. As shown in Figure 2-6, the reinforcements were not connected at the overlap zone. As can be seen, the foundation soil originally had a moderate slope that which was leveled for construction. The base of the left wall was 75 cm higher than for the right wall.

The reinforcement length was 7 meters along the first 30 meters of the wall where the wall height ranged between 8-10 meters. The reinforcement length was reduced to 6 meters along the next 25 meters of the ramp where the wall height averaged about 7 meters. Shorter reinforcements of 5 meter length were used for the remaining sections of the wing wall that were all 6 meters high or less.

The walls were initially designed to resist 0.1g peak ground acceleration. It was concluded that the seismic design resulted in little to no increase in the amount of reinforcement required by static design (Sankey and Segrestin 2001). This issue is further investigated in the subsequent sections.

### 2.1. Observed Field Performance Summary

Field reconnaissance for the Arifiye Bridge site was performed a week following the August 1999 earthquake (Mitchell et al. 2000). The closest accelerometer was located about 10 km away in Adapazari where the maximum peak ground acceleration was measured at 0.4g. The soil conditions at the bridge site however, are different than those found at Adapazari, and less localized amplification would be expected. It is thought that the accelerations at the Arifiye Bridge were probably closer to those near Izmit, in the range of 0.2g-0.3g. This is estimated based on the near field recordings of earthquake motion at stations near the fault rupture. (Rathje et al. 2000; Safak and Erdik 2000)

In addition to significant shaking, ground displacements within a few meters of the RE walls were large, as the surficial fault rupture passed between the northern abutment and the center pier (see Figure 2-2). Maximum horizontal and vertical ground displacements near the northern abutment were estimated at 350 cm and 45 cm, respectively.

Four spans of the bridge collapsed in a "saw-tooth" manner (see Figure 2-7) due to relative displacements of the piers and abutments, along with inadequate beam seat widths. Fault rupture passed under the overpass structure, between the northern abutment and the center pier. Relative offset of 3.5 meters was excessive to be sustained by the available beam set width.

In addition to fault-related ground deformations, foundation settlement up to 25 cm was observed in the section of the wall overlying the culvert. The abutment and the MSE structure are shown in Figure 2-8, where ground cracks near the ramp and signs of distress on one side of the wing wall are visible. The culvert appears to have settled during the earthquake, probably due to the presence of soft and/or liquefiable creek bed sediments that were noted above. The settlements were concentrated at sections of the ramp between the culvert and the reinforced concrete abutment where the ramp reaches its maximum height (about 9 meters grade separation between the top of ramp and the ground, and about 10 meters maximum wall height). Settlement-related ground cracks near the culvert are shown in Figure 2-9. Misaligned facing elements in the section where the settlements were maximum are shown in Figure 2-10. Separation of the facing panels caused the backfill material to spill out. The spilled backfill and misaligned facing panels are shown in Figure 2-11.

A schematic of damage to the wing walls are shown in side and plan views in
Figure 2-12 and Figure 2-13 respectively. Numerous ground cracks were observed near the wing walls. These cracks were aligned perpendicular to the MSE structure and extended about 4 meters. Location and orientation of these ground cracks suggests that these were associated with the uneven settlement along the base of the MSE wall. It seems that the heavy structure and the relatively strong fill underneath the wall (2-meter thick dry crust) punched through the foundation soil. The resulting differential wall settlement caused the facing panels to become separated and misaligned, which allowed spillage of some backfill material. Damage at the top of the embankment is shown in Figure 2-14.

The settlements formed a cone of depression with the maximum settlement near the wall face causing ground cracks perpendicular to the alignment of the approach embankment. No bulging deformations were observed at the ground surface near where the settlements occurred. This suggests that the settlements resulted from compressions in the foundation soils beneath the relatively strong dry crust. Any deformation that took place was confined by the dry crust which possibly prevented any evidence of bulging to be observed at the ground surface.

The height of the structure, and therefore the load on the foundation soil, reaches its maximum near the area of observed settlement. Larger load levels may have also been one of the factors to the concentration of settlements in that particular area. Several three- to four-story residential buildings were present in the area, at very close proximity to the approach embankment. These are reinforced concrete structures with hollow brick infill walls and are supported on shallow foundations. Minor structural damage was observed at some of these buildings. However, our visual investigations did not reveal any foundation related problems (i.e. settlement, punching failure) at the buildings we investigated. No evidence of ground failure was observed around these buildings. And unfortunately, no detailed information was available on the foundation system of these structures. Therefore, it was not possible to estimate the contact pressure exerted by these structures and to compare those values the level of surcharge at those sections of ground failure (10 meters of earth fill ~200 kPa).

Another possible mechanism for the localized settlements might be related to the difference in subsoil conditions along the wall. The presence of the creek channel and the box culvert suggest differences in soil layering (i.e. localized liquefiable creek deposits) at these sections. Accordingly, our subsoil investigations were geared primarily towards assessing possible differences in soil conditions along the wall. However, as discussed in the following sections, there were only minor differences observed among soil conditions at the site.

It is possible too that the weak foundation soils suffered strength loss due to intense shaking and settled under the weight of the overlying structure; although, it is not possible to pinpoint to any specific layer that suffered any strength loss. No sand boils were observed at and around the site. However, as discussed above, the presence of a 2-meter thick dry crust may have prevented any surficial manifestation of liquefaction at depth.

The reinforced concrete bridge abutment on pile foundations appeared to have not been affected by the settlement. No ground cracks were observed near the reinforced concrete abutment. This is probably because the structural loads were transmitted to deeper, stronger layers, bypassing the weaker shallow soils. Piles supporting the abutment may have also helped reduce the earthquake induced stresses and deformations at these upper layers, improving their dynamic response.

In addition to slip joints being used at regular intervals along the wall, slip joints were also present along each side of the concrete culvert. Apparently, these joints added to the flexibility of the wall and its tolerance to uneven deformations. The slip joints appear to have allowed the wall to sustain deformations and settlements without being overstressed; the facing panels were intact and no signs of distress on the panels were noted.

One important observation was the relative lack of damage to any of the facing panels despite the large levels of shaking and resulting deformations. No signs of damage such as broken panel parts or cracks were present, although out-of-plane deformations of the wall face were observed. The maximum out-of-plane panel displacement was about 10 cm and was located about one-third from the base of the wall (i.e. about 3 meters from the base of the wall at the 10 meter high section).

The most notable overall observation was the relative lack of significant damage to the RE walls despite being subjected to strong ground shaking and large displacements. In stark contrast to this behavior, a conventionally-constructed approach embankment located about 250 m from the RE wall suffered heavy damages during the earthquake, experiencing settlements of more than 1 meter. The good performance of the RE walls is thought to be particularly meaningful in demonstrating the seismic stability of conventionally-constructed walls of this type.

Key observations from the reconnaissance can be summarized as follows:

1) The fault rupture passed through the northern abutment and the adjacent pier causing lateral offset more than 3 meters. The bridge decks collapsed due to relative movement of the piers and the bridge abutments at both sides. Bridge deck spans were simply supported.

2) Taller sections of the MSE structure settled, punching into the foundation soils. This resulted in the misalignment of several facing panels. Relative displacement of the facing panels caused them to separate and this resulted in the spillage of some backfill material.

3) The MSE structure performed well despite the high levels of shaking and foundation problems. The structure was designed for a seismic coefficient $k_h = 0.1$.

The wall was subjected to acceleration levels at least twice the design value and still maintained its structural integrity.

4) The structure underwent permanent deformations as a result of shaking. Permanent deformations may be more important in terms of serviceability of such structures. This case demonstrates that significant permanent deformations can develop before the collapse of the earth structure. However, there are no methods in current design guidelines to estimate the permanent deformations of reinforced soil structures. Permanent deformations should be considered during the seismic design of reinforced soil structures.

5) Reinforced concrete bridge abutment on piles did not suffer damages despite ground failure in the vicinity. The abutment did not settle in contrast to the MSE wall it supported.

6) It was obvious that the slip joints allowed the wall to sustain these significant foundation deformations without being overstressed.

**2.2. Subsoil Conditions**

The Arifiye Reinforced Earth Wall site is situated within a deposit of Quaternary alluvial sediments. We performed investigations at the site to determine the subsoil conditions. Cone Penetration Testing with shear wave velocity measurements (SCPT) was performed at two locations. These data, along with soil borings obtained from State Highway Directorate, indicate the presence of alternating layers of medium clay and medium sand, with the water table at a depth of about 2 m. A creek runs parallel to the highway and passes beneath the site under what was the northern approach embankment. The culvert was built beneath the abutment to encapsulate the creek flow.

Results of a Standard Penetration Test performed near the southern abutment by the State Highway Directorate are shown in Figure 2-15. It should be noted that the soil descriptions are based on visual inspection of the drilling crew, rather than laboratory testing. It was not possible to verify the layer descriptions of the crew. A donut hammer was used in the drilling, and the delivered energy ratio is estimated to have been about 40-50% (Skempton

1986). This may have caused larger blow counts than we would expect with the standardized energy ratio of 60%.

Cone penetration testing with shear wave velocity measurements (SCPT) was performed at two locations near the MSE walls. The approach embankment with MSE wing walls was demolished at the time of the investigations (October 2000) and construction works were in progress to replace the approach embankment with a reinforced concrete structure. Shear wave velocity measurements were performed with a downhole setup with 1-meter intervals throughout the depth of the CPT. One of the CPT's (CPT-1) was located near the culvert and extended to a depth of 22 meters. The second sounding (CPT-2) was performed near the sections of the walls that suffered less damage and extended to a depth of 26 meters. The location of the CPT soundings is shown in Figure 2-5.

As discussed above, most of the ground damage and settlement was concentrated at the sections of the wall located between the culvert and the reinforced concrete abutment. Again, the location of the CPTs was selected to investigate the possibility of differences in soil conditions along the wall. CPT-1 is located near the culvert at the zone of maximum ground damage, whereas CPT-2 is located in an area of no apparent ground damage. Measurements of tip resistance ($q_c$) and sleeve friction ($f_s$) were interpreted using current procedures of soil identification methods (Lunne et al. 1997).

The sounding from CPT-1 and shear wave velocity measurements at that location are shown in Figure 2-16. It can be seen that the upper 8 m of the profile consists of 2 m of fill underlain by a 2 m-thick medium clay layer that is underlain by a 1 m-thick loose sand stratum. A mixed layer is found between the depths of 5 m and 8 m. A medium-to-stiff clay stratum extends from the depth of 8 m down to 22 m where the CPT was terminated.

Measurements from CPT-2 are shown in Figure 2-17. Similarly, the upper 8 m of the profile consists of 2 m thick fill underlain by a 2 m-thick medium clay layer that is underlain by a 1 m-thick dense sand stratum. A mixed layer is found between the depths of 5 m and 8 m. A medium-to-stiff clay stratum extends from the depth of 8 m down to 26 m where the CPT was terminated.

Shear wave velocity measurements increase gradually with depth and average about 150 m/s throughout the 25 m profile. Alternating layers of sand and medium clay at the top 10 meters of the profile have an average shear wave velocity of 130 m/s. Shear wave velocity increases to 150-200 m/s at depths where the clay gets stiffer.

Both soundings reveal similar results in terms of soil layering. The only difference between the two soundings is the relative penetration resistances of the 1 meter thick sand layer (at about 5 meters depth). The presence of the loose sand layer near the area of ground damage as opposed to the dense sand layer is important and may have contributed to the ground failure and observed behavior. But it is difficult to attribute the overall contrast in behavior to this thin (about 1-meter thick) soil layer.

These soundings were used to estimate certain soil characteristics such as fines content and normalized clean sand equivalent penetration resistance. For this purpose soil behavior index ($I_c$) is estimated from tip resistance measurements ($q_c$) and friction ratio. It is possible to estimate fines content using $I_c$ and available interpretation procedures. In any case these interpretations are still approximate at best and should be used with caution. Below is a brief description of the procedure (Lunne et al. 1997).

Soil behavior type index ($I_c$) is calculated using the relationship

$$I_c = \left[ \left( \log Q - 3.47 \right)^2 + \left( \log F + 1.22 \right)^2 \right]^{0.5}$$

where Q is the normalized cone penetration resistance and F is the normalized friction ratio as defined below;

$$Q = \frac{q_c - \sigma_{vo}}{P_a} \left( \frac{P_a}{\sigma'_{vo}} \right)^n \text{ and } F = \frac{f_s}{q_c - \sigma_{vo}} \cdot 100\,\%$$

These parameters used in the equations are;

$q_c$ : cone penetration resistance

$f_s$ : sleeve friction

$\sigma_{vo}$, $\sigma'_{vo}$ : total and effective vertical overburden stress respectively

$P_a$ : atmospheric pressure in the same units as $q_c$, $f_s$, $\sigma_{vo}$ and $\sigma'_{vo}$

n : stress exponent factor

The value of stress exponent, n, depends upon the soil type and 1.0 is an appropriate value for clayey soils and 0.5 for clean sands. The selection of the stress exponent requires an iterative process because the procedure to determine the soil behavior type index ($I_c$) requires to assume a stress exponent which inherently is a function of soil type and therefore $I_c$. Robertson and Wride (1997) recommend using a stress exponent 1.0 to calculate $I_c$ as the initial step. If the calculated $I_c > 2.6$ then it means the soil is a clayey and it is in agreement with the initially assumed value of stress exponent. However, if the calculated $I_c < 2.6$, $I_c$ should be recalculated using a stress exponent n = 0.5, a value that corresponds to clean granular soils. If the recalculated $I_c < 2.6$ then the soil is most likely granular. However, if the recalculated $I_c$ is > 2.6 then the soil is a sand-silt-clay mixture. In this case $I_c$ should be once again be recalculated using a stress exponent 0.7.

Once a soil type consistent value of stress exponent n is determined, measured cone penetration resistance should be normalized for the effect of overburden pressure. Normalized cone penetration resistance is a dimensionless quantity and is defined as;

$$q_{c1N} = C_Q \cdot \frac{q_c}{P_a}$$

where qc is the cone tip resistance; $C_q = (P_a/\sigma_{vo})^n$ correction for effective overburden stress; n is the stress exponent and $P_a$ is the reference pressure level as discussed above.

Fines content is can be estimated using soil behavior type index as;

Fines Content

= 0 % for $I_c < 1.26$

$= 1.75\ I_c 3.25 - 3.7 \times 100\ (\%)$ for $1.26 \leq I_c \leq 3.5$

$= 100\ \%$ for $I_c > 3.5$

Results of soil behavior type index and estimated fines content are shown in Figure 2-18 and Figure 2-19 for CPT-1 and CPT-2 respectively. Both profiles exhibit similar characteristics with a 2 meter thick fill underlain by alternating clay and sand layers. Clayey levels are identified by high $I_c$ values (>2.6) and sandy levels are identified by lower values. The sand layer at 5 meters from ground surface is about 1-meter thick. This layer has $I_c$ values as low as 1.5 indicating a clean sand. Peak values of normalized clean sand equivalent tip resistance ($q_{c1,CS}$) are estimated as 140 and 240 for the thin sand layer at soundings CPT-1 and CPT-2, respectively. This layer is overlain and underlain by soft-to-medium clay layers. Both of these layers above and below are mixed with thin sandy lenses indicated by low $I_c$ values throughout. Normalized clean sand equivalent tip resistance for these layers are fairly uniform and estimated to be about 80.

No information was available on the plasticity characteristics of the clayey levels. With the plasticity information we would be able to assess the liquefaction susceptibility of the silt/clay layers in the upper portions of the profile. The presence of ground cracks near the culvert and settlement of the MSE embankment suggest that the foundation soils lost some strength during the earthquake. It is not possible to determine which particular layer or layers suffered what extent of earthquake induced strength loss. Normalized clean sand equivalent penetration ($q_{c1,CS}$) is used to estimate the cyclic resistance of the soils. Recently revised correlations are used for this purpose (Youd et al. 2001). This analysis is performed for level ground conditions. The effect of a static shear stress on the foundation soil from the presence of the 10-meter high MSE structure is not included in this analysis.

Estimated cyclic resistance (CRR) profiles are shown in Figure 2-20 and Figure 2-21 for soundings CPT-1 and CPT-2 respectively. Cyclic resistance ratio for the soils is plotted along with cyclic stress ratio (CSR) for two different levels of peak ground acceleration 0.2g and 0.3g. CSR is estimated using the simplified procedure of liquefaction analysis. Plotted cyclic resistance curves are smoothed using a moving averaging window of 20 cm. Sand layer at CPT-1 sounding has a peak cyclic resistance ratio (CRR) about 0.32, compared to CSRs of

0.19 and 0.28 from peak ground accelerations of 0.2g and 0.3g, respectively. Whereas, on the other hand the denser sandy levels at CPT-2 location have very high peak CRRs (i.e. > 0.5-0.6 off the scale in the CRR vs. $q_{c1,CS}$ boundary curve). Looser sandy strata may have lost strength under strong ground shaking (PGA ~0.3g). Clayey strata have cyclic resistance consistently lower than both levels of cyclic demand. The cyclic resistance ratio of the clayey levels is estimated to be around 0.10 to 0.13.

Above comments on the estimated CRR of the clayey soils apply only if those soils were susceptible to earthquake-induced strength loss. We do not have any information on the plasticity characteristics of these soils. It may be possible that these levels are susceptible to liquefaction they are non-plastic or have low plasticity. However, it was not possible to confirm this suspicion. In any case, the CRR estimates for these soils are shown in comparison to CSR estimates. These analyses show that soft clayey and loose-to-medium dense sandy foundation soils are susceptible to liquefaction as predicted by the current methods. However, the lack of information on the plasticity of the silty/clayey levels prevents any conclusive statements on the liquefaction potential of these levels. Further sampling and subsequent laboratory testing (index tests and cyclic loading tests) of these soils can yield a definitive explanation of the foundation performance at the site. In any case, the thin sandy layer at 5 meters depth is clearly susceptible to liquefaction at moderate levels of shaking.

The penetration resistance of the thin sand layer is different at the two CPT locations. However, given the thickness of the sand layer (about 1 meter), it is not possible to attribute the stark contrast in behavior to this difference in soil conditions. It is most likely that the soft/loose mixed layers above and below this sand layer lost strength and resulted in the observed ground damage under the load of the overlying structure. It is not possible to make a conclusive statement due to lack of data on the plasticity characteristics of these levels. As discussed above the level of load induced by the structure at the sections of ground failure may correspond to a threshold level to trigger excessive settlements when combined with strength loss in the foundation soils.

## 3. DESIGN CONSIDERATIONS OF REINFORCED SOIL STRUCTURES

Reinforced soil structures are gravity retaining structures. Their static and dynamic design involves the estimation of external forces acting on the structure to evaluate external and internal stability. Dynamic stability analysis also involves estimation of inertial forces that arises from the acceleration of the reinforced soil block and the retained soil. The main challenge in design is to select the appropriate level of lateral forces arising from dynamics.

External design involves considerations such as sliding or overturning of the structure as a monolithic block, bearing capacity of the foundation soil against increased normal pressure near the toe and a potential deep seated failure surface not contained within the reinforced soil mass. For internal design one should estimate the anticipated reinforcement forces and the geometry of the potential sliding surface at limit state. Width of the reinforced zone is selected to provide adequate external stability.

External design ensures the reinforced block provides enough gravity resistance against the external forces. Internal design ensures that the reinforced block is strong enough and maintains its structural integrity against external forces (i.e. horizontal pressure from the retained fill, traffic surcharge) and self-weight.

In static analysis, the force exerted on the reinforced block by the retained soil is estimated using fundamental soil mechanics principles of lateral earth pressure. The soil retained behind the MSE wall is assumed to be in limit equilibrium. The force exerted on the reinforced soil zone by the retained soil is calculated simply by well known earth pressure formulas (i.e. Rankine or Coulomb earth pressure theories). This force is assumed to be acting at one-third the wall height (H/3), corresponding to a triangular earth pressure distribution.

External failure modes of mechanically stabilized earth walls are shown in Figure 2-22. The MSE wall is treated as a monolithic gravity retaining structure and these failure modes are checked comparing the applied forces (lateral earth thrust, lateral inertia force in case of an earthquake) and resisting forces (weight of the reinforced soil zone, shear resistance along the base).

In the internal design, a slip surface contained within the reinforced block is assumed. Horizontal earth pressures within the soil mass are calculated using the vertical overburden stress and an assumed idealized earth pressure coefficient. Each level of reinforcement is assumed to carry the load arising from the stresses acting on its tributary area.

Figure 2-23 shows the potential sliding surfaces for MSE structures with inextensible and extensible reinforcements. Internal design is based on the assumption that the maximum reinforcement forces coincide with the sliding surface. Maximum reinforcement forces are checked for internal stability against reinforcement pullout and rupture. Pullout resistance is calculated from the frictional resistance of the reinforcement in the passive region.

Figure 2-24 shows the earth pressure coefficient values recommended by Federal Highway Administration for use in the internal design of MSE walls (Elias and Christopher 1999). Earth pressure coefficient within the reinforced soil zone is estimated from the active earth pressure coefficient ($K_a$) and the type of reinforcement. Larger values of earth pressure coefficient are used at the upper elevations in structures built with inextensible reinforcements. This accounts for the compaction induced earth pressures which are locked in at the upper levels of the reinforced soil structure. Structures with inextensible reinforcements (i.e. steel strips) will be restrained to move laterally during construction and compaction induced stresses will be locked within the soil mass. This situation is analogous to the overconsolidated state of soils due to loading-unloading cycles. As more lifts are added the "overconsolidated" stress state diminishes as the locked in pressures are overcome by the added pressure. Compaction induced earth pressures by the typical equipment used in lift compaction is about equal to horizontal pressure caused by about 6 meters (20 ft) of fill. Therefore, larger-than-active earth pressure coefficients are used at the top 6 meters of mechanically stabilized earth walls built with inextensible reinforcements. Active earth pressure coefficient is used in structures with extensible reinforcements (i.e. geotextile sheets) because these structures are relatively free to move laterally during placement and lift compaction.

Figure 2-25 shows the recommended friction coefficient values to estimate the frictional resistance of ribbed steel strips. Arifiye MSE walls were built using ribbed steel strips.

Static and earthquake design of these structures have general common principles. In the external seismic stability analysis, magnitude of the dynamic force increment due to shaking is calculated using the Mononobe-Okabe approach (Mononobe 1924, 1929; Mononobe and Matsuo 1929; Okabe 1924). This is an extension to the conventional Coulomb sliding wedge theory incorporating the effects of lateral inertia forces on the retained soil mass. As in the static case, the soil behind is assumed to be in limit equilibrium (at active state of failure) exerting horizontal thrust onto the reinforced soil block. This external force is simply applied to the reinforced block as if the soil block is a monolithic unit and conditions regarding external stability are calculated. In internal design, the lateral inertial force exerted on the potentially sliding block (active zone) is estimated from the seismic coefficient ($k_h$). Pullout and rupture are checked under static forces and this additional dynamic force.

There are several design methods available in engineering practice for static and seismic stability analyses of reinforced earth structures. As mentioned above, both static and dynamic cases design methods are based on limit equilibrium. Several methods with minor differences are currently used in practice to estimate dynamic component of lateral earth pressures. These procedures in general are called pseudo-static limit equilibrium methods.

Recently, attempts have been made to estimate earthquake-induced permanent displacements of mechanically stabilized earth structures (i.e. Cai and Bathurst 1996). This requires the estimation of a yield acceleration and double integration of the time history of shaking above this value. This approach is a modified version of the Newmark method (Newmark 1965, Whitman 1991) as originally proposed for estimating permanent displacement of earth structures using the analogy a rigid block on a frictional sliding surface analogy.

### 3.1. Pseudo-static analysis

Current design guidelines require the pseudo-static limit equilibrium method for stability analysis of geosynthetic and metal-strip reinforced soil walls at sites with peak ground accelerations less than 0.29g (AASHTO 1996; Elias and Christopher 1999; Mitchell and Villet 1987). Dynamic deformation analysis is recommended for higher acceleration levels.

Pseudo-static analysis is an extended limit equilibrium method and uses an estimated dynamic earth pressure to assess the stability of retaining walls and slopes. Magnitude of the

dynamic force (from the retained backfill) and the lateral inertia force on the retaining system (reinforced soil zone) are evaluated using a seismic coefficient. Various methods and empirical recommendations are available to estimate the magnitude of dynamic earth pressures (Whitman 1990). Once the magnitude of static and dynamic forces is estimated, various failure mechanisms; both external and internal, can be checked for stability. These mechanisms include sliding along the base, overturning, bearing capacity as the external failure modes and pullout of the reinforcements, tensile overstress of the reinforcements as internal sliding.

One of the earliest and most common methods used in engineering practice today is the Mononobe-Okabe approach which was originally proposed in 1920's for estimating dynamic earth pressures on gravity retaining walls (Mononobe 1924, 1929; Mononobe and Matsuo 1929; Okabe 1924). In this method, the Coulomb wedge analysis is extended to include horizontal and vertical inertial forces due to ground shaking. The geometry and force diagram associated with this method is shown in Figure 2-26. The backfill retained by the wall is assumed to be in an active mode of failure under self weight and inertial forces due to ground acceleration. Both the retaining structure and the retained backfill act as rigid bodies with the maximum shear stress along the potential sliding surface.

The main assumptions of the Mononobe-Okabe method are;

1. The backfill is above the water table.
2. The backfill has undergone sufficient displacement and a full shear resistance has developed along a sliding plane as it is assumed in a Coulomb sliding wedge analysis in a static case.
3. The acceleration is assumed to be constant throughout the sliding mass behind the wall. This is equivalent to saying the mass is moving as a rigid block.

Whitman (1991) emphasizes that dynamic earth pressures on earth retaining structures is a complex problem of soil-structure interaction and suggests that peak dynamic stresses should be of little concern in design. The Mononobe-Okabe approach fails to represent the actual

dynamic behavior, but it is a scheme to relates dynamic earth pressures to a possible state of failure.

Magnitude of the dynamic earth force is correlated to the static earth pressure by a coefficient $k_h$ which is based on the maximum ground acceleration. In the Mononobe-Okabe method the total active earth force is calculated as;

$$P_{AE} = \frac{1}{2}\gamma H^2 \left[(1 \pm k_v) K_{AE}\right]$$

where, $\gamma$ is unit weight of the retained soil, and H height of the wall and $K_{AE}$ is the total earth pressure coefficient. The vertical acceleration coefficient $k_v$ will have a plus (+) sign when acting downward and will have a minus (-) sign when acting upward. In most cases the vertical ground acceleration is taken as acting upward reducing the total active earth pressure; in some cases it is ignored completely. Following formulations will use the convention where vertical ground acceleration is acting upward, utilizing the form of the above formula with the negative (-) sign. The total earth pressure coefficient for a cohesionless dry backfill can be calculated using the formula;

$$K_{AE} = \frac{\cos^2(\phi - \psi - \theta) / \cos\psi \cos^2\theta \cos(\psi + \theta + \delta)}{\left[1 + \sqrt{\frac{\sin(\phi + \delta)\sin(\phi - \psi - \beta)}{\cos(\beta - \theta)\cos(\psi + \theta + \delta)}}\right]^2}$$

where,

$\phi$ = friction angle of the retained soil

$\delta$ = mobilized interface friction angle between the back of the wall facing and the backfill soil (or mobilized interface friction angle between back of the reinforced soil zone and the retained soil in case the reinforced earth wall system is treated as a monolithic structure)

$\theta$ = inclination angle of the inside face of the wall with the vertical (or the batter angle of the back of MSE wall)

$\beta$ = back-slope angle

$\psi$ = seismic inertia angle given by

$$\psi = \tan^{-1}\left(\frac{k_h}{1-k_v}\right)$$

The horizontal component of the total active thrust is;

$$P_{AE-HOR} = \frac{1}{2}\gamma H^2\left[(1-k_v)K_{AE}\right]\cos(\delta+\theta)$$

Parameters $k_h$ and $k_v$ are horizontal and vertical seismic coefficients, respectively, and are expressed as fractions of the gravitational acceleration g. As can be seen from the lengthy formulation above, ground acceleration poses a dynamic force that can be calculated using mechanical properties of the soil and the wall geometry along with characteristic values related to ground acceleration. As originally proposed the parameters $k_h$ and $k_v$ are horizontal and vertical ground accelerations respectively (Mononobe 1924, 1929; Okabe 1924). Several recommendations are available in the literature for the selection of the coefficient.

- Whitman (1990) reports that values of $k_h$ from 0.05 to 0.15 are typical for the design of gravity wall structures corresponding to 1/3 to 1/2 of peak design acceleration between 0.10g-0.45g.
- Bonaparte et al. (1986) recommend $k_h = 0.85$ a/g where a is the peak ground acceleration at the site
- Segrestin and Bastick (1988) relate $k_h = (1.45 - a/g)(a/g)$

It is convenient to divide the total earth thrust into static and dynamic components;

$$P_{AE} = P_A + \Delta P_{AE}$$

where $P_A$ is the static active earth pressure and $\Delta P_{AE}$ is the dynamic pressure increment. Static component can easily be calculated with;

$$P_A = \frac{1}{2}\gamma H^2 K_A$$

where active earth pressure coefficient $K_A$ using the Coulomb formula is expressed as;

$$K_A = \frac{\cos^2(\phi-\theta)/\cos^2\theta\cos(\theta+\delta)}{\left[1+\sqrt{\frac{\sin(\phi+\delta)\sin(\phi-\beta)}{\cos(\beta-\theta)\cos(\theta+\delta)}}\right]^2}$$

Seed and Whitman (1970) suggest a simple approximation to the total earth pressure coefficient for simple geometries. This provides a reasonable value of total earth pressure coefficient for vertical walls and horizontal backfills. It is simply related to the static active earth pressure coefficient and horizontal seismic coefficient;

$$K_{AE} \approx K_A + \frac{3}{4}k_h$$

The difference between the total earth pressure coefficient and static active earth pressure coefficient is (increment in earth pressure coefficient);

$$\Delta P_{AE} = P_{AE} - P_A$$

Using the above relationships, the dynamic component of earth pressure becomes;

$$\Delta P_{AE} = \frac{1}{2}\gamma H^2\left(\Delta K_{AE} - k_v K_{AE}\right)$$

The resultant lateral thrust and the dynamic increment act with an angle to the horizontal. The horizontal component of the dynamic force increment is;

$$\Delta P_{AE-HOR} = \frac{1}{2}\gamma H^2 \left(\Delta K_{AE} - k_v K_{AE}\right)\cos(\delta + \theta)$$

Like the original Coulomb sliding wedge analysis, the Mononobe-Okabe approach provides the magnitude of the total force exerted on the retaining structure, but not the location where this force acts nor the distribution of the lateral earth pressures behind the wall. In its original formulation, the force resulting from dynamic earth pressures were assumed to act at one-third the wall height from the bottom as the static component of lateral thrust (Mononobe 1929). Several researchers have studied the magnitude and distribution of lateral earth pressures either analytically, making additional assumptions or by experiments on models (Bakeer et al. 1990; Prakash and Basavanna 1969; Prakash and Nandakumaran 1973). It has been generally observed that the distribution of dynamic earth pressure does not increase linearly with depth as in the case of geostatic pressures. These studies indicate that the dynamic portion of the lateral thrust acts about 0.33H – 0.55H for a range of acceleration levels and wall movement patterns. Seed and Whitman (1970) recommend that the dynamic component of the pressure resultant should act at 0.67H above the base with the combined dynamic and static thrust located at or near mid-height of the wall.

There are some concerns about the validity of the assumptions inherent in the Mononobe-Okabe procedure. These are related to the form the inertial forces related to the horizontal ground acceleration act along the wall. Horizontal peak ground acceleration acts instantaneously for a very short period of time. One disadvantage of this method is that it does not consider the effects of duration, frequency content of the strong ground motion and amplification of the base motion through the structure (i.e. rigid soil block and therefore constant acceleration throughout).

The method does not consider the duration of the ground motion and its effect on the stability. Although this is a stability problem at certain instances the magnitude of the energy

input into the system may be important which make it necessary to consider the differences between short and long duration motion.

Peak acceleration at the wall base and the wall crest may not be the same. Shear waves are transformed, as they propagate up from the ground through the wall. The peak acceleration will not be acting on the entire wall height at the same time. The wall has a certain finite height which will result in a phase difference in the waveform acting along the wall even if it does not go through any transformations due to the structural response of the wall.

When this method is applied to reinforced soil systems the same formulas can be used to estimate the dynamic earth pressures, but one should be very careful picturing the failure mechanism and the sliding wedge. In analogy to the method as originally proposed for gravity walls, the dynamic earth pressures of the retained backfill act upon the monolithic mass of reinforced soil system. It should be kept in mind that the dynamic earth pressures are estimated from the failure mode where the retained soil that is in a dynamic active mode of failure. Eventually when the calculated resultant force is applied externally to the reinforced soil system and stability is checked it may turn out to be a wedge (planar, bilinear, log spiral, circular) may be in a state of failure. On the other hand from field observations we know that rather than collapsing with reinforcement failure such walls undergo displacements during an earthquake that might be critical and should be considered.

In addition to the obvious practical limitation of these procedures, an added disadvantage of the current methods is that they do not consider the effects of duration, frequency content, flexibility, possible amplification/de-amplification of the base motion through the structure, etc. Also, displacements cannot be predicted with these methods, although it has been shown in field observations and model tests that seismically-induced displacements are often the controlling criteria in terms of wall serviceability following an earthquake (Nova-Roessig and Sitar 1998; Sitar et al. 1997).

Mononobe-Okabe approach is a consistent and well established method. However, the validity of the estimated dynamic earth pressure is strongly dependent on the selected seismic coefficient. On the other hand current design guidelines acknowledge the need for special analysis for higher levels of ground shaking (Elias and Christopher 1999).

### 3.2. Displacement-based design - Newmark's Method to calculate earthquake-induced displacements

Reinforced soil systems are flexible structures that can undergo significant internal straining before collapse. The fact that such structures maintain their integrity at high levels of dynamic straining makes it necessary to develop additional approaches to the analyses of these structures. Permanent displacements can be a more critical concern under seismic conditions.

Currently there are simplified methods for estimating permanent displacement of earth structures. These methods utilize several of the parameters like, peak ground acceleration, peak ground velocity, fundamental period of the embankment and the yield acceleration (a measure of the shaking level where dynamic factor of safety drops to unity). These methods were also modified to estimate permanent displacement of gravity retaining walls. It is therefore useful to estimate the permanent displacements of mechanically stabilized earth structures using this method. This will give an estimate of the translational movement of the MSE wall as a rigid block. Additional work needs to be done to estimate the permanent deformations associated with the internal shearing of such structures. Internal deformations will develop at high acceleration due slip of reinforcements out of the resistant zone and slip of the entire soil block along the reinforcement.

The approach to estimate permanent displacements was first developed for earth embankments and slopes and later adapted to retaining structures. This method roots back to R.V. Whitman (Marcuson 1991) and was first introduced to the earthquake engineering community by N.M. Newmark (Newmark 1965). The concept was later modified to be incorporated in the permanent deformation analysis of gravity retaining walls and mechanically stabilized earth embankments (Cai and Bathurst 1996; Ling 2001; Richards and Elms 1979).

It has been suggested that permanent deformation, rather than stability against maximum pressures should be the design criterion for gravity retaining structures (Richards and Elms 1979). Sliding block analogy is commonly used to estimate the permanent deformation of retaining walls, embankments and slopes. The method was proposed to the engineering community by Newmark (1965). In his original landmark paper Newmark proposes the use

of an analogy to calculate permanent deformation of dams and embankments. The method uses a pseudo-static stability analysis to estimate the seismic acceleration to bring the statically stable embankment/slope to the verge of failure. Newmark presents and discusses the rotational sliding mechanism of a slope or planar sliding of a wedge. As pointed out by Seed (1966), validity of displacements computed by the sliding block method depends upon estimating the yield acceleration as accurately as possible.

Basically the embankment/slope is simplified to a mass resting on a frictional sloping surface. Permanent deformations occur during shaking as the inertial forces exceed the frictional resistance. Permanent deformation is calculated with the double integration of the acceleration time history where the acceleration is above the yield acceleration and the velocity is non-zero. The deformation behavior is not symmetrical (downward and upward along the surface). Resistance in earth structures (dams, slopes, retaining structures) is not the same for both directions of sliding. The acceleration necessary to slide a slope uphill is much greater than what is needed to slide it downhill. The same holds for a retaining structure, where for a given retaining structure it takes a larger horizontal acceleration is necessary to fail the structure towards the backfill than away from the backfill. For this purpose we normally calculate the permanent displacements with unsymmetrical resistance where the yield acceleration is specified for "downhill" direction of motion. Displacements accumulate only in one direction and this corresponds to specifying the yield acceleration on one side of the acceleration history. The steps involved with this method are;

- estimate the yield acceleration for your system using a pseudo-static method of analysis
- select an acceleration time history and place the yield acceleration place the yield acceleration as a bracket on one side of the time history
- set the structure acceleration to yield acceleration where the ground acceleration exceeds the yield acceleration and maintain this value until the relative velocity between the ground and the structure is zero

Deformations accumulate over time as the yield acceleration is exceeded. Yield acceleration (sometimes also referred to as critical acceleration) is defined as the horizontal ground

acceleration to overcome the frictional resistance along the sliding boundary. This corresponds to a dynamic factor of safety factor of unity as calculated with a pseudo-static analysis. For a given time history of ground acceleration and estimated yield acceleration, the accumulated displacement is calculated by integrating those portions of the acceleration history above the yield acceleration.

Newmark developed a series of equations relating permanent displacement to peak ground velocity, peak ground acceleration and yield acceleration. The equation given below is the theoretical solution for the permanent displacement of a mass on a frictional surface where a finite duration acceleration pulse of magnitude $k_m$ is applied (Newmark 1965).

$$d = 0.5 \frac{v_m^{\ 2}}{k_y g} \left(1 - \frac{k_y}{k_m}\right) \left(\frac{k_y}{k_m}\right)^{-1}$$

where, $v_m$ is the peak ground velocity from the applied pulse, $k_y$ is the yield acceleration as a fraction of g (the acceleration coefficient necessary to overcome the available frictional resistance).

Furthermore, Newmark used four strong ground motion recordings, scaled them (modifying both the acceleration and time scales) to have a peak acceleration of 0.5g and peak velocity of 0.76 m/sec (30 in/s) and computed permanent displacements. The following equations were suggested by Newmark as upper-bound curves to his calculated displacements. The lower equation is for lower range of accelerations ($k_y/k_m>0.16$) and the upper equation is for higher range of accelerations ($k_y/k_m<0.16$).

$$d = 3 \frac{v_m^{\ 2}}{k_y g}$$

$$d = 0.5 \frac{v_m^{\ 2}}{k_y g} \left(\frac{k_y}{k_m}\right)^{-1}$$

It is convenient to define a non-dimensional displacement as;

$$d_r = d\frac{k_y g}{v_m{}^2}$$

Using this normalization the three equations above can be rewritten in the following form making it easier to compare with other equations of the same form which will be discussed in the following paragraphs. These relationships are shown in Figure 2-27 in terms of normalized displacement and acceleration ratio.

$$d = 0.5\frac{v_m{}^2}{k_m g}\left(1-\frac{k_y}{k_m}\right)\left(\frac{k_y}{k_m}\right)^{-2}$$

$$d = 3\frac{v_m{}^2}{k_m g}\left(\frac{k_y}{k_m}\right)^{-1}$$

$$d = 0.5\frac{v_m{}^2}{k_m g}\left(\frac{k_y}{k_m}\right)^{-2}$$

Franklin and Chang (1977) used the same procedure and analyzed numerous earthquake recordings and synthesized acceleration histories (169 strong motion records from 27 earthquakes and ten synthesized time histories). They investigated the effects of shaking duration, earthquake magnitude and site conditions on the permanent displacement of embankments and slopes. They developed several curves of normalized displacement and acceleration ratio for a variety of conditions (duration, magnitude, site condition).

The above methodology is developed for deformation analysis of earth embankments and slopes. However, it can simply be applied to retaining walls. Similarly the yield acceleration can be estimated for a retaining wall and the same procedure of double integration can be applied to estimate the permanent displacement of the retaining wall. Resistance of retaining structures, and therefore deformation, is also unsymmetrical as it was the case for slopes.

Retaining walls can undergo several modes of deformation patterns. They can slide along the base or can tilt by rotation (mainly around the base and sometimes around the wall top). Richards and Elms (1979) proposed a method to estimate the permanent displacement of gravity retaining walls. They used the sliding block analogy where the yield acceleration is estimated using a pseudo-static method and the dynamic safety factor against sliding drops to unity under the increased active forces. The relative displacement of the wall away from the backfill is calculated by double integration of the acceleration history as described above. This method assumes that sliding along the base is the dominant pattern of permanent deformations and it does not attempt to estimate rotational deformations. Based on their evaluations of data from Franklin and Chang (1977) they propose an upper bound envelope for permanent displacements in relation to acceleration ratio and peak ground velocity.

$$d = 0.087 \frac{v_m^{\ 2}}{k_m g} \left( \frac{k_y}{k_m} \right)^{-4}$$

This provides a reliable upper bound envelope for displacements for the range of acceleration ratio ($k_y/k_m$) larger than 0.30. This relation becomes highly conservative for larger shaking levels (smaller $k_y/k_m$ ratios). However, this is not an important limitation because excessive deformations are predicted for this acceleration range both for upper and lower bound envelopes.

Whitman and Liao (1984; 1985) used several earthquake records and calculated permanent displacements for various acceleration ratios. They proposed the formula below as a mean fit to their calculated values:

$$d = 37 \frac{v_m^{\ 2}}{k_m g} \exp\left( -9.4 \frac{k_y}{k_m} \right)$$

Cai and Bathurst (1996) reviewed several of the methods discussed above and recommended several relationships for the estimation of permanent displacements. They performed a

statistical analysis of data presented by Newmark (1965) and developed the following equation as a mean fit to the data (50% probability of being exceeded).

$$d = 9.2\frac{v_m{}^2}{k_m g}\exp\left(-5.87\frac{k_y}{k_m}\right)\left(\frac{k_y}{k_m}\right)^{-0.49}$$

They further analyzed the complete data set of Franklin and Chang (1977) and proposed the following formula as a mean upper-bound for displacements.

$$d = 35\frac{v_m{}^2}{k_m g}\exp\left(-6.91\frac{k_y}{k_m}\right)\left(\frac{k_y}{k_m}\right)^{-0.38}$$

The above formulas are summarized in Figure 2-28 in terms of non-dimensional displacement and acceleration ratio. They are produced by curve fitting to different sets of data computed with the double integration of acceleration data capped with a range of acceleration ratios. Scatter in data arises from the random nature of the earthquake process and our attempt to represent it with characteristic values (peak acceleration and peak velocity). It is always possible to perform the double integration with an actual acceleration history using a yield acceleration of interest rather than using the proposed correlations.

Other researchers have studied sliding block method to estimate permanent displacement of earth dams and embankments (Makdisi and Seed 1978; Sarma 1975). But these are not much useful to estimate permanent displacement of earth retaining structures because they are exclusively developed for earth dams. These methods estimate permanent displacement using the same variables used in the above formulations along with the fundamental period of the earth dam in question. Earthquake-induced displacement is calculated by integrating those portions of the acceleration history that are above the critical acceleration and those portions that are below until the relative velocity between the sliding mass and the base reduces to zero.

Some simplified empirical methods have been proposed for the original form of the Newmark displacement method as it was applied to embankment dams. These methods use characteristic values of the ground motions such as peak acceleration, peak velocity along with predominant period of the earth structure and give normalized displacements. The applicability of such methods directly to reinforced earth systems is questionable and these may not yield reliable results.

The sliding mass in the Newmark method is analogous to a rigid block resting on an inclined surface which is set into downward motion by horizontal ground acceleration. When the method is applied to reinforced soil systems the reinforced soil mass can be treated as a monolithic mass which slides along its base upon horizontal excitation. The critical acceleration is the acceleration which gives unity factor of safety in a pseudo-static analysis. As noted above if sliding along the base is considered to be the mechanism of displacements than the pseudo static analysis should be based on this mode.

It may be necessary to calculate displacements at each segmental level and evaluate the cumulative displacement at the wall crest. As an alternative the whole wall can be treated as an intact rigid unit and the displacement can be calculated for the whole system

### 3.3. Current design methods – Federal Highway Administration (AASHTO 1996; Elias and Christopher 1999; Mitchell and Villet 1987)

External design involves the estimation of static and dynamic forces exerted on the MSE structure. The structure is treated as a monolithic gravity structure which maintains its internal stability and it is checked for sliding along the base, maximum eccentricity at base, bearing stability and overall stability (deep seated global sliding). For internal design the reinforcement forces are estimated based on the idea that the horizontal pressures within a certain tributary area are carried by the corresponding reinforcements. Lateral earth pressures are calculated using the vertical geostatic stress and an earth pressure coefficient. MSE structures with comparably stiffer reinforcements (inextensible reinforcements, i.e. steel strips) utilize earth pressure coefficients larger than active earth pressure coefficient at the upper elevations (typically top 6 meters) whereas structures with extensible reinforcements (i.e. geotextiles) utilize active earth pressure coefficient throughout. This is due to the fact

that compaction-induced lateral stresses develop in the wall in MSE structures with inextensible reinforcements because lateral deformations of the wall face are inhibited during compaction.

The Federal Highway Administration design guidelines differentiate between mechanically stabilized earth walls (MSEW) and reinforced soil slopes (RSS) based on the face inclination (Christopher et al. 1989). Reinforced soil structures with face inclination steeper than 70 degrees (H:V 2.75:1) are referred to as MSEW and RSS otherwise. This is a categorization based on geometry and the design principles are the same for both types of structures. FHWA guidelines suggest that MSEW should be limited to 30 meters in height for inextensible steel reinforcements and to 15 meters for extensible geosynthetic reinforcements.

Minimum values of factors of safety for various failure modes are recommended as;

| | |
|---|---|
| External Stability | |
| Sliding | 1.5 (MSEW) |
| | 1.3 (RSS) |
| Maximum eccentricity at base | L/6 in soil, L/4 in rock |
| Bearing capacity | 2.5 |
| Deep seated stability | 1.3 |
| Seismic stability | 75% of static factors of safety |
| Internal Stability | |
| Pullout resistance | 1.5 |
| Allowable tensile strength | 0.55 yield strength (steel strips) |
| | 0.48 yield strength (geogrids) |

FHWA guidelines recognize the fact that MSEW structures and RSS are flexible structures and are resistant to dynamic forces developed during earthquakes. Several recommendations are provided for the selection of the peak ground acceleration at the site and the utilization of this value in wall/slope design. AASHTO acceleration coefficient (“A” is the peak ground

acceleration expressed as a fraction of gravitational acceleration) is utilized as the peak ground acceleration at the site (Section 3 of AASHTO Division 1-A, AASHTO 1996, pp. 397-406).

It is recognized that at sites with acceleration coefficients less than 0.05, static design will govern and no seismic design will be necessary due to the safety margin in static case (i.e. 75% of the static factors of safety are sufficient for the seismic case). Pseudo-static design is recommended for sites with peak ground accelerations between 0.05g-0.29g. Dynamic deformation analysis is required at sites with peak ground accelerations greater than 0.29g. This upper acceleration limit where the pseudo-static method is applicable will easily be exceeded in the near field of a major earthquake.

This method suggests the peak ground acceleration at the site to be selected from AASHTO guidelines (AASHTO 1996). The maximum acceleration within the wall is calculated as;

$$A_m = (1.45 - A)\, A$$

where 'A' is the maximum acceleration coefficient (as a fraction of g) from Section 3 of 'AASHTO Division 1-A Seismic Design' and '$A_m$' is the horizontal acceleration coefficient ($k_h$) to be used in wall design. It is seen that FHWA utilizes the recommendations of Segrestin and Bastick (1989) to estimate the horizontal seismic coefficient from the peak ground acceleration at the site.

For external design, the total active thrust (sum of the static and the dynamic force increment) should be estimated. Slightly modified form of the Mononobe-Okabe equation is utilized for this purpose. Components of the classical Mononobe-Okabe approach as utilized for gravity retaining structures are shown in Figure 2-26. The formulation inherently assumes that the interface between the reinforced soil zone and the retained backfill is frictionless where the $\delta$ in the original formulation is zero. In this case, the total active thrust acts parallel to the backfill slope (analogous to a Rankine earth pressure formulation). The formula for the total active thrust is given below where the symbols refer to the same variable as in the original formulation. One difference in the formula below arises from the convention in

defining the batter angle of the wall. In gravity retaining walls the batter of the wall back is away from the retained fill and the original Mononobe-Okabe formula uses this as the positive θ convention. However, reinforced soil structures will have a batter towards the retained fill. The angle should be measured with the vertical as shown in Figure 2-26 and for this reason it is a negative value for typical MSE structures.

$$K_{AE} = \frac{\cos^2(\phi - \psi + \theta) / \cos\psi \cos^2\theta \cos(\psi - \theta + \delta)}{\left[1 + \sqrt{\frac{\sin(\phi + \beta)\sin(\phi - \psi - \beta)}{\cos(\beta + \theta)\cos(\psi - \theta + \delta)}}\right]^2}$$

The dynamic force increment $\Delta P_{AE}$ is calculated using the simplified formula recommended by Seed and Whitman (1970) for horizontal backfills.

$$\Delta P_{AE} = \frac{1}{2}\gamma H^2 \left(\frac{3}{4}k_h\right)$$

The dynamic force increment is reduced 50% from the value calculated using the above formula. Reduced dynamic force increment is applied to the structure at a height 0.6H from the base parallel to the backfill slope.

Lateral inertial force exerted on the MSEW due to horizontal acceleration is calculated as;

$$P_H = \frac{1}{2}\gamma H^2 k_h$$

Lateral inertial forces on the reinforced soil zone due to shaking are calculated based on an effective width of 0.5H. On the other hand the entire MSE structure is considered in calculating the resisting forces (i.e. the weight, available shear resistance at the base). Dynamic force increment and lateral inertial force along with the static forces are applied to the MSE structure and the external stability is calculated. A reduced dynamic force increment (50% of the calculated value) is used because it is unlikely that the two dynamic forces

(dynamic force increment from the retained soil and the inertial lateral force) will peak at the same time. The force diagram for a vertical facing wall with horizontal backfill is shown in Figure 2-29. FHWA guidelines should be referred for the force diagrams of these more complicated cases (Elias and Christopher 1999, pp. 106-108). Force diagram of a mechanically stabilized earth wall with a sloping face is shown in Figure 2-30.

Internal design of mechanically stabilized earth structures involves the estimation of maximum tensile forces at the reinforcements and determination of the potential slip surface. Slip surface is assumed to be bilinear for the case of inextensible reinforcements and linear for the case of extensible reinforcements as shown in Figure 2-23. This sliding geometry is used both for static and dynamic internal stability calculations. Static lateral pressure at any level is estimated from the vertical overburden stress and the coefficient of earth pressure within the reinforced soil zone. Coefficient of active earth pressure is estimated directly from the internal friction angle ($\phi$) of the compacted granular backfill.

$$K_a = \tan^2(45 - \frac{\phi'}{2})$$

The charts recommended by the guidelines (see Figure 2-24) can be used to relate earth pressure coefficient within the reinforced soil zone to $K_a$. Magnitude of the maximum load per unit wall applied to the reinforcement due to static forces is calculated as;

$$T_{\max} = \sigma'_{ov} \cdot K \cdot S_v$$

where $\sigma'_{ov}$ is the vertical overburden stress, K the earth pressure coefficient and $S_v$ is the vertical reinforcement spacing (or the thickness of the tributary slice of the reinforcement in case of uneven vertical spacing). The guidelines should be consulted for estimation of active earth pressure coefficient and vertical overburden stress for complex geometries such as inclined backfill, traffic surcharge and inclined wall facing.

Dynamic forces are estimated using the seismic coefficient and the weight of the soil mass. Figure 2-31 provides guidelines for this procedure. As seen in the sketch the total load at

each reinforcement level (per unit width wall) is denoted by $T_{total}$ and the overall lateral thrust on the active block is denoted by $P_I$. The guidelines recommend the calculation of $P_I$ from the weight of the complete active block and estimation of the corresponding force at each reinforcement elevation from the weight On the other hand one can also calculate the dynamic force increment at each reinforcement level directly using the formula given below;

$$T_{md} = k_h \cdot W = k_h \cdot \gamma \cdot (L - L_e) \cdot S_v$$

where;

$k_h$ = horizontal acceleration coefficient, peak acceleration coefficient (as a fraction of g) of the wall shaking calculated from the horizontal seismic coefficient $k_h = A_m = (1.45A - A^2)$

$\gamma$ = unit weight of the compacted backfill

L = length of the reinforcement at the elevation

$L_e$= length of the reinforcement within the passive (resistant) zone

$S_v$ = vertical reinforcement spacing or the thickness of the tributary slice of the reinforcement)

Finally the maximum force at the reinforcement level is the sum of the static component and the dynamic component is;

$$T_{total} = T_{\max} + T_{md}$$

Stability with respect to reinforcement breakage and pullout are checked with the seismic safety factors 75% of the minimum allowable static safety factor.

## 4. STATIC AND DYNAMIC DESIGN OF ARIFIYE MSE WALLS

Limited information is available on the design procedures followed at the time of the wall construction (1988). These procedures are most likely a variant of what is in use in current practice (i.e. AASHTO 1996; Elias and Christopher 1999; 2000) because these guideline have undergone slight modifications in time. As-built conditions of the wall have been investigated using current design procedures.

Existing design procedures account for external stability and internal stability conditions. Current guidelines recommend the design back-to-back MSE walls (double walls) with the same procedures that apply to conventional MSE walls with minor modifications (Elias and Christopher 1999).

Internal design considers the reinforcement forces that are associated with the inertial/gravity forces (static and dynamic) of the reinforced zone. Internal design aims to ensure the reinforced soil structure maintains its structural integrity and acts as a monolithic structure. The same procedures used in the design of conventional mechanically stabilized earth walls apply for the internal design of double walls. Each side of the wall is designed separately assuming no interaction exists between both sides (ref and page number).

External stability analysis deals with the resistance of the structure to forces that are associated with inertial/gravity of the reinforced backfill and retained backfill. External design ensures the gravity block is stable against sliding, overturning, foundation stability and overall stability. External design of double walls differs from the design of conventional walls where the external forces due to the retained fill are not considered as a load. The adjacent wall behind is considered to support itself and is designed independently. These guidelines are followed in this section when investigating the as-built conditions of the Arifiye MSE walls in comparison to current design guidelines.

Recommended design values of earth pressure coefficient are shown in Figure 2-24. For ribbed steel strips, earth pressure coefficient varies between $1.7K_a$ ($K_a$ active earth pressure coefficient of the reinforced backfill soil) at the top of the structure to $1.2K_a$ at 6 meters from the wall top. The friction coefficient between the reinforcement and the soil is needed to

estimate the pullout resistance of the reinforcements. Values of interface friction coefficient recommended for design are shown in Figure 2-25.

Design values of reinforcement forces are estimated using the vertical stresses in the reinforced backfill and the earth pressure coefficient. The vertical stress at all levels is calculated from the geostatic stress conditions. Conventionally, the effect of the horizontal thrust from the backfill is considered in calculating the vertical stresses in the wall. Eccentricity caused by the horizontal thrust is taken into account in estimating vertical stresses within the backfill. This can either be estimated by principles of rigid body mechanics, or Meyerhof's approximation that accounts for stress redistribution due to flexible interaction (Christopher et al. 1989). However, the effect of the retained backfill is ignored, as specified by the guidelines for back-to-back walls. Therefore, vertical stresses are calculated using the unit weight of the compacted backfill soil (an assumed value of 20 $kN/m^3$ for the unit weight $\gamma$) and depth from top of the wall.

Design reinforcement forces for static design are plotted in Figure 2-32 along with upper and lower bounds of design forces (corresponding to $1.7K_a$ and $1.2K_a$ respectively). These values are for a unit wall width. Forces at individual reinforcements are calculated by multiplying these values by the width of the panel (1.5 meters in this case) and dividing by the number of reinforcements at that level (i.e. 2 strips for panels with 4 strips). Total design reinforcement forces for the left and right walls are 260.3 kN/m and 304.7 kN/m for the left and right walls respectively.

Tensile and pullout resistance at each reinforcement level are shown in Figure 2-33. Tensile strength is estimated using the tensile yield strength of steel (450 MPa ≈ 65 ksi) and the available reinforcement cross-section area per unit wall width. These tensile capacity values are the ultimate values and are not reduced to any allowable strength value. Pullout capacity is calculated using the vertical stress, friction coefficient and available surface area of reinforcement. Pullout resistance is calculated using the length of reinforcement anchored to the passive zone defined by design guidelines. The potential slip surface separates the so-called active and passive zones. The active zone is 0.3H wide at the top half of the wall. This is the pullout capacity used in design. A comparison of these values indicates that pullout

governs along the wall height except few lower layers where there is significant confining pressure. Additionally, pullout resistance of the full reinforcement length is shown for comparison.

The seismic stability analysis of the wall was investigated with a pseudo-static approach where the earthquake induced forces were evaluated using a horizontal coefficient ($k_h$). The seismic inertia force is calculated by multiplying the weight of the active zone with the seismic coefficient. The seismic inertia force is 39.6 kN/m and 46.1 kN for the left and right walls, respectively, for $k_h = 0.1$ (Weight of the active zone is 395.5. kN/m and 461.3 kN/m for the left and right walls respectively). Reinforcement forces due to seismic forces are calculated by distributing the seismic inertia force in proportion to the length of the reinforcements in the passive zone.

The Turkish Earthquake Code at the time (1988) required a seismic coefficient of 0.1 for the design of Arifiye MSE walls. Accordingly, it has been reported that the wall was designed using a horizontal coefficient ($k_h$) of 0.1 as per the earthquake code in use at the time in Turkey (Sankey and Segrestin 2001). This resulted in little increase in the amount of reinforcement required by static design. Design reinforcement forces for seismic coefficient $k_h = 0.1$ and 0.2 are plotted in Figure 2-34 along with those values of static design.

Using a seismic coefficient of 0.1 results in 14.5 to 69.0% increase in design reinforcement forces compared to static design values with the larger increase being at the upper reinforcement levels. For this case, the total reinforcement force increases to 295.9 kN/m and 350.8 kN/m for the left and right walls, respectively. This corresponds to a 13.5% and 15.1% increase in total reinforcement forces in comparison to the static design values for the left and right walls respectively. This increase in design reinforcement forces does not necessarily require an increase in the amount of reinforcement because a reduced factor of safety (generally 75% of the static factor of safety) can be used for seismic design. Therefore, the additional design force required by seismic design is offset by the reduced factor of safety resulting in little or no increase in the amount of reinforcement required.

Factors of safety for the same design conditions are shown in Figure 2-35. As seen, the static factor of safety ranges between 2.4 to 3.8 along the height of the wall. Values of the factor of

safety drop to a range of 1.2 to 3.2 for seismic coefficient of 0.1. This observation is in agreement with the earlier suggestion that using a seismic coefficient of 0.1 in accordance with the seismic design codes resulted in little or no increase in the amount of reinforcement required.

In the following sections, results of the numerical analyses are reported. Reinforcement forces calculated from numerical analyses are compared with the design values.

## 5. NUMERICAL ANALYSES

Post-earthquake observations revealed significant insight into the seismic behavior of mechanically reinforced soil structures. The level of shaking was significant and fault rupture passed very close to the MSE walls. It is also possible that the soils beneath the wall lost strength causing settlements and additional distress to the structure. All these combined constitute a significant load on the reinforced soil structure. Signs of distress on the wall were observed as out-of-plane deformations of the wall facing, misalignment and separation of the facing panels at some locations causing granular backfill to spill out. However, it is remarkable that the wall maintained its structural integrity.

Further learning opportunities are possible by extending those from the observations with numerical analysis. It is necessary to investigate issues such as how the wall behaves during shaking, the magnitude of earth pressures, reinforcement forces and deformations during and after shaking. Numerical analyses are performed for a two-dimensional cross section of the wall where the approach embankment attains it maximum height. The effects of the ground failure/settlement and culvert collapse are not within the scope of this numerical study. Additionally the presence of the reinforced concrete abutment on piles and its effect on the adjacent earth structure is not considered.

Commercially available program FLAC (Fast Lagrangian Analysis of Continua) was used for these analyses (Itasca Consulting Group 2000). FLAC uses an explicit finite difference scheme to solve static and dynamic problems. The program solves the equation of motion for mass-spring-dashpot systems in the time domain with incremental time steps. Calculated incremental displacements are related to incremental stresses in connection with selected

constitutive relationships. The program utilizes explicit time step integration between consecutive steps. In explicit time integration scheme a critical time step is selected to maintain computational stability (Belytschko 1983; Felippa and Park 1979; Goudreau and Taylor 1972; Hughes and Liu 1978a, 1978b; Hughes et al. 1979; Hughes 1983; Newmark 1959; Sander et al. 1979). Critical time step is related to the stiffness and size of the elements in the mesh. Smaller time step is required for stiffer and smaller elements. For example, in this analysis the critical time step is mandated by the reinforced concrete facing panels and steel strips, the stiffest elements in the model. Therefore, explicit time integration procedures require very small time steps to maintain computational stability, i.e. time steps as small as $10^{-6}$ seconds requiring about a million time steps for 1 second of dynamic time. Analysis of the model with a time history with 60 seconds duration takes about 4 hours with a Pentium 4 computer with 2.6GHz processor speed.

A suite of elements are available in the program to model continuum, structural elements and the interaction of continuum with structural elements. The continuum is divided into discrete segments where each discrete element is specified in space with four nodes defining its geometry. Nodal points defining each element are referred to as "gridpoints" and the area enclosed by the four gridpoints is referred to as "zone". Certain quantities such as displacement, velocity and acceleration are defined at the gridpoints whereas others (i.e. stresses, strains) are defined at the zones.

A variety of constitutive models are available in the program (i.e. elastic, inelastic, elasto-plastic). In addition to the built in models, the user can implement user-defined constitutive models using the FISH script available as a FLAC programming interface.

### 5.1. General Modeling Considerations

Although, some aspects of RE wall behavior are three-dimensional, the aspects important to this study are captured with two-dimensional analysis and thus, the two-dimensional version of FLAC (FLAC2D) was used, and a plane strain condition was assumed. The wall structure is sufficiently long in the longitudinal direction and therefore any movements in that direction are restrained (i.e. plane strain conditions). However, it should be noted that even though the wall is "sufficiently long" in the longitudinal direction, the height of the wall is

not constant throughout this length. The height varies smoothly over the length and there are no abrupt changes and this would provide sufficient constraint to minimize deformations in the longitudinal direction. This longitudinal dimension prevents any mode of motion and provides plane strain boundary conditions. The wall structure on one end has a reinforced concrete abutment structure on pile foundations. Such complications may be argued to require a three-dimensional analysis. Such a sophisticated analysis would be costly in terms of computation time.

The main mode of displacements is out-of-plane motions of the wall facing. And, the actual observed movements of the backfill soil and the facing panels were out-of-plane deformations. Even though the strips are discrete and not continuous (such as geotextile reinforcements) in the third-dimension, their interaction with the surrounding soil and within the whole structure is not three-dimensional. The discrete nature of the reinforcements can easily be averaged out in the third-dimension. Such an averaging process should be done with caution following certain scaling rules as discussed below.

Reducing three-dimensional problems with regularly-spaced beams, cables or piles to two-dimensional problems involves an averaging the effect in 3D over the distance between the elements. Stiffness properties of reinforcing elements and facing panels were scaled to reduce the three-dimensional problem to an equivalent two-dimensional plane strain cross section. Donovan et al. (1984) suggest that linear scaling of material properties is a simple and convenient way of distributing the discrete effect of the reinforcement over the distance between reinforcement in a regularly spaced pattern. For this purpose the element spacing, S, is used to scale the structural element properties (strength and stiffness). Basically, the value of the corresponding property is divided by S to obtain the averaged two-dimensional property. The FLAC manual has been reviewed for its convention on this issue and the suggested recommendations were followed. The manual provides the guidelines on scaling properties presented in Table 2-1. (Itasca Consulting Group 2000).

Dynamic numerical analysis using explicit time integration schemes poses a computational stability problem (Belytschko 1983; Hughes 1983). The time step between increments is maintained below a critical value to ensure computational stability. Incremental

displacements in the finite difference grid are calculated from the velocity field of the previous step. However, stability and accuracy are two distinct issues. The fact that stability is maintained does not automatically guarantee that the results of the analysis will be accurate. In explicit time integration, stresses and displacements are calculated by extrapolating the velocity field of the previous step. This means that displacements and stresses vary linearly in time, in between steps (i.e. assuming constant velocity between steps). It has been argued that keeping the time steps sufficiently small (like those small time steps in the order of $10^{-6}$ seconds that are required for stability) will also maintain an accurate solution. However, some unaccounted amount of error is transferred to the next step and this accumulates with each step because no iterations are performed in between steps to solve for equilibrium conditions. Equilibrium is not maintained in between steps and this brings the possibility of an unaccounted error term and inaccuracy to the dynamic solutions. Larger errors should be expected for dynamic analyses involving high degree of non-linearity and irrecoverable deformations. However, it is not possible to estimate the magnitude of those errors nor their effects on the results.

Table 2-1. Convention used in scaling structural elements

| **Structural Element** | **Properties to scale** |
|---|---|
| Facing panels | Elastic modulus of the beam<br>Ultimate moment capacity of the beam |
| Steel strips | Elastic modulus of the cable element<br>Yield strength of the cable element<br>Stiffness of the interface<br>Cohesive strength of the interface<br>Exposed perimeter of the cable element |

The FLAC program offers several structural elements such as cable elements, beam elements and pile elements to represent structural members in geotechnical engineering problems.

Interface elements are provided to define the interaction of the structural elements with the immediate media around (Itasca Consulting Group 2000).

For this study, cable elements were utilized to model the strip reinforcements. Cable elements are defined by their axial strength and axial stiffness properties as well as the interface characteristics between the cable and the surrounding media. Facing panels were modeled using beam elements where the axial and flexural stiffness properties are formulated.

Interface elements are used to define the connectivity between the facing panels and backfill soil. Cable elements which were used to model the reinforcements have built in interface characteristics. Therefore, it was not necessary to define separate interface elements for the reinforcements. Interface characteristics of cable elements are defined in a very similar fashion as interface elements, therefore the following discussion and explanations also apply to defining interfaces of cable elements as well as interface elements used for beam elements (i.e. facing panels).

Interface elements are available in FLAC to define the connectivity and interaction of beam elements with the surrounding media. Basic parameters used to define interfaces are described herein but the descriptions made here are limited to the parameters used in this model and may not cover the complete options inherent to interface elements available in FLAC. Interface elements are defined by their peak strength against sliding, normal and shear stiffness as well as the geometry of the nodes defining the connectivity of surfaces in contact. Shear strength of the interface is defined by a cohesion parameter and a friction angle. These parameters define the peak sliding resistance of the interface. Connectivity of the adjoining surfaces is established by a normal spring whose stiffness ($k_n$) related the normal stress along the interface in relation to relative normal displacement of the surfaces. Shear resistance along the sliding surface is related to the relative slip of the surfaces and the shear stiffness ($k_s$) of the interface.

$$\text{shear}_{\text{interface}} = \text{minimum } (k_n \cdot \text{relative slip, peak interface strength})$$

In cases where maximum interface shear is reached and slippage has already occurred, interface shear strength may change due to changing confinement/overburden. Even though the value of interface shear strength may change as the analysis progresses, in all cases shear stiffness of the interface is constant ($k_s$), unless this property is changed by the user through the course of the program.

Shear stiffness of the interface is estimated from pullout test reported in the literature (Christopher et al. 1989). These tests show the total slip versus pull-out force. Interpretation of reported test results in backcalculating stress versus displacement assumes uniform soil/reinforcement slip and shear stresses along the length of the reinforcement.

Reinforcement properties such as cross sectional area, perimeter, stiffness, strength, interface stiffness are scaled. Scaling of the strength and stiffness properties of the reinforcements were carried out at each level based on the quantity of reinforcement at each particular level. Scaling ratio (S) for each reinforcement elevation are calculated using the number of reinforcements at that level over panel width (1.5 meters).

$$S = \frac{\text{Number of reinforcements at elevation per panel}}{\text{Width of panel}}$$

Material property (reinforcement area, perimeter, stiffness, strength etc.) is multiplied by the scaling factor (S) to obtain the equivalent distributed property. In a way the material property is converted to a model property by this scaling. Such properties are scaled so that the concentrated forces (reinforcement forces and forces on the soil-reinforcement strip) are represented by equivalent stresses in the model.

The analyses considered the pre-earthquake condition of the wall by modeling the wall construction in a static condition, as well as a dynamic phase that simulated earthquake shaking. The static analysis was accomplished in stages simulating the sequence of construction, followed by the dynamic phase where the model was excited with a recorded acceleration time history from the 1999 Kocaeli Earthquake. Details of the analysis procedure and results are discussed below.

### 5.2. Model Geometry and Input Parameters

Two-dimensional plane strain analysis was performed for the cross-section of the highest portion of the double-wall reinforced earth approach embankment. The cross section of the analyzed wall geometry is shown in Figure 2-6. At this maximum wall section, the wall is 10 m high and 7 meter long steel strips with a cross-sectional area of 40 mm x 5 mm were used. Two levels of reinforcements are provided at each full size panel resulting in 75 cm vertical reinforcement spacing. The embankment is 12.5 m wide, resulting in a 1.5-m reinforcement overlap at the wall center for the cross section considered. The reinforcements were not connected at the overlap zone.

Design drawings indicate that the reinforcements were placed with a horizontal-to-vertical grade of 5%. Five strips were used per panel for the two lower panels and four strips were used for the upper panels at this maximum wall section being modeled. In cases where a half-size panel is used at the lowest level (i.e. left face of the wall analyzed), 2 or 3 strips were used per half-size panel. Half-size panels at the top of the wall have 2 strips each.

The components of the wall system are shown in Figure 2-36. This configuration of the facing panels represents the geometry of the wall section being analyzed. Left face of the wall consists of 6 panels whereas, 4 of the panels are full-size and the two at the bottom and the top of the wall are half-size panels. Right face of the wall consists of 7 panels, 6 of them being full-size and the one at the top half-size.

The model has five distinct zones: (1) foundation soil, (2) backfill reinforced with reinforcements, (3) facing panels, (4 and 5) the fill material in front of both faces. Foundation soil is in place at the base of the model and is 21.5 meters wide. The wall structure composed of backfill soil, reinforcements and facing panels rest on the foundation soil. Reinforced backfill is 12.5 meters wide with the left side of the backfill 9.4 meters high and the right side 10.1 meters. Fill is present in front of both faces of the walls. The wall structure and the front fills are connected to the foundation soil with interface elements and thus can slide on the foundation soil. The connectivity of these components (backfill, foundation, front fill and facing panel) at the wall base is shown in Figure 2-37.

The model cross-section was discretized into zones of different sizes as shown in Figure 2-38. Backfill is made up of zones of size 18.95 cm x 18.75 cm (horizontal vs. vertical). This element size was selected such that 8 levels of zones would match one facing panel of 150 cm. The backfill section was divided into 66 zones in the horizontal direction. The left and right sections of the backfill have 50 and 54 zones in the vertical direction respectively. Wider elements were used at the lateral sides of the model outside the reinforced backfill. The slenderness ratios of these elements are larger than generally recommended values. A summary of zone dimensions for various sections is given below in Table 2-2.

This discretization provided sufficient accuracy to capture the stresses and displacements in the soil and reinforcements, while keeping computation time within practical limits. The asphalt pavement and other structural elements on the top of the wall were not considered in the analysis.

Table 2-2. Size of different sections in the model and corresponding element sizes

| Section | Width (m) | Height (m) | Number of elements in the x-direction | Number of elements in the y-direction | Element size (m x m) |
|---|---|---|---|---|---|
| Foundation soil | 21.5 | 2.4475 – left<br>1.6875 – right | 78 | 13 – left<br>9 – right | 0.1895 x 0.1875 under backfill<br>0.50 x 0.1875 to 1.00 x 0.1875 under front fill |
| Backfill | 12.5 | 9.375 – left<br>10.125 – right | 66 | 50 – left<br>54 – right | 0.1895 x 0.1875 |
| Left front fill | 4.5 | 0.750 | 6 | 4 | 0.50 x 0.1875 to 1.00 x 0.1875 |
| Right front fill | 4.5 | 1.125 | 6 | 6 | 0.50 x 0.1875 to 1.00 x 0.1875 |

5.2.1. Soil Model

The foundation soil and the backfill were modeled using the Mohr-Coulomb soil model built into the FLAC code. This is an elasto-plastic model with a non-associated flow rule in which the yield surface is defined by the Mohr-Coulomb shear strength criteria. The stress-strain relationship is linear elastic below yielding, and the material attains plastic flow at yielding (Itasca Consulting Group 2000). The foundation soil was defined to have a cohesion of 150 kPa, $\phi = 40$ degrees, and a shear modulus of 15000 kPa. The backfill was assigned a $\phi = 40$ and a cohesion of zero.

Table 2-3. Mohr-Coulomb shear strength properties used in the analysis

| Zone | cohesion, c (kPa) | friction angle, $\phi$ (degrees) |
|---|---|---|
| Foundation soil | 150 | 40 |
| Backfill | 0 | 40 |

The stiffness of the backfill was stress-level dependent and these properties were updated during the analyses at each lift placement. After each level was placed, stiffness of the in-place backfill material was calculated using the confining pressure. Tangential values of bulk and shear modulus were defined to incrementally follow a hyperbolic stress strain relationship (i.e., Duncan and Chang 1970; Duncan et al. 1980). In this model, tangential Young's modulus, E, and Bulk modulus, B, are defined as:

$$E = \left[1 - \frac{R_f\left(1-\sin\phi\right)\left(\sigma_1 - \sigma_3\right)}{2\cdot\left(c\cos\phi + \sigma_3\sin\phi\right)}\right] K \cdot p_a \left(\frac{\sigma_3}{p_a}\right)^n$$

$$B = K_b \cdot p_a \left(\frac{\sigma_3}{p_a}\right)^m$$

where K, n Young modulus number and exponent

B, m Bulk modulus number and exponent

c, $\phi$ shear strength parameters

$\sigma_1$, $\sigma_3$ minor and major principal stresses

$p_a$ atmospheric pressure

The tangential Young's modulus was estimated through the model at each lift placement. As seen in the above formulation it is dependent on level of confining pressure as well as the deviatoric stress. However, once the value is assigned for the modulus it does not change throughout the analyses unless another update is performed for the next fill placement. Compressibility of the soil is defined by this assigned value of modulus below yielding.

Parameters typical of those used in previous numerical studies were selected to define the stress-level dependency of the backfill (Adib 1988; Schmertmann et al. 1989), as summarized in Table 2-4.

5.2.2. Structural Elements and Property Scaling

Interface elements were used to model the connectivity between the backfill soil and the facing panels. In FLAC, a contact logic is defined between each side of the interface by the use of normal and shear springs. The interface can be defined between adjacent soil surfaces along discontinuities, or between soil media and structural elements. The shear strength of the interface is defined by Mohr-Coulomb strength parameters. The shear strength of the soil/facing panel interfaces were assigned $\phi = 30$ degrees. Normal and shear spring stiffness of these interfaces were defined as $1.0 \times 10^6$ kN/m$^2$/m and $5.0 \times 10^3$ kN/m$^2$/m, respectively.

Steel strips were defined using cable elements in FLAC. Cable elements have a built-in feature that allows the user to define the element connectivity to the soil media without using interface elements. Shear strength of the reinforcement-soil interface is defined to have $\phi =$ 35 degrees. Cable elements are connected to the facing elements at one end at the corresponding nodes. Properties of the steel strip are summarized in Table 2-5.

Table 2-4. Model parameters of the backfill

| | |
|---|---|
| Unit weight ($kN/m^3$) | 21.0 |
| Young modulus number, K | 500 |
| Young modulus exponent, n | 0.5 |
| Bulk modulus number, $K_b$ | 300 |
| Bulk modulus exponent, m | 0.4 |
| Unload modulus number, $K_u$ | 800 |
| Failure ratio, $R_f$ | 0.80 |

Table 2-5. Properties of the reinforcements

| | |
|---|---|
| Width of steel strip (mm) | 40 |
| Thickness of steel strip (mm) | 5 |
| Perimeter of each single reinforcement (cm) | 9.0 |
| Area of each single reinforcement ($cm^2$) | 2.0 |
| Yield strength of steel reinforcement (MPa) | 450 |
| Elastic modulus of steel reinforcement (GPa) | 200 |
| Strength of each strip (kN/strip) | 90 |

In Reinforced Earth design practice, each facing panel has two levels of reinforcements and with half of the reinforcements at each level. In case when there is an odd number of reinforcements, most of the time the extra reinforcement is placed at the bottom level of the panel. As mentioned above, 5 steel strips were used in the lower panels (LP-6 RP-6 and RP-7). In these panels, 5 reinforcements were distributed equally as 2.5 strips at each level of the panel, instead of providing 3 and 2 strips at the top and bottom level of the panel respectively. This is a numerical simplification to overcome the uncertainty of reinforcement

placement at these panels. This equal distribution of reinforcements is an average of the two possibilities the reinforcement placement in these panels with 5 strips.

Lower panel at the left face (LP-7) is a half-size panel and these panels near the maximum wall height have 2 or 3 reinforcements as indicated by the as-built drawings. Similarly, 2.5 strips were assigned to this reinforcement elevation in the numerical model to represent this variable condition with an average.

Cross section of unit thickness (1 meter) is analyzed. Therefore, the reinforcement properties should be averaged over this dimension. The elastic modulus of the steel reinforcements, cross sectional area, and the perimeter of the strips were scaled per the actual reinforcement spacing, as recommended by Donovan et al. (1984). This scaling was performed to average out the discrete effect of the reinforcement and convert the system into an equivalent homogenous force system throughout the unit wall width. Scaling ratio (S) for the reinforcement levels with 2 and 2.5 strips were calculated as 1.33 and 1.67 respectively.

The connectivity of each zone was defined using interface elements. This was done to allow for slip displacement between these zones. Interface elements were also used between the backfill soil and the facing panels.

Table 2-6. Scaled properties of the reinforcements per unit thick model

| Panel | Strips/panel at each level | Area ($cm^2$) | Perimeter (cm) | Tensile strength (kN) | Young's modulus (kPa) | Interface shear stiffness (kPa) |
|---|---|---|---|---|---|---|
| LP1 – LP5<br>RP1 – RP5 | 2 | 2.67 | 12 | 120 | $2.67 \times 10^8$ | $0.8 \times 10^6$ |
| LP6, LP7,<br>RP6, RP7 | 2.5 | 3.33 | 15 | 150 | $3.33 \times 10^8$ | $1.0 \times 10^6$ |

Facing panels are continuous in the longitudinal direction (in-plane dimension of the 2D model). Therefore, properties for those structural elements are not scaled. However, the

elastic modulus of the facing panel has been modified by the following formula to account for plane strain conditions;

$$E_{planestrain} = \frac{E}{1-\nu^2}$$

where;

E = Young's modulus of concrete

ν = Poisson ratio of concrete

Using a Young's modulus of 2.0 x $10^7$ kPa and a Poisson ratio of 0.2 the modulus in plane strain conditions was estimated as 2.08 x $10^7$ kPa for the facing panels. As can be seen this does not bring in a significant difference especially at these conditions where an average modulus is selected for lightly reinforced concrete. Properties of the facing panel used in the analysis are summarized in Table 2-7.

Table 2-7. Properties of the facing panels

| | |
|---|---|
| Unit weight (kN/m$^3$) | 23.0 |
| Panel thickness (cm) | 15 |
| Cross sectional area | 120.0 |
| Moment of inertia | 2.67 x $10^8$ |
| Young's modulus (kN/m$^2$) | 2.0 x $10^7$ |
| Poisson's ratio | 0.2 |
| Scaled Young's modulus for plane strain | 2.08 x $10^7$ |

## 5.3. Static Analysis and Results

A static analysis was performed to model the pre-earthquake conditions of the wall. This modeling phase was important because static equilibrium stresses within the backfill and the reinforcing strips are likely to play a major role in the dynamic behavior of mechanically-stabilized earth wall. Therefore, it was important to assess the initial conditions of the wall to our best. Sequential analysis was performed to simulate the wall construction procedure.

The effects of compaction were also modeled in the analyses by applying and removing a surcharge pressure on each lift. Because the wall is built in compacted soil lifts, it is likely that reinforcement forces especially in the upper layers will be affected by the compaction effort. This is generally true for earth retention systems with inextensible reinforcements (comparably stiffer reinforcements and facing panels) where the structure does not have as much flexibility to deform laterally.

Linear elastic-fully plastic material model is used at this stage of analyses. Backfill material behaves linearly elastic before yield strength is reached and attains plastic flow under constant shear stress after yield. Yield strength of the backfill is defined by its friction angle ($\phi'$) and it is updated at each stage as the stress conditions change (due to increased overburden and/or deformations). The effect of volumetric changes on shear strength (i.e. dilational/compressional volumetric strains) is not accounted for in these analyses. The shear strength of the material is solely dependent upon its friction angle ($\phi'$) and state of stress.

### 5.3.1. Sequential Construction

Lifts were placed in steps as each panel was placed and reinforcements were introduced at their corresponding levels. Soil strength and stiffness was updated at each step to account for the most recent stress state. A panel is placed and initially the top node of the panel is fixed as the backfilling behind that panel is in progress. One level of backfill is placed and let to reach static equilibrium under self weight. Reinforcements are introduced at the same step where the lift of their elevation is placed. Each panel is backfilled in four stages where panels are 150 cm high with each level of lift is 37.5 cm thick (two elements thick). Node restraints are removed after backfill placement behind the panel is completed.

The following sequence was followed for each lift placement stage.

1) Figure 2-39 shows the system in equilibrium with 2 facing panels on each side. At this state, 6 and 8 lifts are in place on the left and right sides of the model. The first panel on the left side is a half-panel bearing 2 lifts behind. Base of the model is fixed for displacements in the vertical direction. Lateral sides of the model are fixed for horizontal displacements. Facing panels are connected by hinges. As this model came to equilibrium from the previous state, the equilibrium stress conditions are used to update the strength and stiffness properties of the model.

2) Panels on each side of the wall face are placed as shown in Figure 2-40. Connection of the new panel to the panel below is initially specified as moment carrying. Top node of the new panel is also fixed for horizontal displacements.

3) The new lift is placed by switching the model properties of the corresponding soil zones from null to Mohr-Coulomb. Vertical displacements of the nodes of the previous lift are subtracted from the nodal coordinates of the newly introduced fill. This ensures that the vertical compression of the backfill in-place is not reflected as deformations or geometrical unconformities on the newly placed fill.

4) As the new lift is placed initial stresses are assigned to this newly introduced soil mass to represent the body forces. These initial stresses in the new lift are determined from geostatic stress conditions (i.e. vertical stresses from self weight and horizontal stresses half the vertical stresses). Introduction of these initial stresses to the newly placed soil elements is important because their strength and stiffness is solely determined by the stress state. Soil strength/stiffness values updated and the system was brought to equilibrium under this additional load.

5) Stiffness and strength values were updated under the new stress state of the current equilibrium.

6) A surcharge load of 20 $kN/m^2$ (tapered to 5 $kN/m^2$ near the wall face) was applied at the top of the recently placed lift of soil as shown in Figure 2-41. The system again brought to equilibrium under this surcharge load. Soil strength/stiffness values updated and the system was brought to equilibrium under this additional load.

7) The surcharge load was removed and once again the system brought to equilibrium and the strength/stiffness properties were updated.

8) A new lift placed as shown in Figure 2-42, while the same boundary conditions are held (i.e. horizontal constraint of the top of the facing panel and moment connection between the uppermost panel and the panel below). A single level of reinforcement is placed on each side. The end of the reinforcements are attached to the facing panels. The system is again brought to equilibrium under this surcharge load. The soil strength/stiffness values updated and the system was brought to equilibrium under this additional load.

9) Fill placement, surcharge load application and removal, reinforcement placement continued until the 4 lifts are in place for the upper facing panels.

10) As 4 lifts are in place and the system is in equilibrium as seen in Figure 2-43, horizontal fixity of the top of the facing panels is released. Moment fixity at the facing panel connection is released and a hinge is defined at the connection. The system again brought to equilibrium in response to this disturbance and the strength/stiffness values updated before new facing panels are placed for the new levels.

5.3.2. End-of-construction deformations

Displacement vectors are shown Figure 2-44 for the model at the end of static analysis. Maximum horizontal displacement occurs at the top of the wall. Maximum horizontal displacement of the wall top is about 4 cm which is about 0.4% of the wall height. Horizontal displacements form a larger component of the displacements at the top portions of the wall whereas displacements in the lower parts of the wall are vertically aligned.

Profiles of horizontal displacement along the left and right faces of the wall are shown in Figure 2-45. Locations of the base of the wall and the top of the in-front fill are also shown in the figure. Peak horizontal displacement occurs at the wall top and it is about 3 and 4 cm for the left and right wall face respectively. Total lateral deformation at wall top is 7 cm and this corresponds to 0.56% strain in reference to the width of the wall = 12.5 m.

Values of vertical displacement at the top of the wall and at different elevations within the wall are shown in Figure 2-46. Top of the wall has settled about 1 cm in a fairly uniform pattern. Settlement near the center is slightly larger than on the sides. The same settlement pattern is observed at elevations near the wall top (z = 1 meters and z = 2.5 meters). Larger settlements near the middle of the wall are caused by the horizontal displacements of the wall faces. Larger settlements are observed at mid-height of the wall and below (z = 5 meters and z = 7.5 meters). Settlement distribution is more uniform at these elevations, because lateral displacement of the wall face is much more limited.

5.3.3. End-of-construction stresses in the backfill and reinforcement forces

Vertical stress contours are shown in Figure 2-47. Vertical stresses are close to geostatic stresses in the middle sections of the model and smaller than geostatic stresses are present near the wall facing. This zone of reduced vertical stresses is about 1.5-2.0 meters wide behind each wall face. High stress gradients are evident at the toe of the wall faces. The toe of the wall is a geometric discontinuity and stresses vary significantly in short distances. Horizontal stress contours are shown in Figure 2-48. High horizontal stresses are present in the foundation soil and fill outside the footprint of the backfill. Shear stress ($\sigma_{xy}$) contours are shown in Figure 2-49 and it is seen that maximum shear stresses are attained near the toe of the wall. Similarly, contours of earth pressure coefficient (K) in the model are shown in Figure 2-50. It is seen that ratio of the horizontal stresses to vertical stresses are about 0.2 – 0.3. Smaller values are observed in the middle sections of the wall and larger near the wall face.

Vertical and horizontal stresses for various sections in the backfill along wall height are plotted in Figure 2-51. As seen the vertical stresses are very close to geostatic stresses. Smaller values of the vertical stresses correspond to locations near the wall face. Horizontal stresses show more scatter. It is not possible to indicate a certain specific trend because of the scatter. At the top 4-5 meters of the wall earth pressures vary between active earth pressure conditions ($K_a$) to larger than at-rest ($K_o$) conditions. Below the top 4-5 meters of the wall, horizontal earth pressures are scattered between values that correspond to active and at-rest earth pressure conditions.

Maximum values of reinforcement forces are plotted in Figure 2-52 along with the upper and lower bound of design forces. Design bounds correspond to reinforcement forces calculated using earth pressure coefficients $1.2K_a$ and $1.7K_a$. Upper bound earth pressure coefficient ($1.7K_a$) is equal to 0.370 for this case ($\phi$=40 degrees) and this value is very close to at-rest earth pressure coefficient, $K_o$ = 0.357. It is seen that the peak reinforcement force at the top 5 meters upper slightly lower than the lower bound curve ($1.2K_a$) close to about an active earth pressure coefficient. Calculated peak reinforcement forces are plotted in Figure 2-53 along with limit equilibrium design values and the ultimate reinforcement capacity as defined by the minimum of tensile and pullout resistance.

Calculated peak reinforcement forces are used to estimate the factor of safety at the end of construction by comparing the calculated reinforcement forces with the ultimate capacity values. These are shown in Figure 2-54 and they are compared with the static design values calculated previously. It is seen that design values and values from calculated reinforcement forces are in close agreement. This is an indication that current design methods do a reasonable job of predicting working-stress reinforcement forces.

The distribution of reinforcement forces at the end of static analysis is shown in Figure 2-55 and Figure 2-56 for the left and right face reinforcements respectively. Location of the peak force is shown in the figures along with the extent of forces larger than 95% of the peak force at that reinforcement level. The zone of maximum reinforcement force is wide in extent. This shows that there is not a zone of strong shearing to produce a distinct peak reinforcement force. This is reasonable for working stress conditions where stress conditions are not as high as those near failure state. The sum of the end-of-construction peak reinforcement forces for the left and right walls are 252.4 kN/m and 285.2 kN/m respectively. These forces are for the unit width of the plane strain model.

### 5.4. Dynamic Analysis and Results

Dynamic analyses were carried out to simulate earthquake shaking. Horizontal shaking was applied at the base of the model following static analysis. These analyses focused on investigating the effect of shaking intensity on the permanent deformations and maximum reinforcement forces among others.

Stiffness of the backfill and the foundation soil were calculated from the end-of-construction stresses of the static analysis phase. Likewise, the shear strength of the backfill and foundation soil followed the Mohr-Coulomb criteria described above. Stress-strain behavior is assumed linear-elastic below yielding, and plastic flow is assumed at the yielding stress.

The east-west component of the acceleration time history recorded at the YPT (Yarimca Petkim) Station during the Kocaeli Earthquake was used in the analysis. The YPT Station is about 40 km from the Arifiye site and located on ground conditions similar to those at Arifiye. The acceleration record was baseline-corrected, and frequencies above 15 Hz were removed by low-pass filtering. Baseline correction of the raw time history is performed to achieve zero ground velocity at the end of the record. Acceleration time history is demeaned and detrended for this purpose. Removal of high frequency components was needed to ensure that the input motion can transmitted within the finite difference grid without being distorted (Kuhlmeyer and Lysmer 1973). An additional filtering process was performed to achieve a zero displacement at the end of the record. Low frequency components (0.025 Hz) were removed with a high-pass filter for this purpose.

Acceleration and velocity time histories of the record after filtering are shown in Figure 2-57. As seen, peak ground acceleration reaches 0.234g and peak ground velocity reaches 69.5 cm/s. The record is 60 seconds long with the strongest episode of shaking occurs at the first 15 seconds of the record. There is a second-shock between 35-40 seconds. This part of the recording is composed of high frequency components in the acceleration record therefore not yielding much ground velocity and displacement as seen from velocity and displacement time histories between 35-40 seconds.

Positive values of the record correspond to motions in the East direction and thus the right face of the wall (as seen looking North). The peak value of the acceleration (0.234g) occurs in the positive direction corresponding to +East direction. The peak acceleration along the other direction (-West) is 0.221g.

Response spectra for pseudo-spectral acceleration (PSA), spectral velocity (SV) and pseudo-spectral velocity (PSV) are shown in Figure 2-57. The predominant period of this time history, as defined by the period with the peak pseudo-spectral acceleration, is 0.53 seconds.

It is seen from the pseudo-spectral acceleration response spectra the record has a wide range of peaks within the oscillator periods 0.2 to 0.8 seconds.

The input acceleration motion was applied at the base of the model. Free-field boundary conditions were imposed at the sides of the model using the free-field boundary feature built in FLAC. This enabled truncation of the sides of the model close to the wall faces while still maintaining the condition of vertically-propagating shear waves at the boundaries.

For the dynamic analysis, several key parameters were monitored throughout the duration of ground shaking. Of primary interest were the displacements along both faces of the wall and the wall centerline, and the maximum forces along the length of the reinforcements. The deformed shape of the grid at the end of shaking is shown in Figure 2-58. It can be seen that the wall settled along the centerline and bulged laterally near the base. A predicted maximum permanent lateral deformation of 13-17 cm occurred about one-third of the wall height above the base. This prediction agrees well with the actual measured peak lateral displacement of 10 cm that occurred near the bottom of the wall.

Displacements were monitored during the analysis at many locations within the model. Main focus of the monitoring was the displacements at the wall faces. Moreover, displacements were also monitored at several locations within the wall. Nodal history points were selected such that the model was covered with uniformly distributed points. Vertically-aligned nodal points were selected to form vertical arrays. Each vertical array is composed of 19 nodal points that are equally spaced (0.5625 m corresponding to every third grid point spacing within the model). A schematic of the monitored data points are shown in Figure 2-59. Nodal points along the vertical arrays at each wall face are shown individually whereas only the vertical arrays are shown for the inside points for brevity purposes.

Similarly, horizontal stresses were monitored during the analysis within the model. Horizontal stresses were monitored at several locations within the wall. Vertically-aligned nodal points were selected to form vertical arrays. Each vertical array is composed of 27 points that are equally spaced (0.375 m corresponding to every 2 grid point spacing within the model). A schematic of the monitored data points are shown in Figure 2-60. History

points along the vertical arrays behind each wall face are shown individually whereas only the vertical arrays are shown for the inside points for brevity purposes.

Variation of peak acceleration within the model is shown in Figure 2-61. Points of peak acceleration at each monitored point are plotted along with the average line which is defined as the mean of the peak acceleration values of the various points at the same elevation. It is seen that the motion is deamplified throughout the model. There is some amplification from 2 meters from the top of the wall to the top of the wall. The motion is amplified from about 0.1g at 2 meters depth to 0.17g at the top of the wall. This is the free surface effect when a wave hits a stress free surface the upgoing wave and the reflected wave combine constructively to double the amplitude.

The results are provided Figure 2-62 and Figure 2-63 in the form of displacement time histories for the right and left wall faces, respectively. Displacement time histories of 10 points along each face are provided for every other monitored point (1.125 meters vertical spacing of reported histories). These time histories present the relative displacement at these points with respect to their at-rest positions at the end of static equilibrium. They are not directly a measure of deformations. However, when these displacement time histories are compared to those at the base of the model (bottom graph in each figure) there appears a certain lagging between the upper history points and the base input motion. Displacement time histories deviate from the input motion throughout shaking resulting in a permanent offset at the end of shaking. The magnitude of end-of-shaking permanent displacements is a measure of the out-of-plane misalignment of the wall facing at those respective points.

Although a useful indication of permanent deformations, these displacement histories do not directly provide quantitative information on the magnitude of lateral deformations. They are a measure of the lateral displacements along the wall facing but it is actually the relative displacements of points on each side of the wall that indicate if that particular elevation suffered lateral deformations (out-of-plane deformations of the wall faces; extension/compression of the model cross section).

A better measure of deformations can be the relative displacements of respective points on each side of the model. Relative displacements of nodal points on each face of the wall

correspond to the horizontal deformation along the wall cross section. Positive values indicate extension and negative values correspond to compression along that particular elevation of the model. The sketch in Figure 2-64 shows how the horizontal wall deformations are calculated. As seen, total deformation at an elevation is the relative displacement of respective points on each side of the model. This is a measure of change of length of the original wall geometry and directly gives horizontal deformation throughout wall height and thus horizontal strains.

$$\Delta hor_i = xdisp^{right}{}_i - xdisp^{left}{}_i = Deformed_{total} - L_{total}$$

$$\varepsilon^{hor}{}_i = \frac{\Delta hor_i}{L_{total}(=12.5m)}$$

Similarly, deformations of the left and right sections of the model are calculated using the relative displacements of the nodes at the respective faces and the nodal points along the centerline of the model as shown in Figure 2-64. Even though the left and right sections of the structure are not distinct and independent features, this can give an idea on the directionality of the shaking. Both faces of the wall are very similar in geometry and design. Shaking is different in each direction, but both directions are similar in terms of average characteristics (i.e. peak acceleration and velocity). Even though deformations on each section of the wall are out of phase, they have similar magnitudes of end-of-shaking permanent deformations.

Horizontal deformations at several elevations (point 1 at the top of the wall and point 19 at the base of the wall) during shaking are presented in Figure 2-65. As specified above, lateral deformation is calculated from the relative displacement of nodal points at each facing (displacement history at the left subtracted from that displacement history at the right of the same elevation).

As seen, the time histories suggest that the majority of the deformations developed during the episode of stronger ground shaking (between 4 to 15 seconds of shaking). Some additional

deformation is accumulated between 35-40 seconds where there is a second episode of strong shaking.

Lateral deformation values at the end of shaking are shown in Figure 2-66. Values are provided for left and right sections of the model along with the total deformations. Average deformation is defined as the average of the absolute values of deformations along the wall height. Peak deformation is the maximum extensional deformation along the height of the wall. As seen left and right wall sections show similar behavior in terms of the deformation pattern. The maximum of 13.0 and 16.7 cm out of plane deformation occurs at about 7 meters from the top of the wall for left and right walls respectively. The total deformation, which is the sum of each section, is also plotted to yield 28.7 cm peak out-of-plane deformations. It should be noted that the maximum total deformation is not simply the addition of the maximums at left and right walls because the peaks at each section occur at slightly different elevations. The peak maximum deformation is the peak of the sum of the deformations of left and right sections.

Both the deformed shape at the end of shaking and the interpreted deformation measurements show that bottom half of the wall bulged out whereas the upper sections of the wall merged in. The bulging at the lower half and compression at the upper half resulted in settlement at the crest of the wall. The predicted top-of-wall settlement (along the centerline) was 27 cm, and this was due primarily to the lateral deformation of the system. This settlement prediction is consistent with the observed settlement that was estimated in the range of 25-30 cm.

Lateral deformation histories for individual points were plotted in Figure 2-66. Average deformation calculated from these points for left and right sections and the total wall section are plotted in Figure 2-67. Similarly, a majority of the deformations developed during the episode of stronger ground shaking (between 4 to 15 seconds of shaking). It is also seen that the deformation accumulation of left and right wall sections are out of phase. As one section is undergoing episode of deformation accumulation, the other section is more or less staying undeformed. Deformations develop in one direction as the shaking occurs in that particular direction. One other point is that the deformations do not “recover” even when the shaking

direction is reversed. These observations are better presented in Figure 2-68 where the same results are presented for the period of strong shaking when the majority of deformations occur.

The rate of average deformation is also shown in Figure 2-69. This is the time derivative of the deformation results shown previously. Large values of deformation rate correspond to episodes where majority of the deformations are taking place. As seen, most of those are between 4 to 15 seconds. It should also be pointed out that the deformation rate slightly falls to negative values momentarily; another indication that the deformations are permanent and are not recovered during shaking. Similarly the same results are better presented in Figure 2-70 for the period of strong shaking where most of the deformations take place.

Earth pressures were monitored within the model throughout the dynamic analysis. Of particular interest were the peak values and end-of-shaking values of the earth pressures and how these correlated to at-rest ($K_o$) and passive earth pressure states at the respective points. Earth pressure histories at several locations along the left and right face of the wall are shown in Figure 2-71 and Figure 2-72 respectively.

Total earth thrust behind left and right faces are shown in Figure 2-73 and Figure 2-74. It is seen that the static values of horizontal earth thrust (total earth pressure behind facing for unit width wall) for both faces are very close to at-rest geostatic values predicted by $K_o$ earth pressure coefficient. Maximum values of earth thrust increase to 4 times the initial static (and at rest) earth pressures. At the end of shaking the earth thrust is about twice the static values indicating that a significant amount of horizontal earth pressure is locked in the system as a result of induced permanent deformations.

The depth of action of the total earth thrust is calculated from the distribution of earth pressures and the results are presented in Figure 2-75 and Figure 2-76 for the left and right sections respectively. The total earth thrust act at about 2/3 of wall height from the wall top for both faces. The point of action of the total earth thrust varies between 0.5H to 0.8H from the wall top during shaking.

Initial, peak, and end-of-shaking horizontal earth pressures are plotted in Figure 2-77. As discussed above the initial earth pressures are very close to at-rest ($K_o$) earth pressure

distribution. Peak values of earth pressures are bound by the passive earth pressures ($K_p$) which is limited by the shear strength of the soil. Peak values of earth pressure at the top 2 meters are very close to the passive earth pressure boundary indicating that the soil has failed at those locations during shaking. End-of-shaking earth pressures for both walls are also shown.

Reinforcement forces were also monitored throughout the dynamic analysis. Peak reinforcement forces along the left and right walls are shown in Figure 2-78 and Figure 2-79 respectively. The peak reinforcement force at some levels is capped by a maximum value where the reinforcement force reaches either the maximum tensile strength or pullout resistance.

The sum of the peak reinforcement force at each wall are shown in Figure 2-80 and Figure 2-81. Maximum values of total reinforcement force increase to four times the initial static values. The same results are shown in Figure 2-82 with a more detailed examination. It is seen that the total reinforcement force at the left and right walls are out of phase as expected and as evidenced previously from the deformations. The equivalent depth of action of the reinforcements force is calculated and the results are presented in Figure 2-83 and Figure 2-84 for the left and right walls respectively. The total reinforcement force acts equivalently at about 2/3 of wall height from the wall top for both walls. The point of action of total reinforcement force varies between 0.6H to 0.7H from the wall top during shaking which is a narrower range than that of the earth pressures.

Peak and end of shaking values of reinforcement forces are plotted in Figure 2-85. Peak reinforcement forces are shown in Figure 2-86 in comparison to design values calculated using $k_h = 0.285$ ($k_h = (1.45 – 0.234)(0.234)$ where 0.234g is the peak base acceleration as in this case). As seen the peak reinforcement forces that develop during shaking are significantly higher than those predicted by the design method. In fact they are even higher than the reinforcement resistance envelope which is mainly a function of pullout resistance of the length of reinforcement in the passive zone. However, what happens to be an absolute upper bound is the envelope defined by the tensile strength and the pullout resistance of the full-length of the reinforcement. In both resistance envelopes, the pullout governs as opposed

to the tensile resistance because tensile resistance is larger than pullout resistance (both for passive zone length and full length) except at several bottom level reinforcements.

Calculated values of maximum reinforcement forces are compared with the reinforcement resistance envelope (minimum of tensile resistance and pullout resistance of reinforcement length in the passive zone) as defined by the design procedures and the results are shown in Figure 2-87. Also plotted is the variation of the factor of safety predicted by the design methods using $k_h = 0.285$. It is seen that the factor of safety falls significantly below 1.0 to values around 0.6 if the calculated demand is compared with the predicted capacity envelope. This demonstrates several key issues. First, the fact that the design method underpredicts the peak reinforcement forces (i.e. demand) is different than the predicted reinforcement resistance (i.e. capacity). Reinforcement forces predicted by the design methods are much lower than those developed throughout the numerical analysis. On the other hand what appears to be a resistance envelope is also larger then the resistance envelope predicted by the design methods. When fully loaded, the full length of the reinforcement contributes to the pullout resistance.

Calculated peak reinforcement forces are compared with the resistance values that correspond to the minimum of tensile resistance and full reinforcement length. The results are shown in Figure 2-88. It is seen that calculated peak reinforcement forces are very close to the maximum capacity envelope resulting in factor of safety values ranging between 1.0 and 1.2.

Even though the peak reinforcement forces were very close to the maximum capacity, the model still did not collapse but has undergone permanent deformations. Current design guidelines are not reliable predictors the seismically induced reinforcement forces. Much larger forces developed in the numerical analysis. However, this still did not lead to a collapse, but rather, resulted in significant permanent wall deformations. This demonstrates the shortcomings in the predictive capability of the current design methods, as well as the need to predict permanent deformations as an additional performance criterion of wall behavior.

Finally, it should be noted that that no slip surface or failure wedge developed in the backfill during analysis, although enough vertical and horizontal displacement occurred to present potential serviceability problems for the walls. The predicted settlement of the overlying roadway was substantial in close agreement with the post-earthquake observations. Thus, in terms of the overall seismic performance of RE walls, the numerical analyses suggest that displacement is likely to be the controlling criterion as opposed to shear failure.

Also, the analyses indicated that it is likely that enough out-of plane movement of the facing panels would occur to allow spillage of the backfill long before a pronounced slip surface would develop. Even though these analyses did not consider the separation of the panels, (i.e. panels were connected by hinges) the magnitude of deformations is large enough to potentially create openings between the panels.

### 5.5. Parametric Analyses

Series of analyses were performed for several cases to investigate the effects of shaking intensity and design factor of safety on seismic performance. Of primary interest was the permanent displacement of the model in response to simulated shaking. Additionally the reinforcement forces were monitored throughout shaking to relate peak values of total reinforcement forces to base acceleration.

Dynamic analyses were carried out following the static phase to simulate earthquake shaking. Horizontal shaking was applied at the base of the model in static equilibrium. The earthquake record was scaled to different values between 0.023g to 0.398g involving a total of 21 cases including the base analysis described above. The base analysis was shaken with the baseline corrected East-West component of the YPT record. Peak ground acceleration values in the East and West directions for this record are 0.234g and 0.221g, respectively. This record was simply scaled in the time domain with scaling coefficients ranging between 0.1–1.7. Results of the analyses are briefly summarized below in Table 2-8.

Average deformation and peak deformation at the end of shaking increase with shaking intensity. Figure 2-89 shows the results of the analyses for end-of-shaking average deformation in relation to peak acceleration applied at the base. Similarly, Figure 2-90 shows how end-of-shaking peak deformation varies with peak base acceleration. Average

deformation is defined as the average of the absolute value of lateral deformations along the height of the wall. Peak deformation is the maximum value of the end-of-shaking lateral deformations along the height of the wall. Both observations of deformations show similar trends.

Higher acceleration levels result in larger deformations. However, the data do not suggest a "breakdown" acceleration to correspond to a threshold level after which deformations increase at a faster rate. Average deformation is less than 10 cm for acceleration levels smaller than 0.2g. Average deformation ranges between 20-30 cm, for acceleration levels between 0.3-0.4g.

The same deformation data is plotted in Figure 2-91 and Figure 2-92 in terms of peak base velocity. Average deformation and peak deformation are less than 10 cm and 20 cm respectively for peak base velocity smaller than 0.6 cm/s. Average deformations as large as 30 cm are calculated for peak base velocity levels around 1.0 cm/s.

Acceleration history is monitored at several points along the wall during the analyses. Variation of peak acceleration within the wall is shown in Figure 2-93 for various levels of base shaking. It should be noted that base motion is amplified for low levels of motion, whereas it is deamplified for moderate to high levels of shaking. This observation is related to how the level of non-linearity affects the motions within this earth structure. The stronger the shaking, the more non-linearity, and as a result more energy is dissipated within the system, resulting in lower acceleration levels at the top of the wall.

It is apparent from the graph how motion is amplified to about twice its value at the top of the wall in comparison to peak acceleration at about 2 meters below the top. This is obviously a free-surface effect where the up-going wave and the reflected motion interfere constructively at a free end of a vibrating system.

Another observation from the acceleration data is the way peak acceleration is enveloped. As the acceleration level is increased the peak acceleration within the wall is bound by an envelope. This is probably related to the level of acceleration that can be sustained by the shear strength of the system. Acceleration is a direct measure of the inertial forces exerted on the system due to shaking. The envelope is an indirect measure of the shear strength of the

soil in relation to the peak acceleration. Higher acceleration levels can be sustained at lower levels in the model because the strength of the soil is confining pressure dependent.

Table 2-8. Summary of the parametric analyses

| scaling ratio | PGA (g) | PGV (cm/s) | average def. (cm) | peak def. (cm) | peak dyn. reinforcement force (kN/m) |
|---|---|---|---|---|---|
| 0.10 | 0.0234 | 0.0324 | 0.08 | 0.36 | 280.7 |
| 0.20 | 0.0469 | 0.0526 | 0.31 | 0.42 | 434.4 |
| 0.30 | 0.0703 | 0.0688 | 0.74 | 0.99 | 458.2 |
| 0.40 | 0.0937 | 0.0867 | 1.62 | 1.73 | 524.3 |
| 0.50 | 0.1172 | 0.1054 | 2.92 | 3.40 | 538.8 |
| 0.55 | 0.1289 | 0.1123 | 3.64 | 4.72 | 543.2 |
| 0.60 | 0.1406 | 0.1188 | 4.29 | 6.09 | 580.9 |
| 0.65 | 0.1523 | 0.1245 | 5.27 | 6.78 | 596.6 |
| 0.70 | 0.1641 | 0.1332 | 5.94 | 9.05 | 601.8 |
| 0.75 | 0.1758 | 0.1396 | 7.56 | 12.14 | 635.7 |
| 0.80 | 0.1875 | 0.1441 | 8.42 | 13.85 | 660.7 |
| 0.85 | 0.1992 | 0.1524 | 9.74 | 17.86 | 674.9 |
| 0.90 | 0.2109 | 0.1577 | 10.61 | 18.35 | 704.1 |
| 0.95 | 0.2226 | 0.1623 | 12.15 | 24.89 | 722.8 |
| **1.00** | **0.2344** | **0.1646** | **13.81** | **28.69** | **752.1** |
| 1.10 | 0.2578 | 0.1736 | 14.99 | 38.16 | 752.0 |
| 1.20 | 0.2812 | 0.1945 | 17.46 | 39.52 | 765.7 |
| 1.30 | 0.3047 | 0.2018 | 20.66 | 49.88 | 839.2 |
| 1.40 | 0.3281 | 0.2082 | 23.57 | 61.98 | 854.1 |
| 1.60 | 0.3516 | 0.2241 | 25.03 | 66.44 | 900.1 |
| 1.70 | 0.3984 | 0.2286 | 28.94 | 82.26 | 937.9 |

The ratio of peak acceleration at the top of the wall to the peak acceleration applied at the base for various shaking intensities is shown in Figure 2-94. The base acceleration is amplified for values smaller than about 0.15g. An amplification ratio of about 2 is observed at low acceleration levels. The peak acceleration at the top of the wall is about 70-80% of the peak base acceleration for levels about 0.3-0.4g.

In many cases, average peak acceleration within the wall can be a better measure of the inertial forces the system experiences. The ratio of average peak acceleration within the wall to peak base acceleration is shown in Figure 2-95. The ratio that corresponds to seismic coefficient recommended for design (AASHTO 1996) to base acceleration is shown for comparison.

Peak horizontal thrust behind the left and right wall faces for different levels of base acceleration are shown in Figure 2-96 and Figure 2-97 respectively. It is seen that in both cases the horizontal thrust for static case (peak base acceleration = 0) is very close to at-rest conditions denoted by $K_o$ earth pressure coefficient ($K_o$ = 0.375 for $\phi$ = 40 degrees). The increase in horizontal earth thrust becomes marginal for base accelerations higher than 0.2g.

Total reinforcement force at the left and right faces are shown in Figure 2-98 and Figure 2-99 respectively for various acceleration levels. Below are three formulations to predict peak reinforcement force. Case A corresponds to the current design method where the seismic force is calculated from the horizontal inertia force of the passive zone. The weight of the passive zone is multiplied by the seismic coefficient ($k_h$) to find the seismic inertia force. As seen in the figures and as demonstrated in the previous section, this formulation significantly under-predicts the reinforcement forces.

$$\text{total force} = \text{static force} + \text{seismic force} = P_{st} + P_I = P_{st} + \left(\frac{3}{4}\right) 0.3\gamma H^2 k_h \quad \text{– (Case A)}$$

In Case B, seismic force is calculated similarly using the inertia of the whole wall (12.5 meter wide double wall). The total weight of the whole wall is multiplied by the seismic

coefficient ($k_h$) to find the seismic inertia force. This relationship shows a fairly good fit to the calculated forces.

$$\text{total force} = \text{static force} + \text{seismic force} = P_{st} + P_I = P_{st} + \gamma HWk_h \quad - \text{(Case B)}$$

As a third alternative the total force (static and seismic) is calculated using a combined earth pressure coefficient which is the sum of the at-rest earth pressure coefficient ($K_o$) and the seismic coefficient. It is seen that even though this is an improvement over the current design methods (Case A), this still under-predicts total reinforcement forces.

$$\text{total force} = \text{static force} + \text{seismic force} = P_{st} + P_I = \frac{1}{2}\gamma H^2\left(K_o + k_h\right) \quad - \text{(Case C)}$$

Peak horizontal thrust behind the left and right wall faces for different levels of peak base velocity are shown in Figure 2-100. Similarly, maximum total reinforcement force is plotted in Figure 2-101 with respect to peak base velocity. Peak total reinforcement force in relation to average permanent deformation is plotted in Figure 2-102. Also, end-of-shaking reinforcement forces are shown in Figure 2-103 in relation to average permanent deformations. Initially, it seems reasonable to expect larger locked-in reinforcement forces in relation to larger deformations. However, this figure suggests that there is no direct correlation.

The location of action of the equivalent peak horizontal earth thrust is shown in Figure 2-104 for various base acceleration levels. Three different graphs are presented including upper-bound and lower-bound values of location of action as well as the end-of-shaking locations. Upper-bound values are the minimum values of the location of action (depth / wall height) throughout shaking and show the uppermost elevation the equivalent earth thrust acts during shaking. The lower-bound is the lowermost elevation obtained from the maximum value of depth of action. As seen, the upper-bound values vary around mid-height of the model (0.5H) and stay constant for increasing acceleration levels. On the other hand, the lower-bound values range between 0.75H-0.90H showing a slight correlation with the acceleration level.

At higher acceleration levels the earth thrust may act at deeper elevations. End-of-shaking depths of action range between 0.6H to 0.7H showing no relation to the level of shaking. Values at the left face are consistently higher than the right face, possibly because the wall exhibits larger deformations along the left direction resulting in larger end-of shaking earth pressures.

The location of action of the total reinforcement force is shown in Figure 2-105 for various base acceleration levels. Similarly, three different graphs are presented including upper-bound and lower-bound values of location of action as well as the end-of-shaking locations. Similar results are observed for the location of action of the reinforcement force as the ones for earth pressure. As seen the upper-bound values are around mid-height of the model (0.55H) and stay constant for increasing acceleration levels. On the other hand the lower-bound values range between 0.7H-0.8H showing a slight relation with acceleration level. At higher acceleration levels the equivalent reinforcement force may act at slightly deeper elevations. End of shaking depths of action are around 0.6H for both walls.

The effect of design factor of safety is investigated by performing additional dynamic analyses by changing the amount of reinforcement in the model. The original model which represents the as-built conditions of the wall and is taken as a base case. The parameters that would affect the reinforcement strength are changed by some amount to change the overall factor of safety of the model. Model parameters such as reinforcement area, reinforcement perimeter, reinforcement interface stiffness are increased (or decreased) by the same ratio at all reinforcement levels. The same procedures described in the static analysis sections were followed to bring the revised model into static equilibrium. A series of dynamic analyses were performed with the same range of peak accelerations used in the analysis of the base case.

Four more cases were analyzed in addition to the base case. Properties were changed so that two cases of increased and two cases of decreased factors of safety were formed. Two cases of decreased factor of safety were formed such that the overall factors of safety were 10% and 20% reduced in comparison to the base case. Similarly, two cases of were formed where factor of safety was increased 20% and 40% in comparison to the base model.

Of particular interest was tracking how the average and peak deformations would vary with respect to different design conditions. Results are shown in Figure 2-106 where average deformation is plotted for five different design cases are presented for various acceleration levels. It is clearly seen that the increase in factor of safety significantly reduces average deformations. Similarly, peak deformation is plotted for the design cases in Figure 2-107. The same trend holds for peak deformations where the effect of design factor of safety are demonstrated.

Additionally the ratio of the average deformations at various design levels to those at the base case are shown in Figure 2-108. It is seen that 20% reduction in factor of safety results in about 60% larger average deformations in comparison to the base case. 20% larger average deformations are measured for the case with 10% less design value. 10% reduction in average deformation is obtained with 20% increase in factor of safety in comparison to the base case. The effect of factor of safety on the reduction of average deformations gets marginal with further increases in factor of safety.

Additionally, the ratio of the peak deformations at various design levels to those at the base case are shown in Figure 2-109. The effect of factor of safety is much more evident in terms of peak deformations. It is seen that 20% reduction in factor of safety results in about 140% larger peak deformations in comparison to the base case. Approximately 60% larger average deformations are measured for the case with 10% less design value. A 50% reduction in peak deformation is obtained with 20% increase in factor of safety in comparison to the base case. 80% reduction in peak deformation is obtained with 20% increase in factor of safety in comparison to the base case.

## 6. SUMMARY AND CONCLUSIONS

Following the August 1999 Kocaeli, Turkey Earthquake ($M_w$=7.4) investigations were performed in the affected area to document geotechnical field performance. The study focused on the performance of improved soil sites and mechanically-stabilized embankments (MSEs). Of particular significance was the performance of two Reinforced Earth (RE) walls located at the site of the Arifiye Bridge overpass. These walls, constructed of steel strips,

concrete facing elements, and compacted granular fill, performed well and suffered little damage despite being subjected to ground shaking , and large fault-rupture related ground displacements nearby. Numerical analyses were performed to investigate the factors contributing to this performance. Both the field documentation of the walls as well as the numerical analyses provided important insight into RE wall behavior under seismic loading.

The principal findings from the study are:

1) The RE wall system at the Arifiye Bridge Overpass is an important case history that highlights the seismic performance of reinforced earth walls. The walls, constructed of steel strips and compacted select backfill, performed well despite being shaken with ground accelerations >0.2g in an M7.4 event, and being subjected to fault-related ground displacements of 350 cm that occurred almost adjacent to the wall. The structure was designed for a seismic coefficient $k_h = 0.1$. The wall was subjected to acceleration levels at least twice the design value and still maintained its structural integrity. An unreinforced earthen embankment about 250 m from the wall suffered heavy damage, settling more than 1 m.

2) Following the earthquake, the maximum permanent lateral movement of the RE facing panels was about 10-15 cm, and this occurred at about one-third the wall height above the base. The settlement along the centerline of the double-wall system was estimated at 25-30 cm, primarily due to the lateral bulging of the system.

3) The fault rupture passed through the northern abutment and the adjacent pier causing lateral offset more than 3 meters. The bridge decks collapsed due to relative movement of the piers and the bridge abutments at both sides. Bridge deck spans were simply supported.

4) Higher sections of the MSE structure settled, punching into the foundation soils. This resulted in the misalignment of several facing panels. Relative displacement of the facing panels caused them to separate and this resulted in the spillage of some backfill material.

5) The structure has undergone permanent deformations as a result of shaking. Permanent deformations may be more important in terms of serviceability of such structures. This case demonstrates that significant permanent deformations can develop before the collapse of the earth structure. However, there are no current conventional design methods to estimate the permanent deformations of reinforced soil structures. Prediction of permanent deformations should be a part of the seismic design of reinforced soil structures.

6) The reinforced concrete bridge abutment on piles did not suffer any damages despite the ground failure in the vicinity. The abutment did not settle, in contrast to the MSE wall it supported.

7) It was observed that the slip joints helped the wall to sustain these foundation deformations without being overstressed.

8) This case demonstrates well-designed conventionally-constructed RE walls (steel strips and compacted select fill) and with good foundations tend to perform well under strong ground shaking.

9) Analyses were performed for the as-built conditions of the wall. These results were compared with the model with different factors of safety. Reinforcement amount was increased or decreased some percentage of the as-built conditions. This is an indirect measure of the overall factor of safety of the model. Analyses were performed on these models with different reinforcement. These made possible to estimate the effect of the reinforcements used on wall performance. It was seen that the walls built with increased amounts of reinforcements performed better compared to the base case. Smaller deformations developed as the factor of safety increased.

10) The earthquake-induced RE wall deformation pattern and displacement magnitudes were successfully predicted using the computer code FLAC assuming two-dimensional, plane-strain conditions. The predicted deformation pattern was consisted of (1) significant settlement along the double-wall centerline and (2) lateral bulging with peak displacements occurring at about one-third the wall height above the base. This predicted deformation was consistent with the observations. In

terms of the displacement magnitudes, a maximum lateral wall displacement of 12-14 cm was predicted, compared to an observed value of 10-15 cm. The predicted settlement along the centerline of the double-wall system was 27 cm, consistent with the observed value of 25-30 cm. The static analysis was conducted using a Mohr-Coulomb soil model and hyperbolic soil stiffness criteria, and the dynamic analysis assumed an elasto-plastic model that assumed linear behavior up to the yield stress, and plastic behavior beyond this value.

11) Pre-earthquake stress conditions determined during a static analysis that simulated wall construction were important in terms of correctly estimating the final earthquake-induced stresses and forces in the RE system.

12) Permanent vertical and lateral displacements probably developed during the strong part of shaking (first 10 seconds), as indicated by predicted displacement time histories calculated for different locations and elevations along the walls.

13) The numerical analyses indicate that the earthquake shaking significantly increased the forces in the steel reinforcement strips, especially in the lower third of the walls. Maximum reinforcement forces reached values about two to three times those at the end of construction at the upper and lower elevations respectively. Even though these numbers indicate that the some of the steel strips reached their yield strength and some slip probably took place, the system integrity was maintained by a large margin.

14) It is interesting how the wall performed well with limited earthquake induced deformations even though the analyses show that reinforcement forces were larger than expected. The main reason these walls have not collapsed is their tolerance to deformations. Steel is a ductile material and it is believed to be the major contributor to the flexible behavior of reinforced soil structures. Strong ground shaking induces significant loads to the reinforced soil structure, but the reinforced soil structure can tolerate large deformations. Rather than withstanding against the effects of shaking like a rigid structure it deforms flexibly. If some yielding took place at some reinforcement levels, it is believed to have been only temporarily. Results of the analyses show that even if some yielding and/or slip took place the deformations were not uncontrolled. The flexible nature of the structure may have

been a factor in the redistribution of stresses from the yielded reinforcement levels to the other levels which can sustain more load.

15) Displacement is likely to be the controlling criterion for the seismic performance of RE walls, as opposed to shear failure or collapse. From a seismic standpoint, RE walls behave as flexible systems. In the numerical analyses, no slip surface or failure wedge developed in the backfill, although enough settlement and horizontal displacement occurred to present potential serviceability problems for the walls. Steel reinforcements have probably caused the deformations in the backfill to spread out rather than concentrating along a well-defined slip surface. Similar observations were made by Shewbridge and Sitar (1996) on tests performed on models of reinforced sand.

16) The predicted settlement presented a potential problem for the overlying roadway. Similarly, the analyses predicted that it is likely that enough out-of plane movement of the facing panels to allow backfill spillage would occur before a pronounced slip surface can develop.

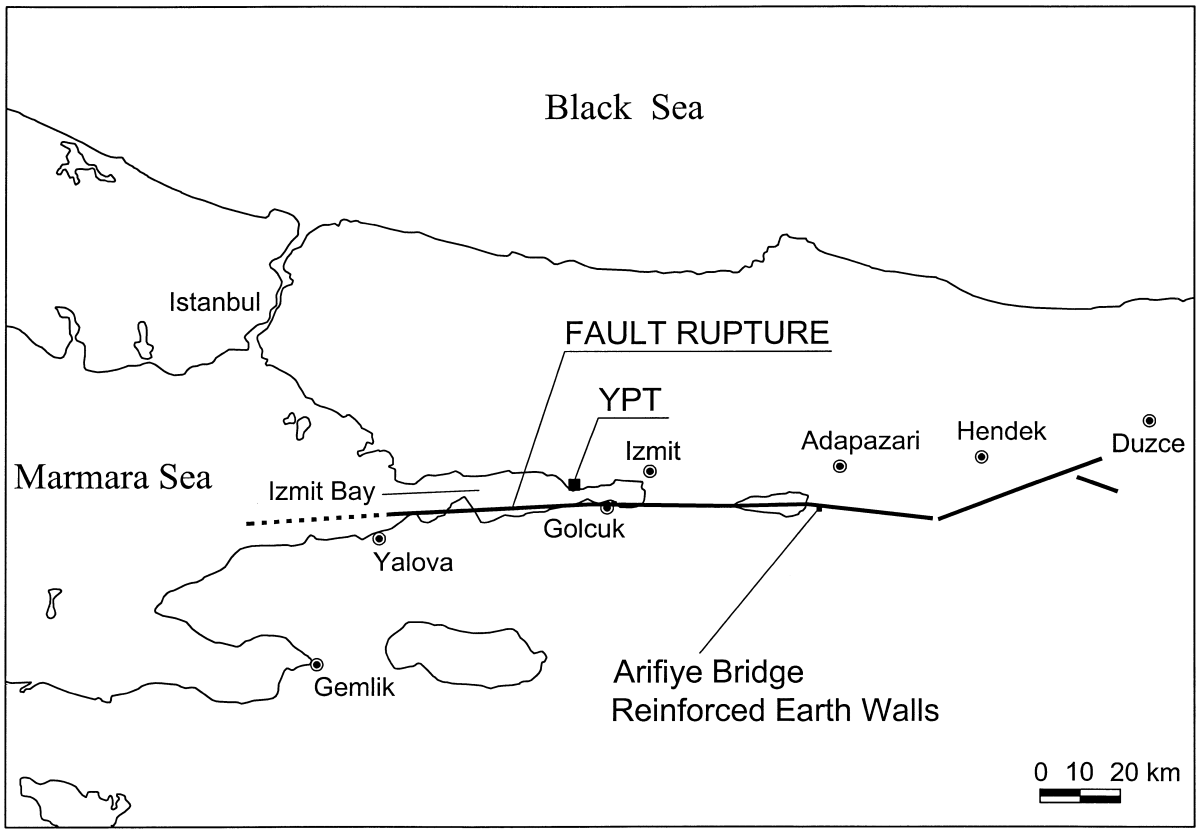


Figure 2-1. Setting of the August 17, 1999 Kocaeli Earthquake

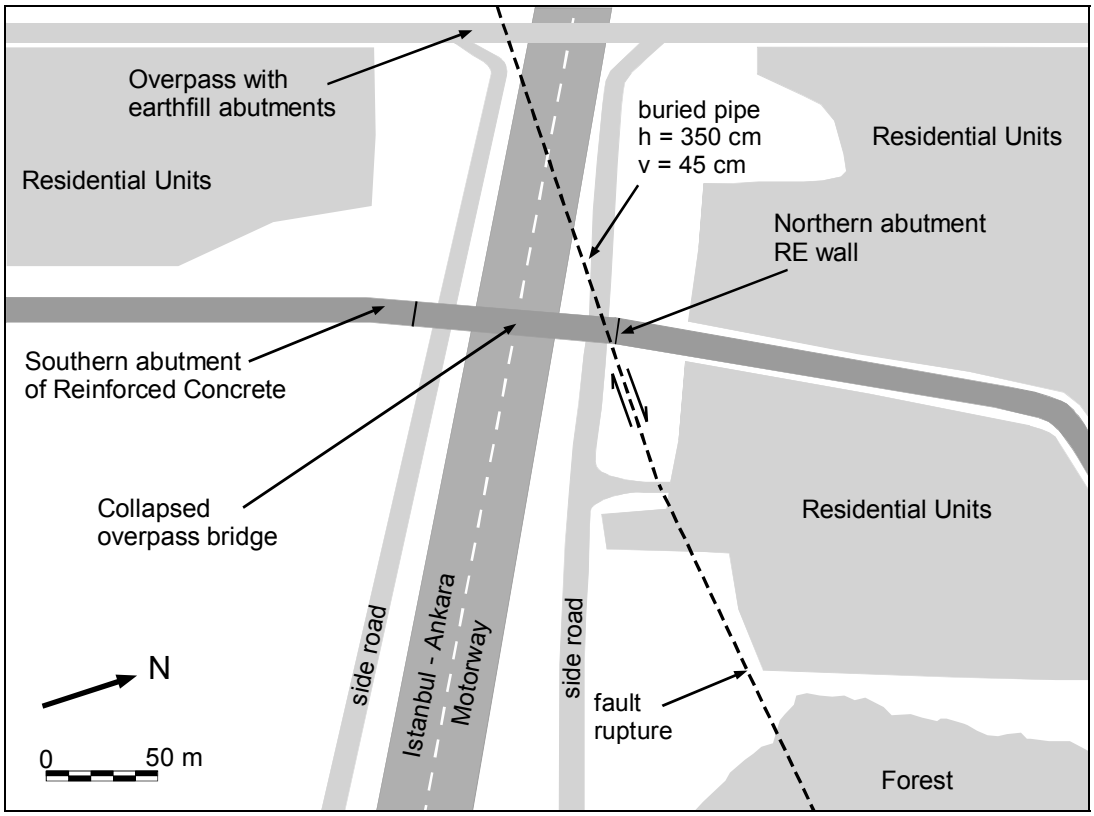


Figure 2-2. Plan view of Arifiye Overpass and the fault rupture trace

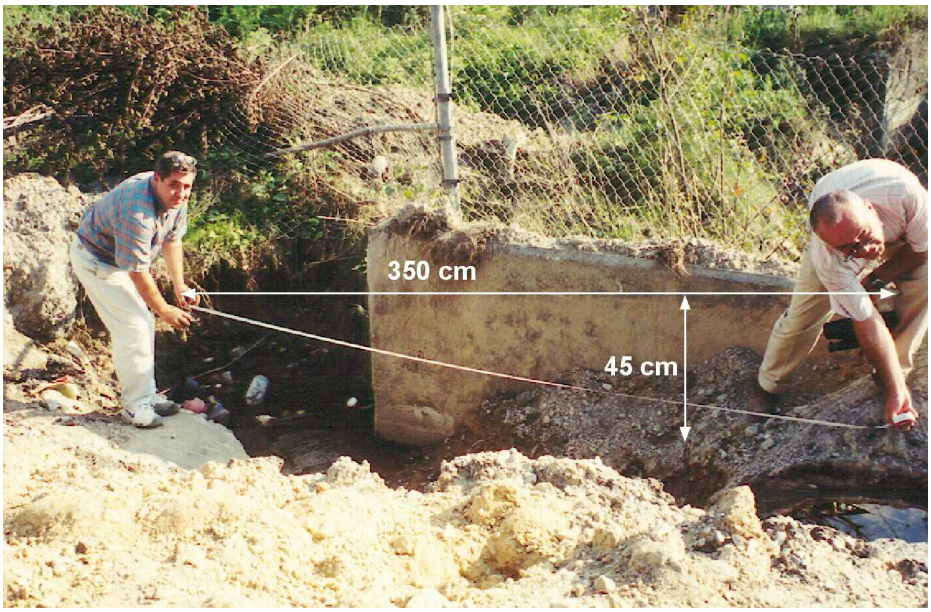


Figure 2-3. Measurement of the displacement of a pipe ruptured by fault movement

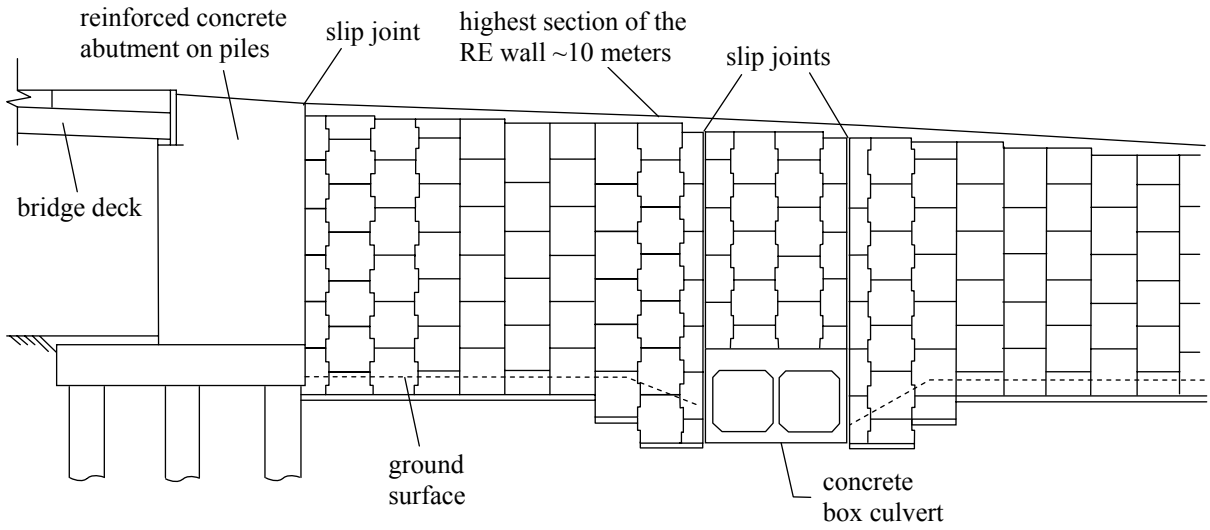


Figure 2-4. Side view of the Arifiye Overpass MSE wing walls

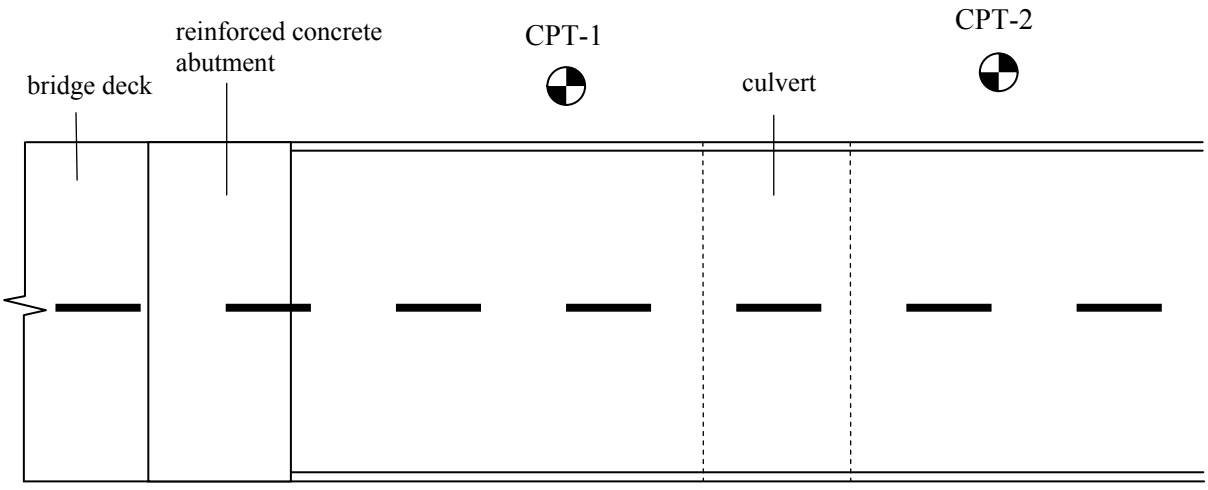


Figure 2-5. Plan view of the Arifiye Overpass and Cone Penetration Test locations

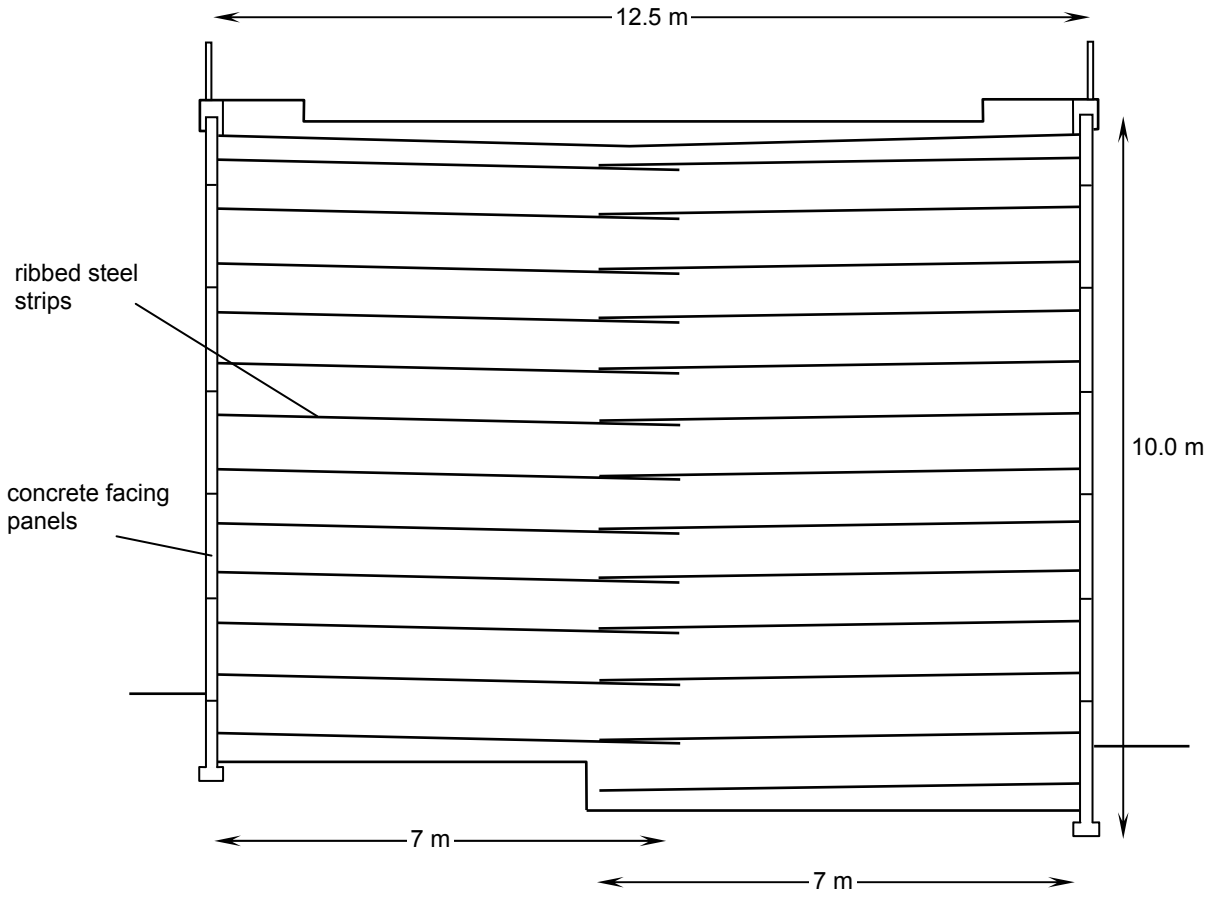


Figure 2-6. Cross section of the Arifiye Reinforced Earth Walls


Figure 2-7. Collapsed bridge decks

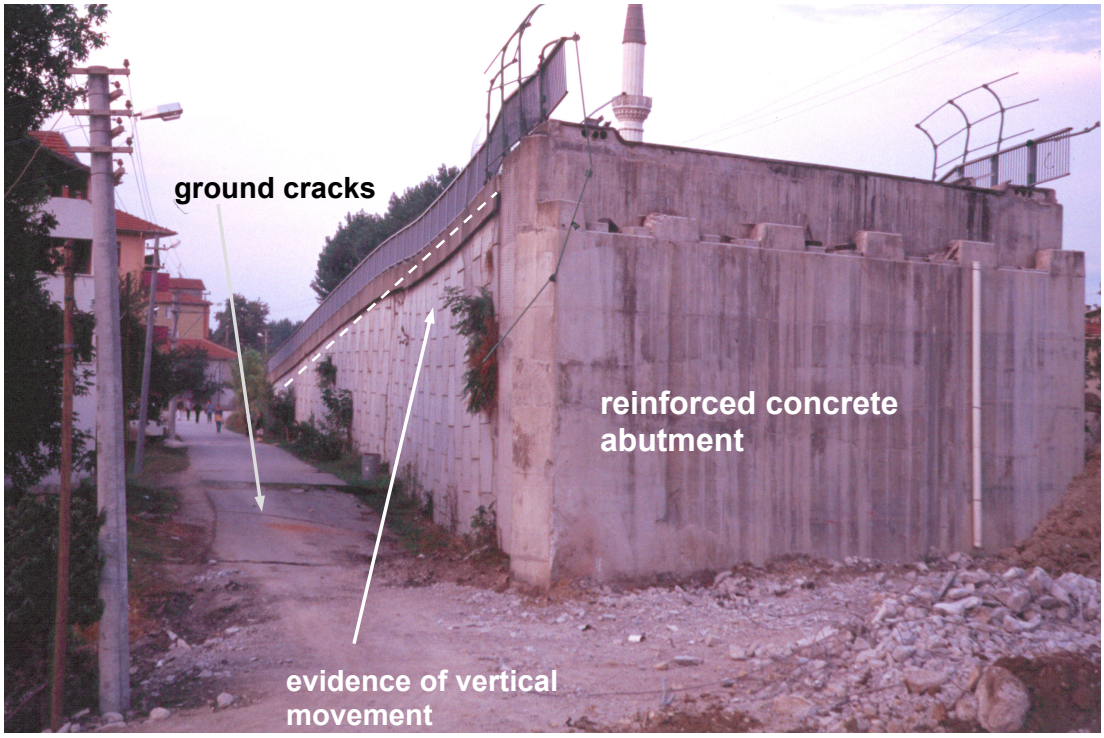


Figure 2-8. Approach embankment and signs of damage

Figure 2-9. Settlements and ground cracks near the buried culvert


Figure 2-10. Distorted facing panels near the culvert

Figure 2-11. Separation of the facing panels due to vertical distortion and spilled backfill material

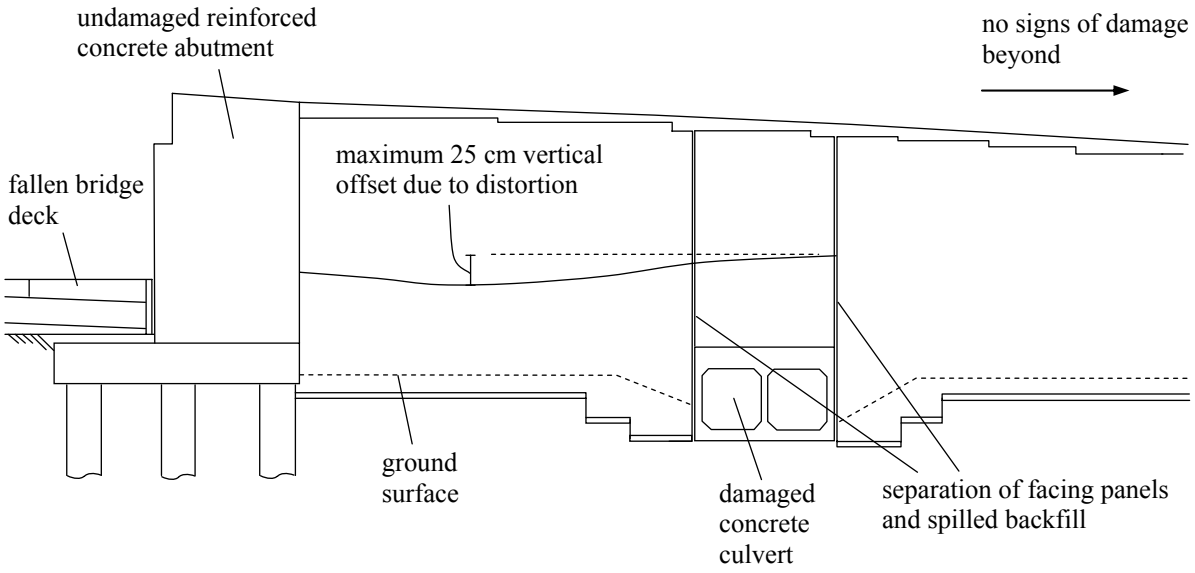


Figure 2-12. Schematic of damage – side view

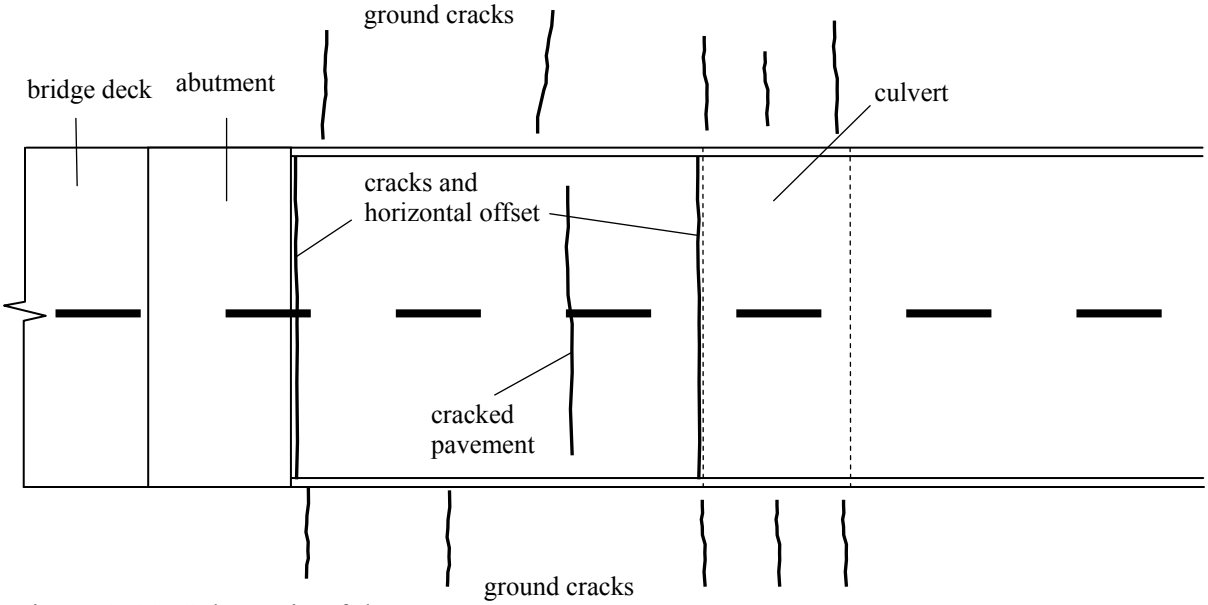


Figure 2-13. Schematic of damage – plan view

Figure 2-14. Damage at the top of the approach embankment. Sagging due to foundation settlement and cracks in the pavement are evident.

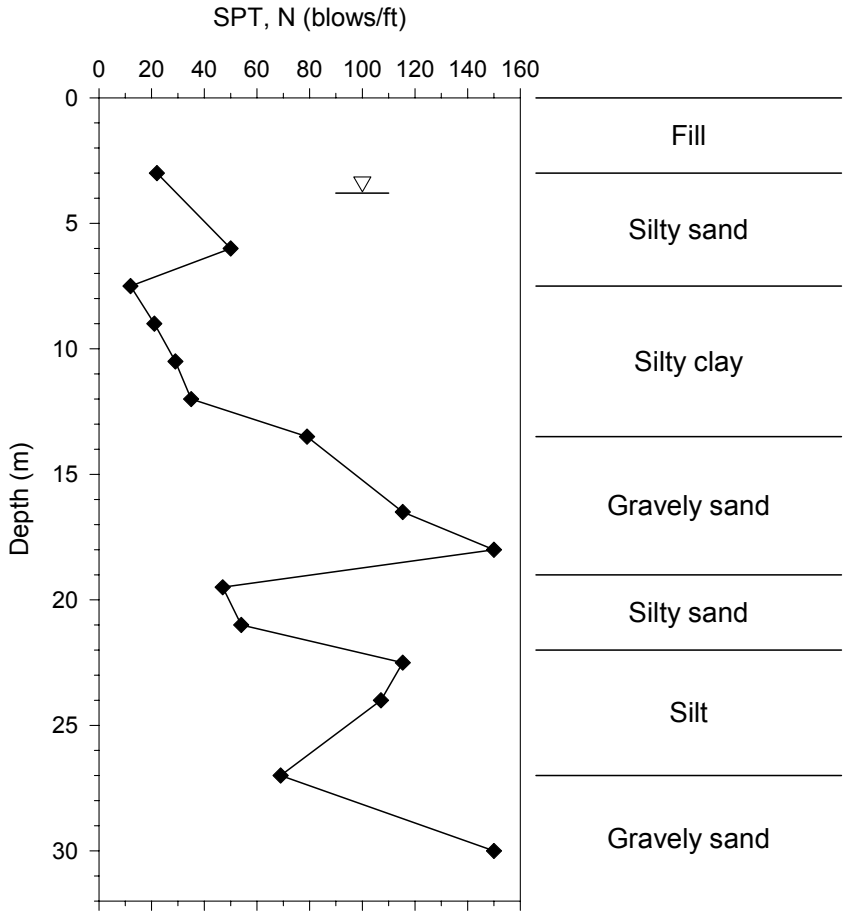


Figure 2-15. Subsoil profile and standard penetration test (SPT) results – obtained from the Turkish State Highway Directorate drilling crew operating at the time of the site visit

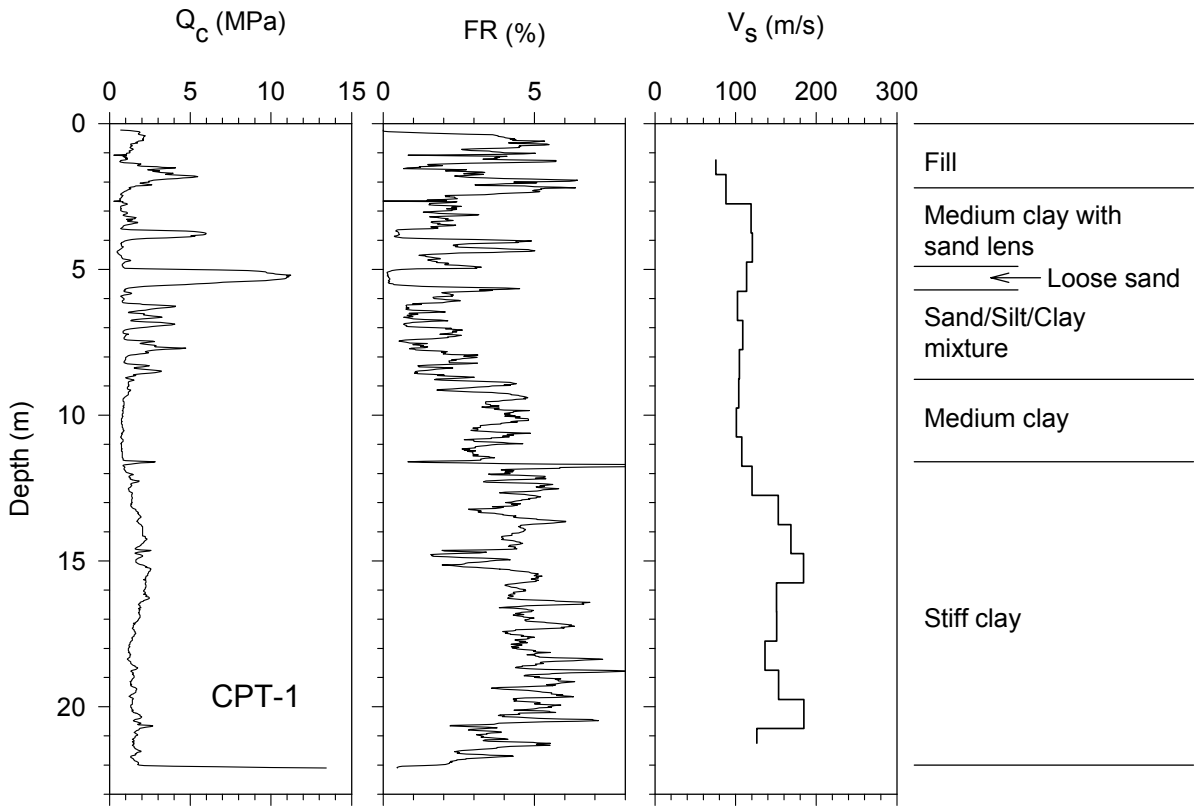


Figure 2-16. CPT sounding near between the culvert and the reinforced concrete abutment (CPT-1)

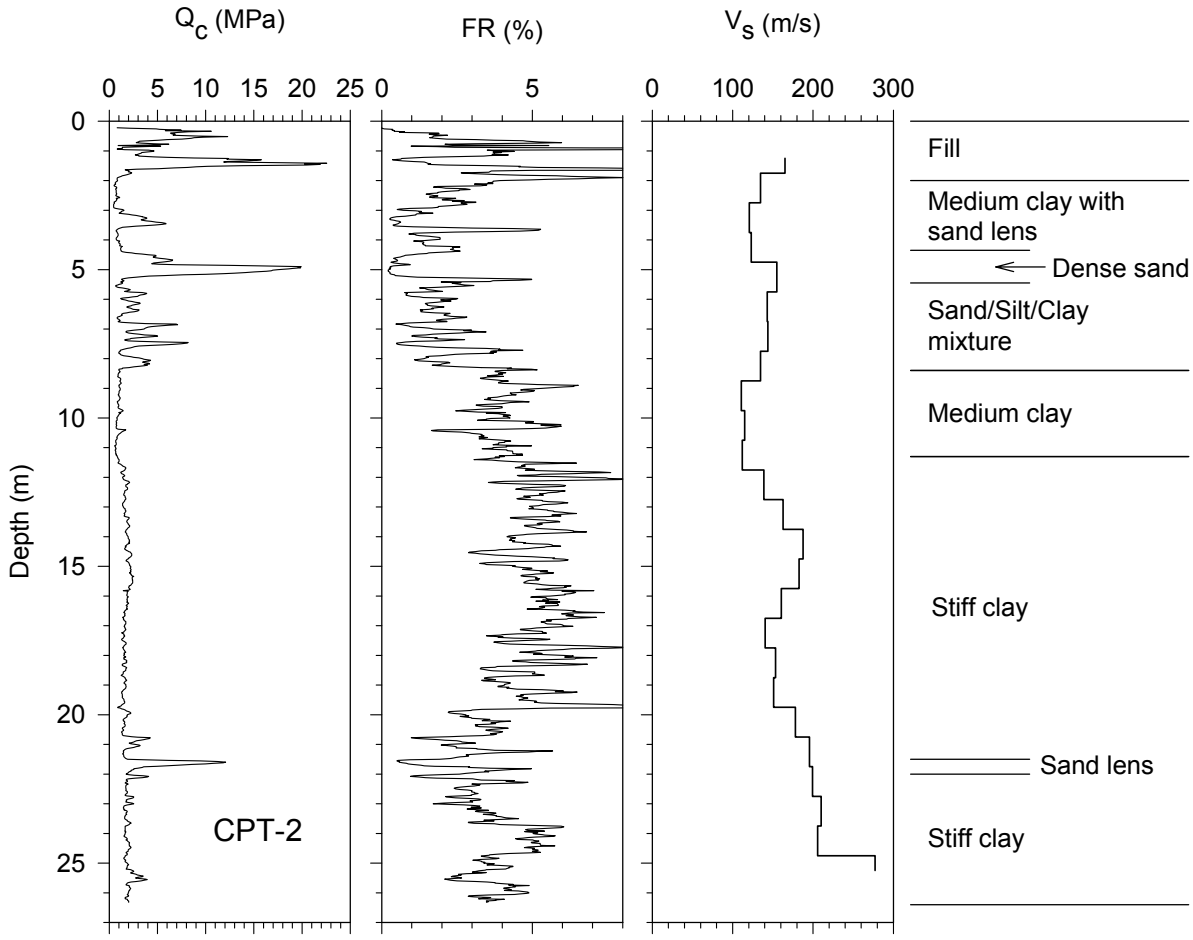


Figure 2-17. CPT sounding near the wall where no ground damage occurred (CPT-2)

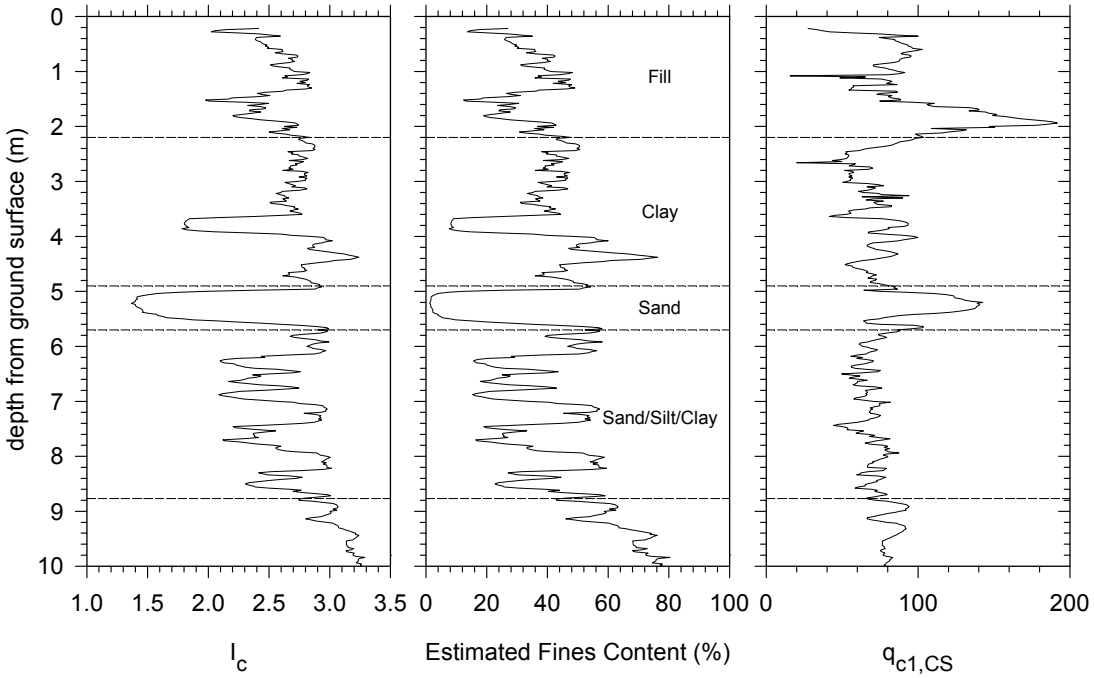


Figure 2-18. Estimated soil characteristics – CPT-1

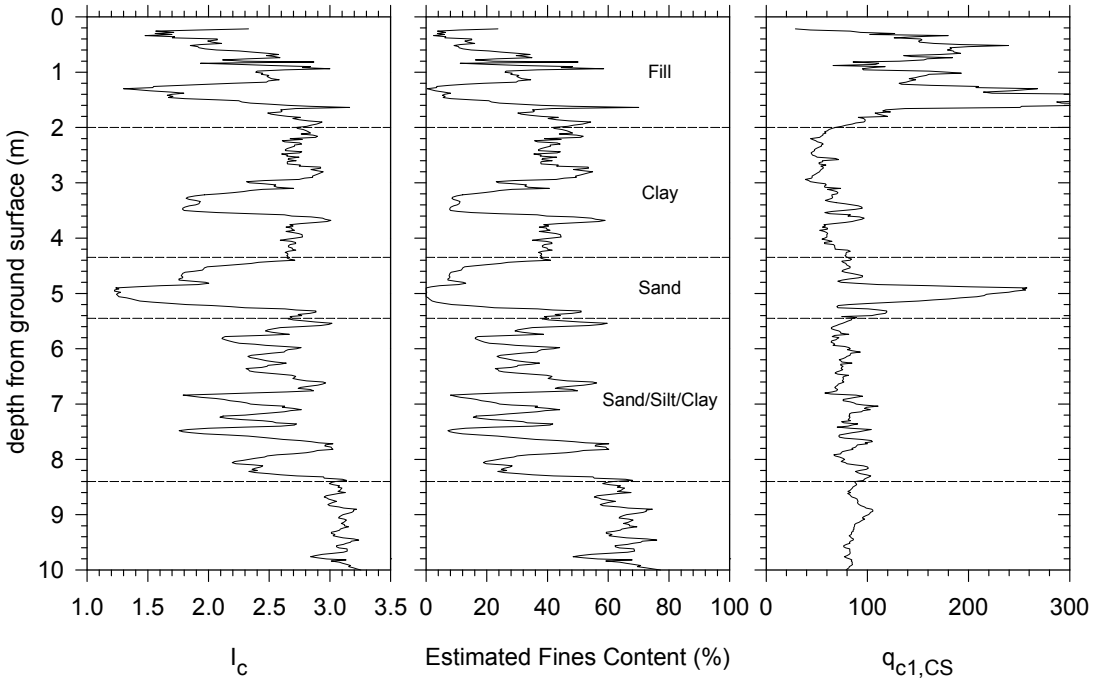


Figure 2-19. Estimated soil characteristics – CPT-2

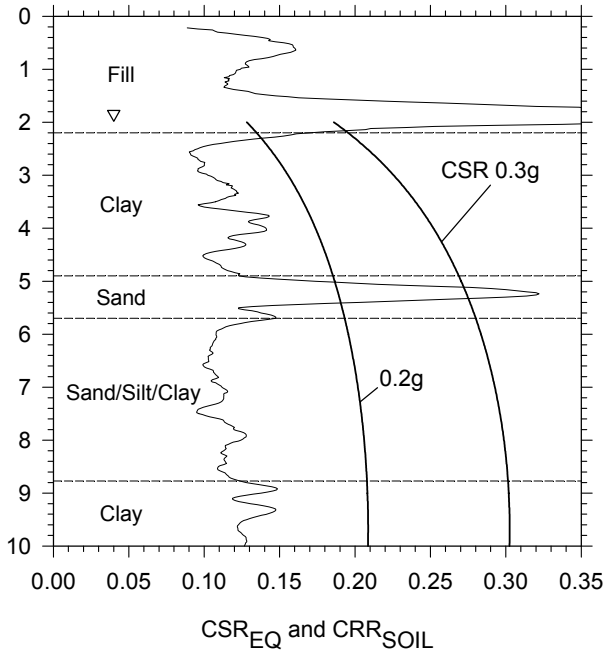


Figure 2-20. Comparison of induced cyclic stress ratio ($CSR_{EQ}$) and estimated cyclic soil strength (CRR) – CPT-1

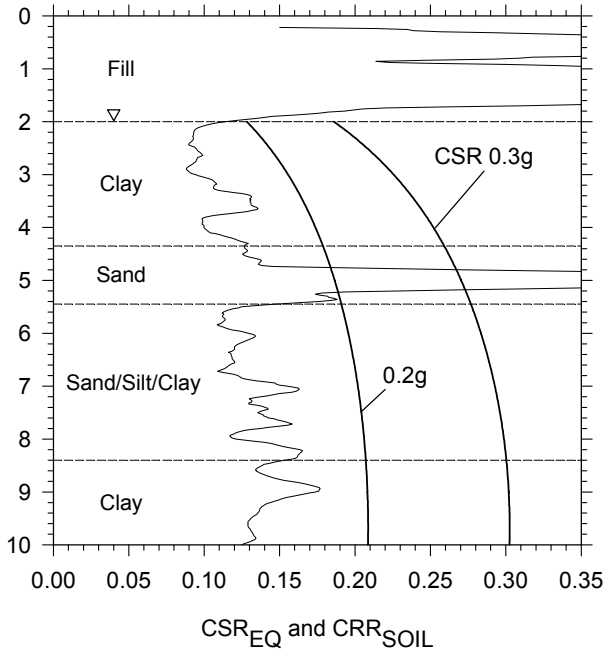


Figure 2-21. Comparison of induced cyclic stress ratio ($CSR_{EQ}$) and estimated cyclic soil strength (CRR) – CPT-2

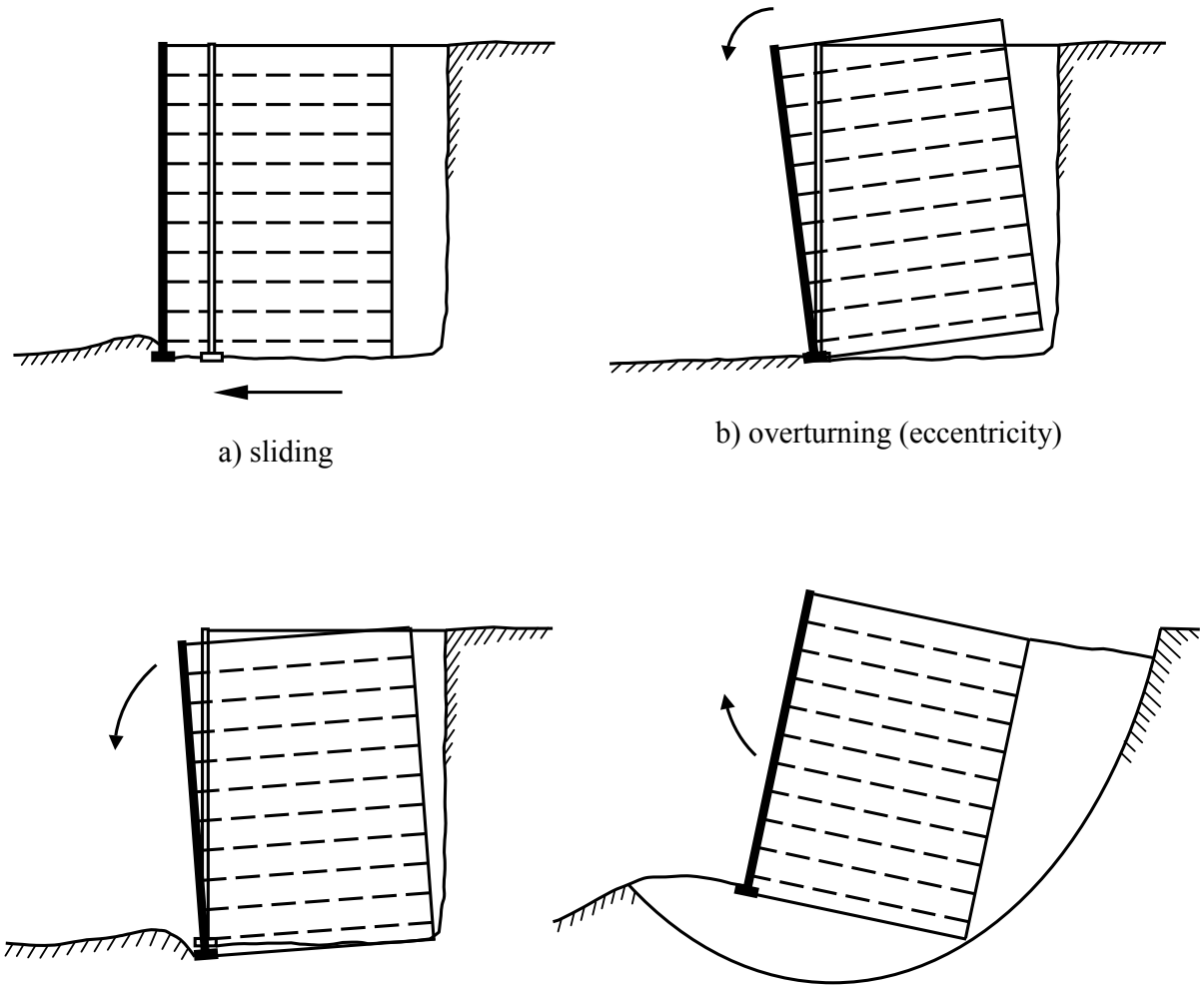


Figure 2-22. Potential external failure mechanisms of mechanically stabilized earth walls

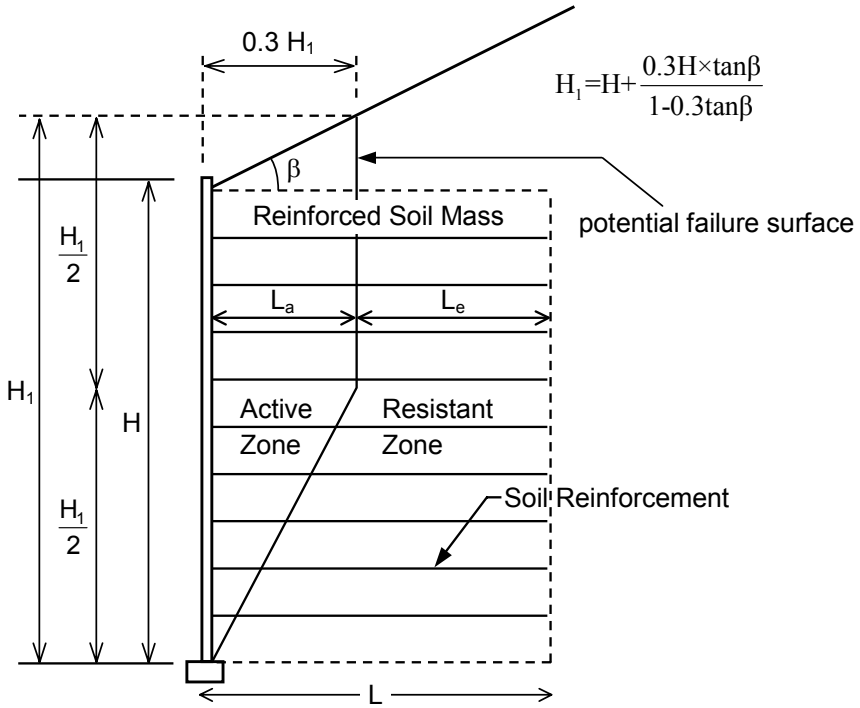


a) Inextensible Reinforcements

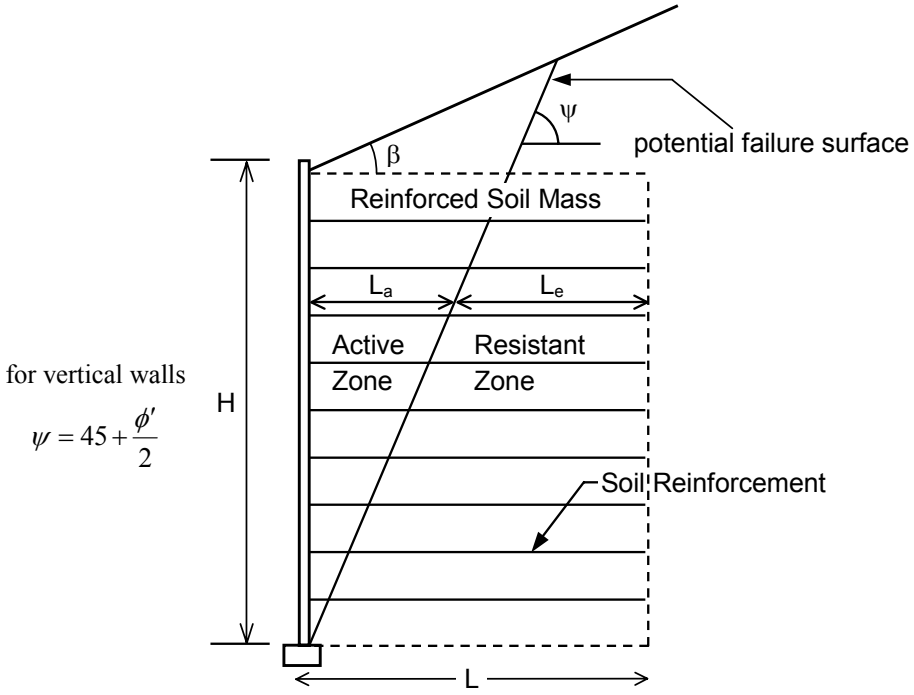


b) Extensible Reinforcements

Figure 2-23. Location of potential failure surface for use in internal design of MSE walls

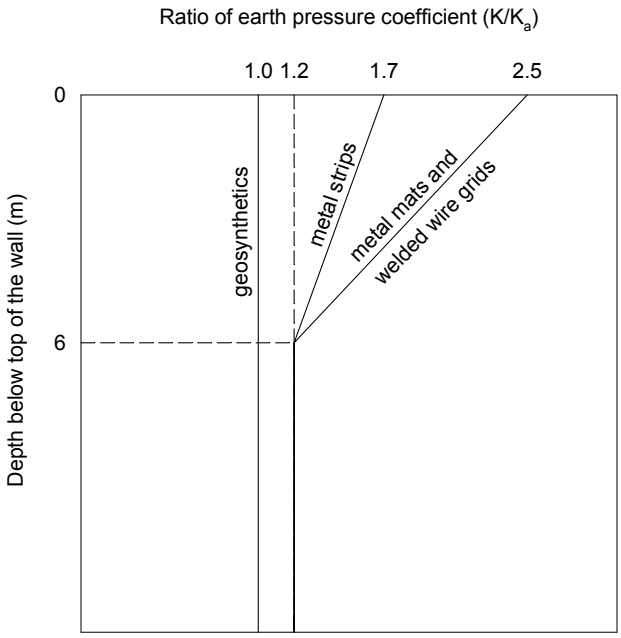


Figure 2-24. Earth pressure coefficient for mechanically stabilized earth walls recommended for design (Elias and Christopher 1999)

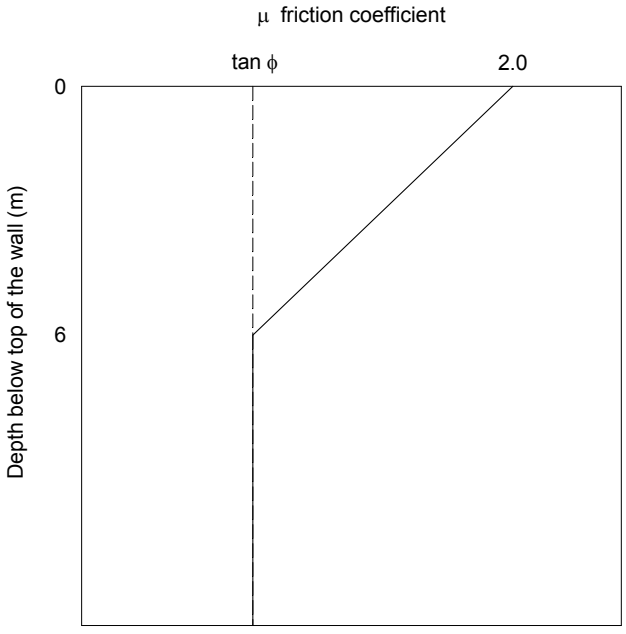


Figure 2-25. Friction coefficient recommended for ribbed steel strips (Elias and Christopher 1999)

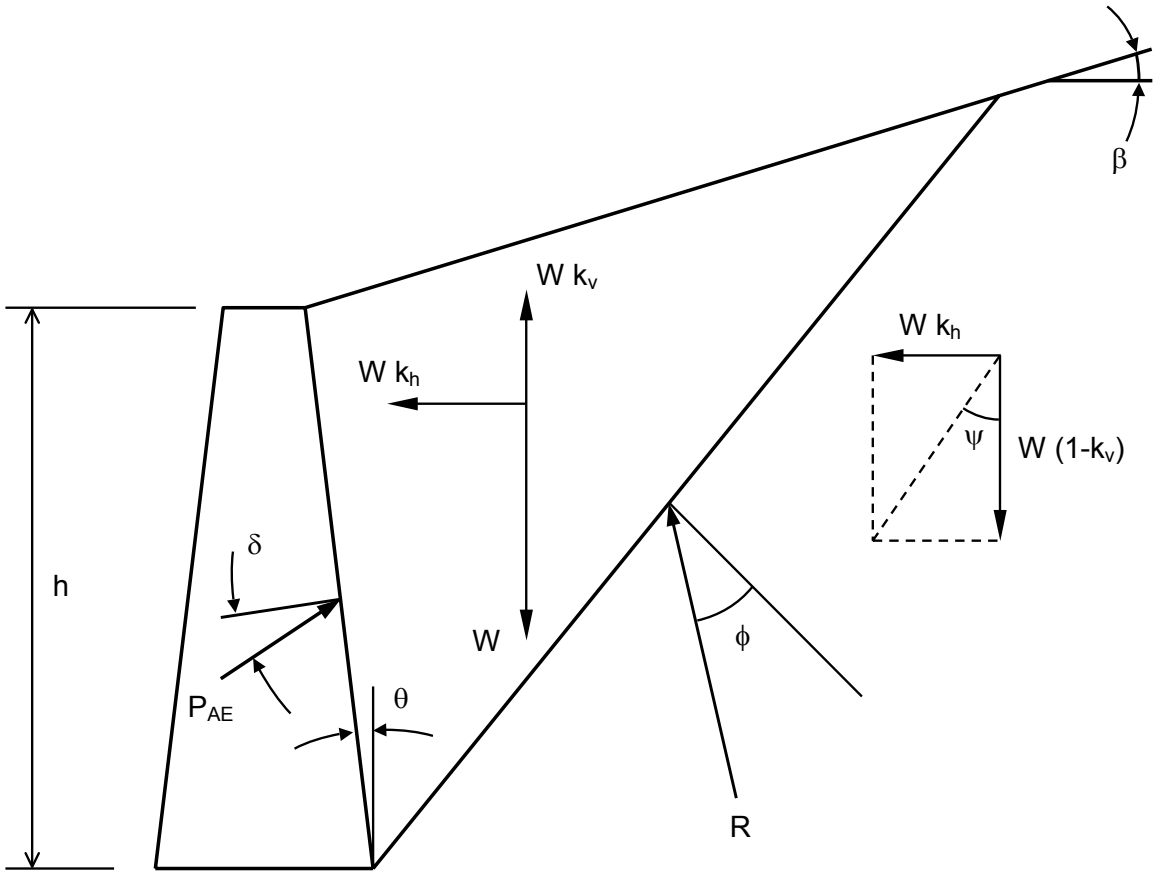


Figure 2-26. Mononobe-Okabe approach – forces acting on the retained soil mass

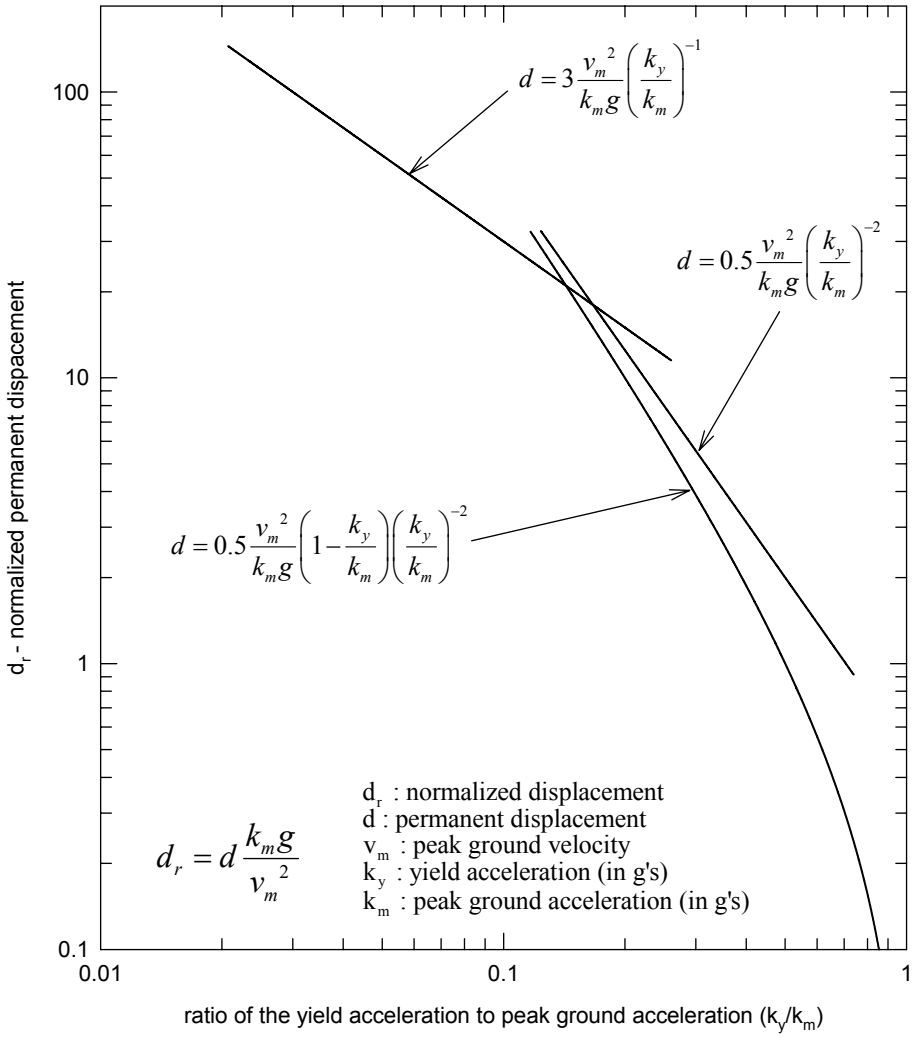


Figure 2-27. Non-dimensional displacement in relation to acceleration ratio as proposed by Newmark as upper bound envelopes (1965)

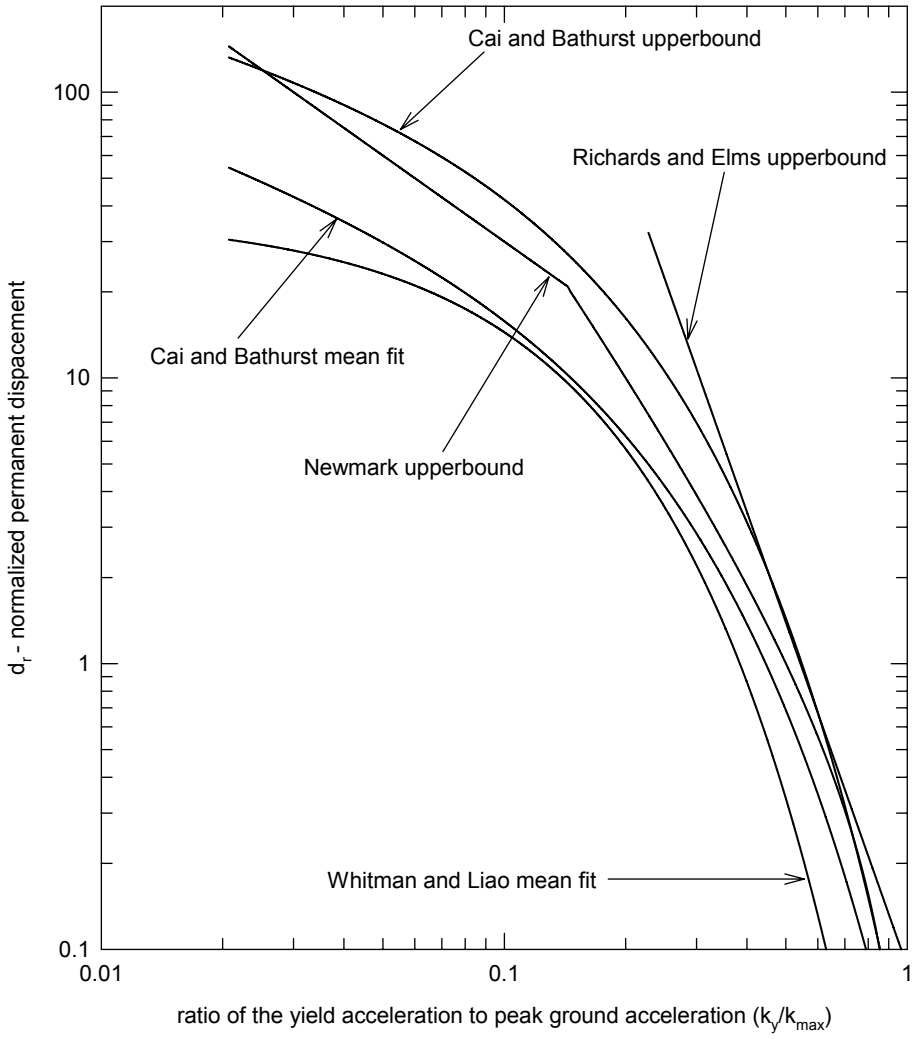


Figure 2-28. Non-dimensional displacement in relation to acceleration ratio as proposed by Newmark as upper bound envelopes (Newmark 1965)

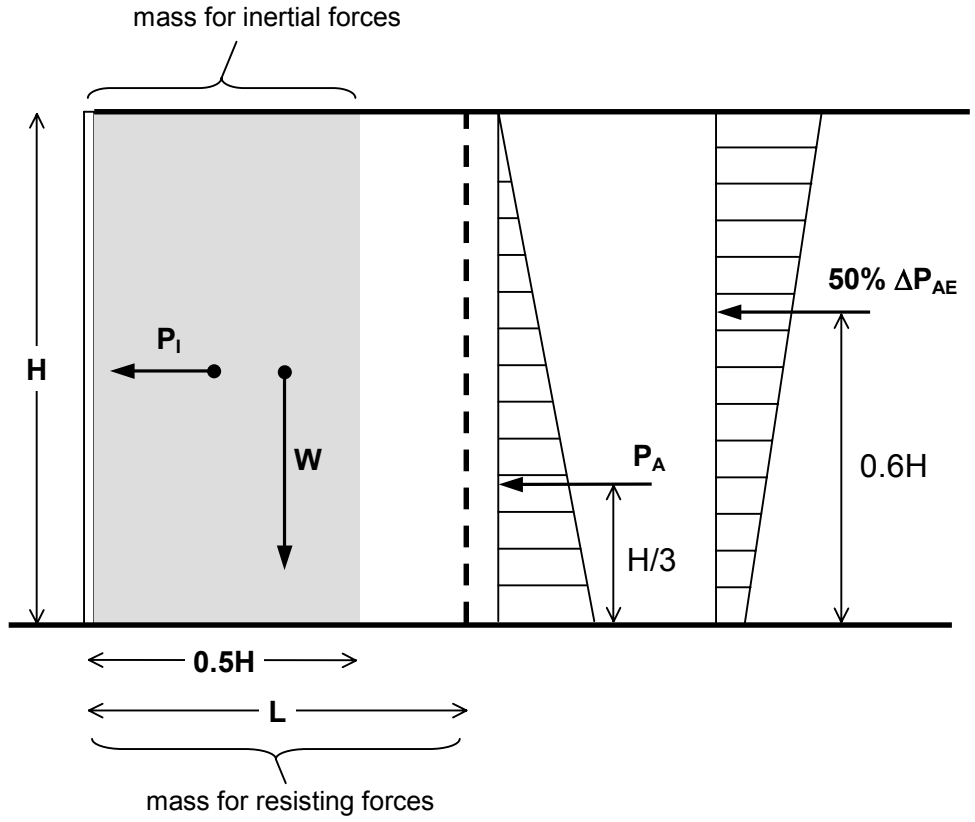


Figure 2-29. Mechanically stabilized earth wall with a vertical face. Idealized force system acting on the retained soil wedge in active mode of failure under dynamic loading

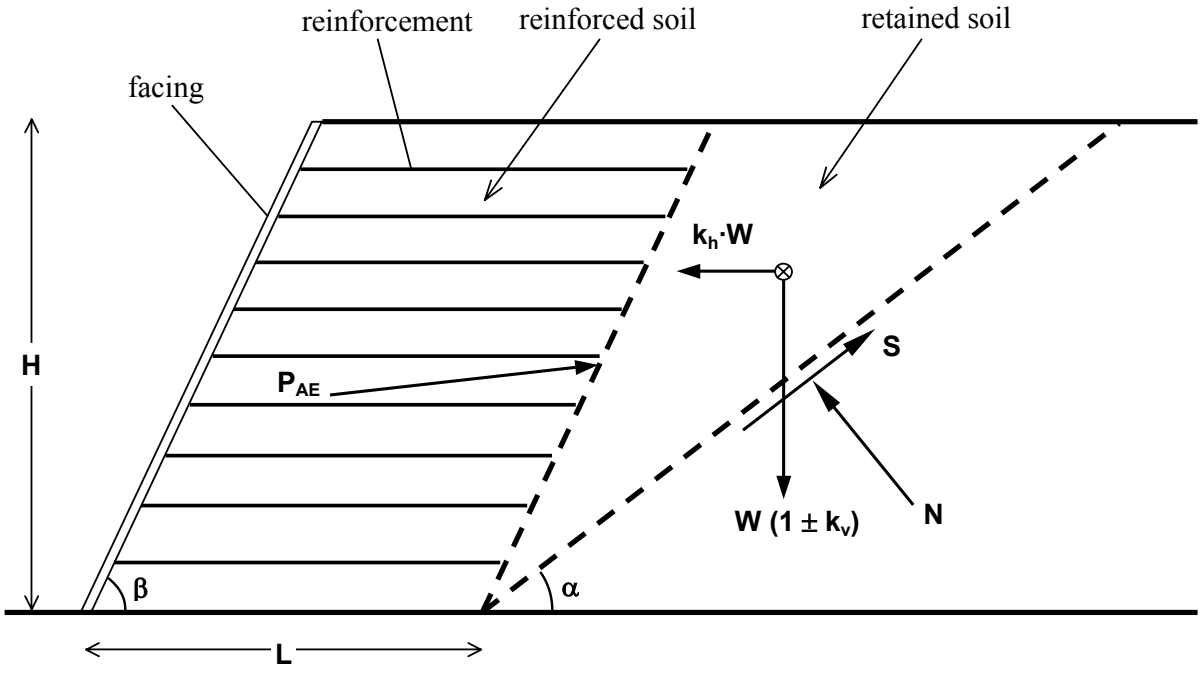


Figure 2-30. Mechanically stabilized earth wall with a sloping face. Idealized force system acting on the retained soil wedge in active mode of failure under dynamic loading

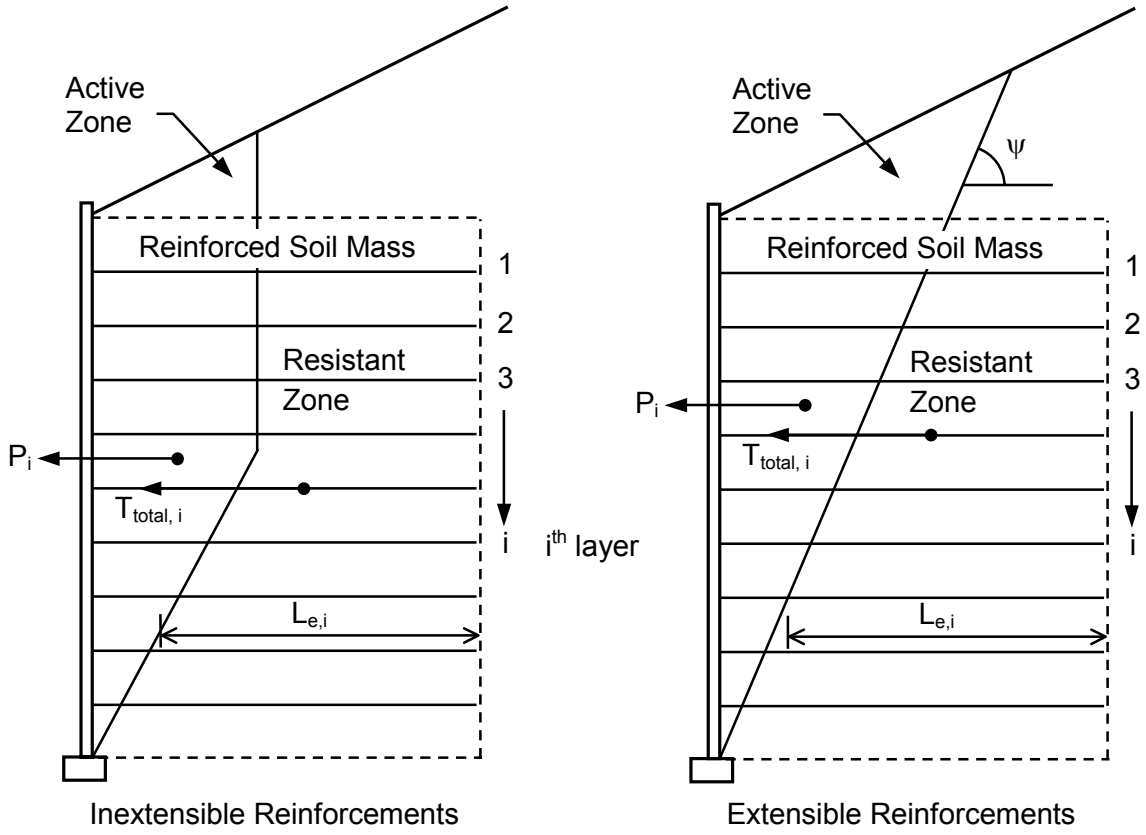


P : Internal inertial force due to the weight of the backfill within the active zone

$L_e$ : Length of the reinforcement in the resistant zone

$T_{max}$ : The load per unit wall width applied to each reinforcement due to static forces

$T_{md}$ : The load per unit wall width applied to each reinforcement due to dynamic forces

$T_{total}$ : Total force applied to each reinforcement per unit wall width

Figure 2-31. Geometry and forces involved in the internal design of MSE walls

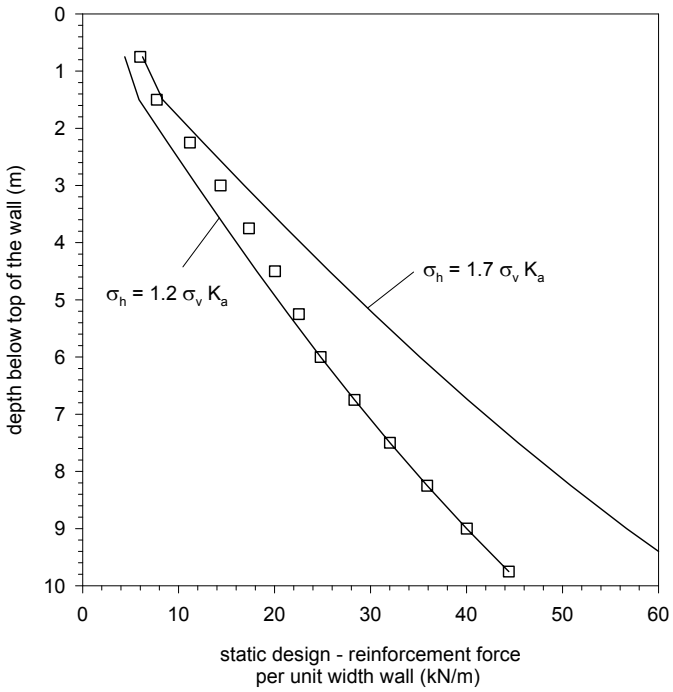


Figure 2-32. Reinforcement forces for static design per unit wall width (1m)

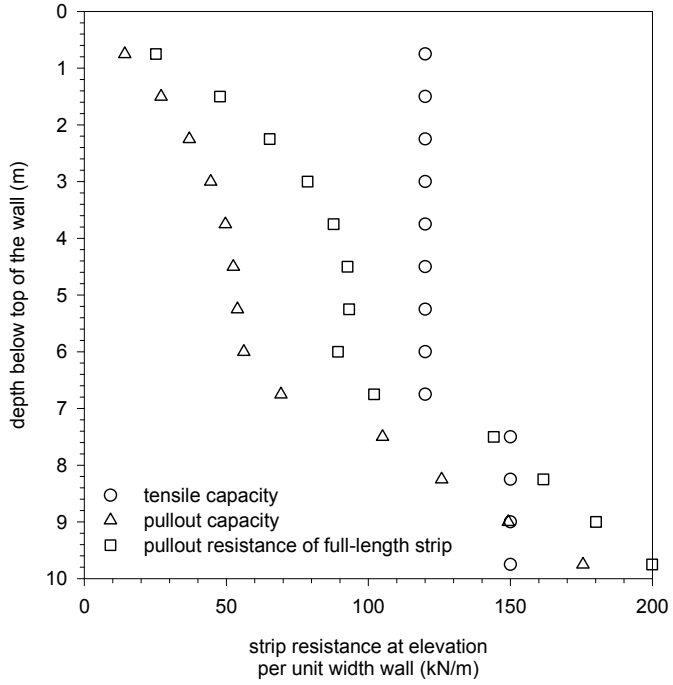


Figure 2-33. Tensile and pullout resistance of reinforcing strips to be used in design

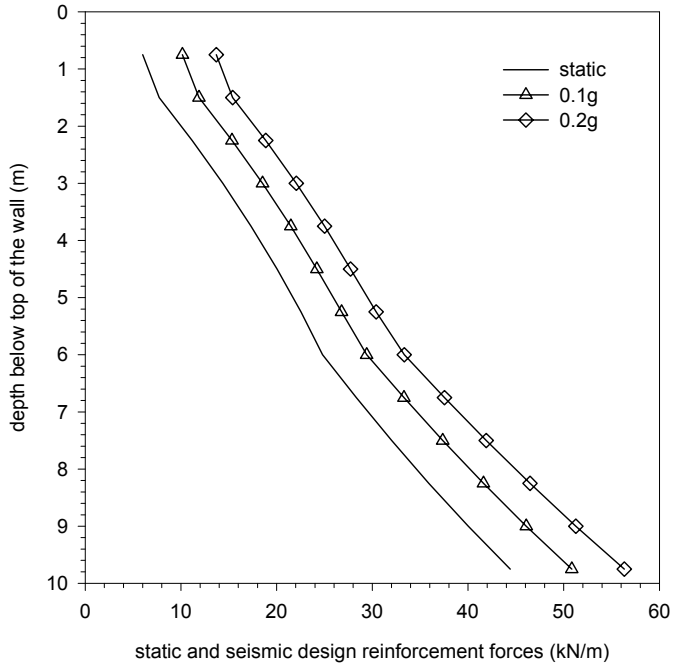


Figure 2-34. Maximum reinforcement forces for static and seismic design

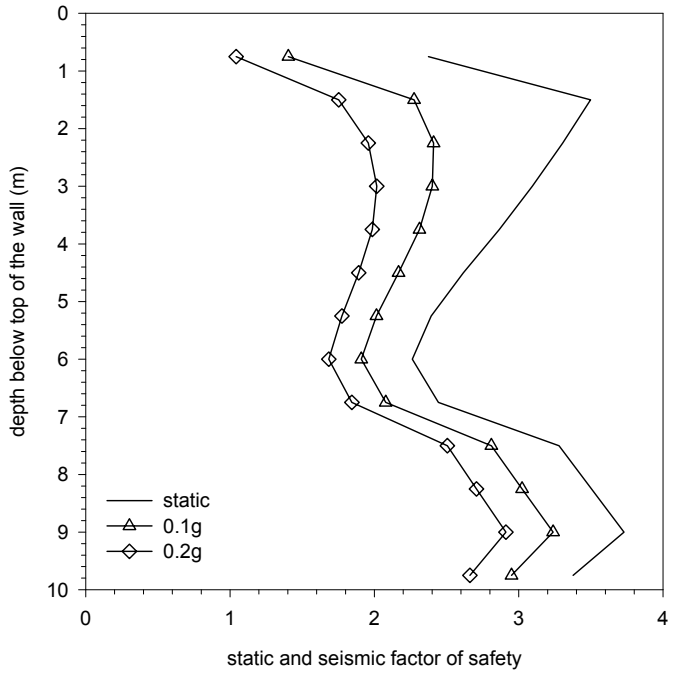


Figure 2-35. Static and seismic design – factor of safety

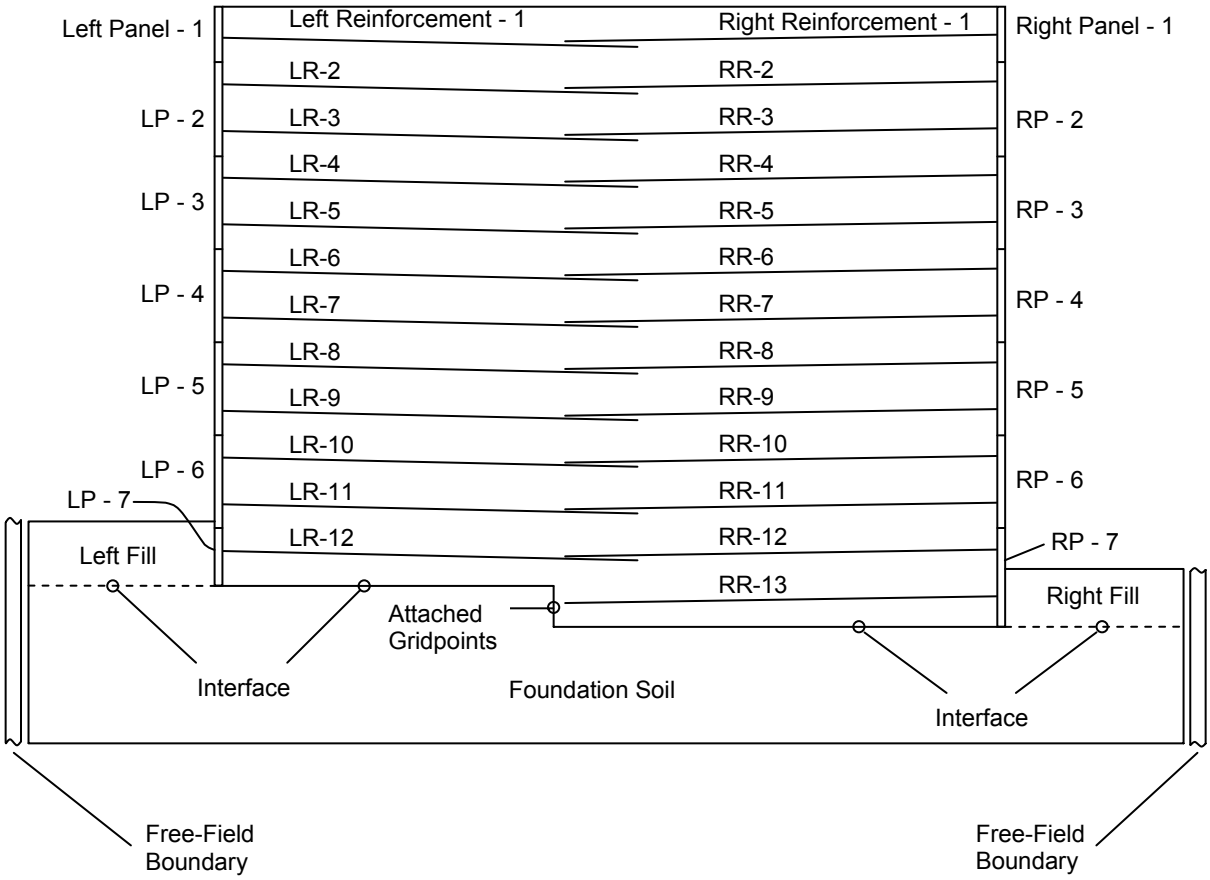


Figure 2-36. Components of the numerical model analyzed with FLAC

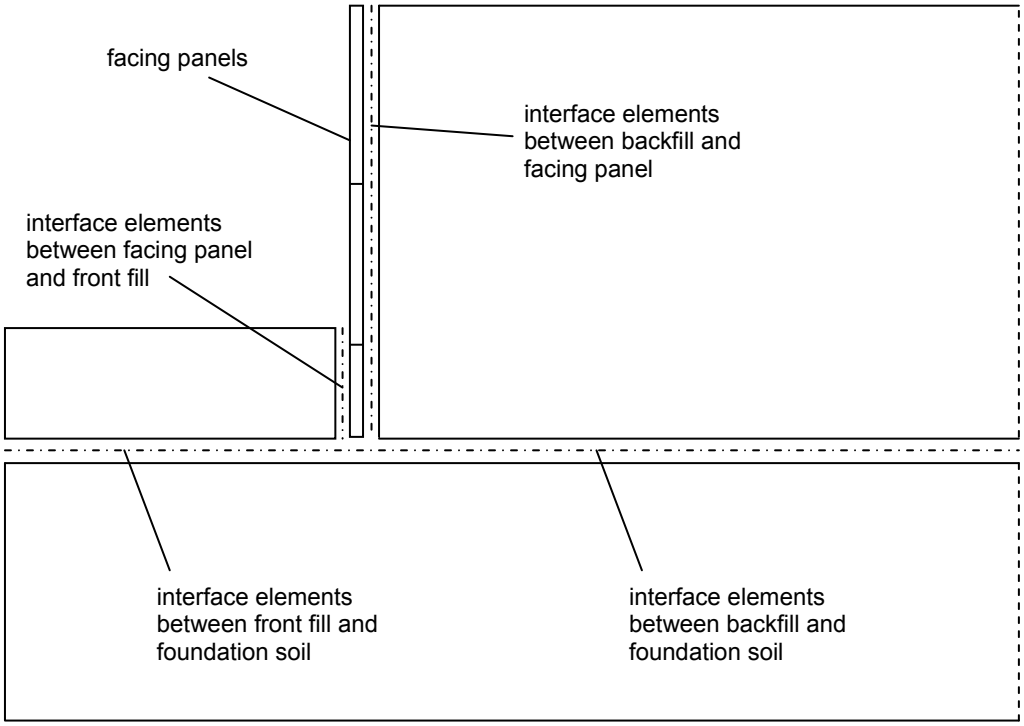


Figure 2-37. Connectivity of the backfill, foundation soil, front fill and the facing panel

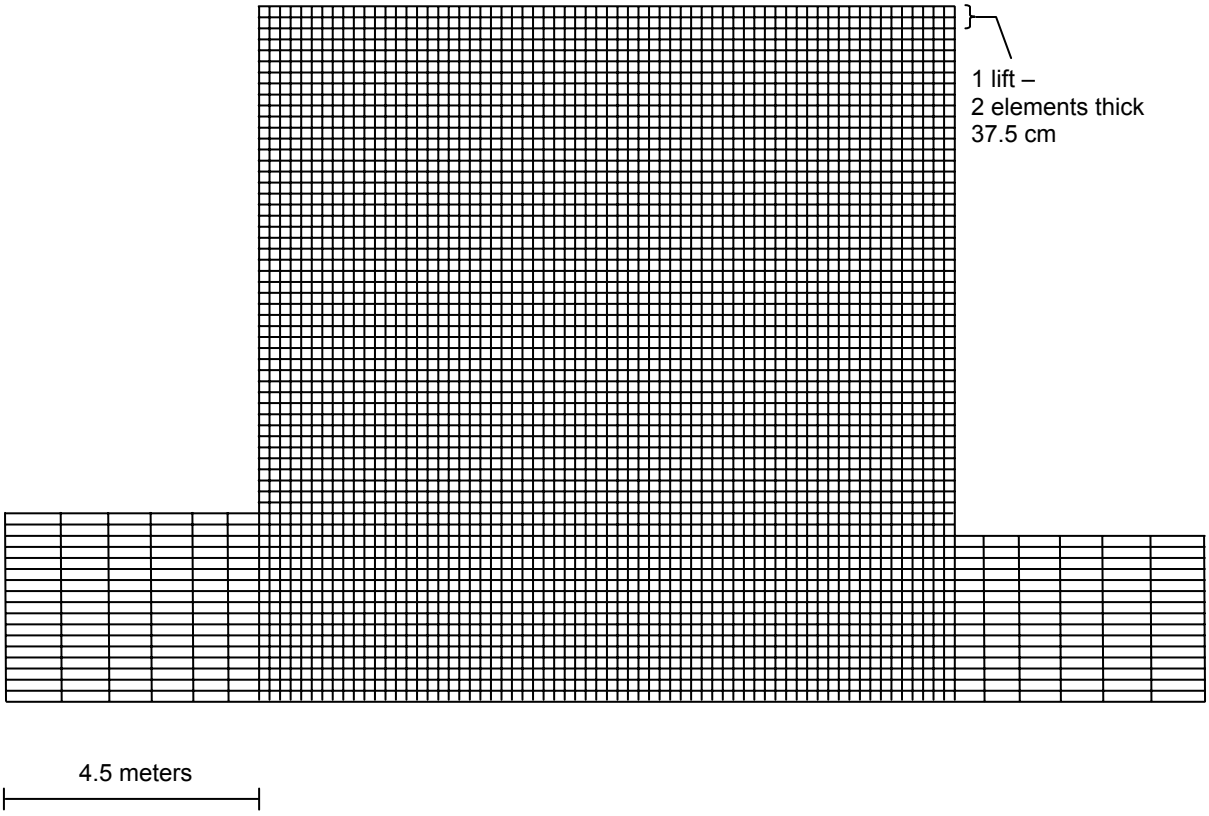


Figure 2-38. Finite difference grid used in the static and dynamic analyses.

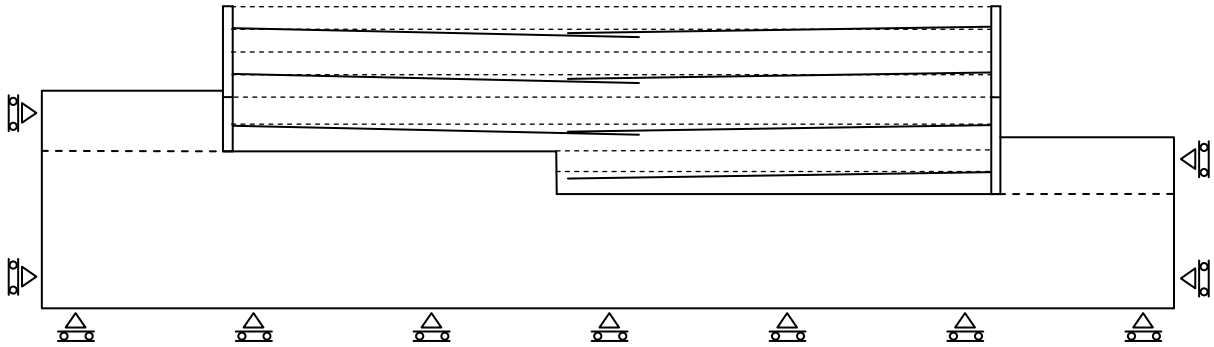

Figure 2-39. 8 lifts, 4 levels of reinforcement and 2 panels in place, panel connections hinged, model in equilibrium. Current model stresses used to update the stiffness and strength values of the earth material in the model.

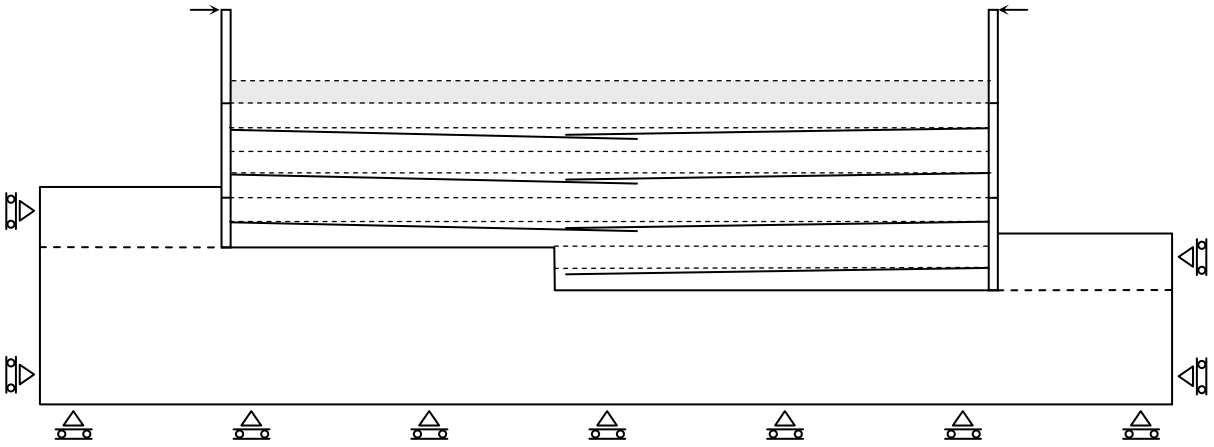

Figure 2-40. Third level of facing panels placed, connection of the third level of panels with the second level of panels is moment carrying. Top node of the new facing panels fixed for horizontal displacements. The new fill placed and the system brought to equilibrium under the weight of this new soil mass. Strength and stiffness updated under new stress conditions.

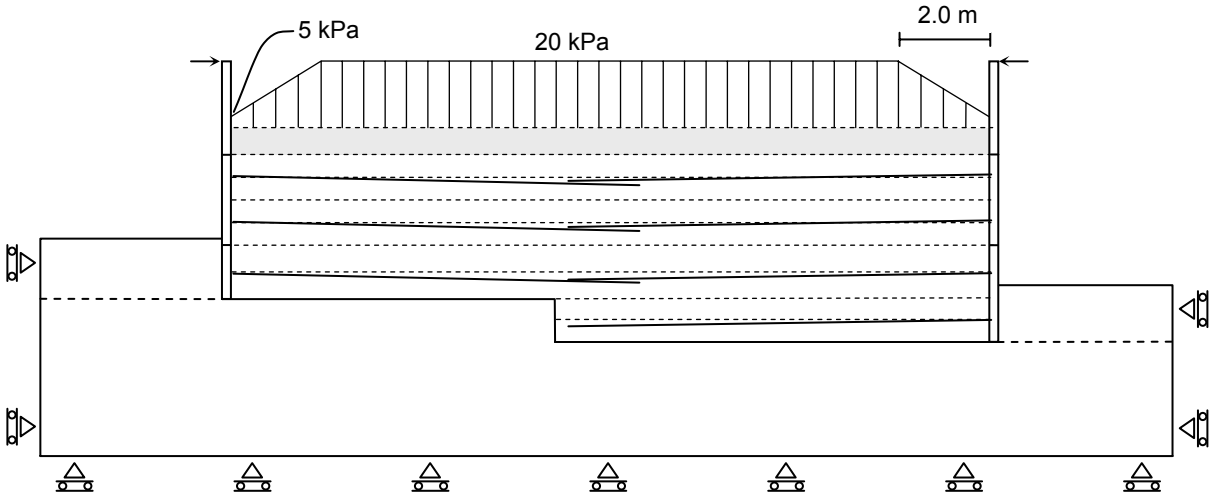


Figure 2-41. Surcharge load applied at the top and the system brought to equilibrium. and stiffness updated under new stress conditions. The surcharge removed and the system brought back to equilibrium. and stiffness updated under new stress conditions. Surcharge is placed to simulate the compaction efforts.

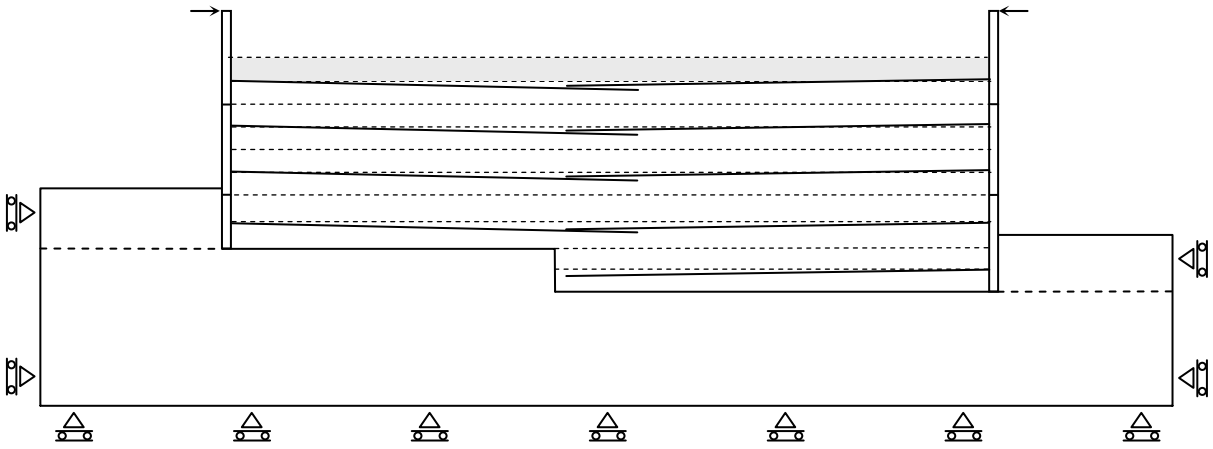

Figure 2-42. New lift placed along with the new level of reinforcements. Above procedures repeated.

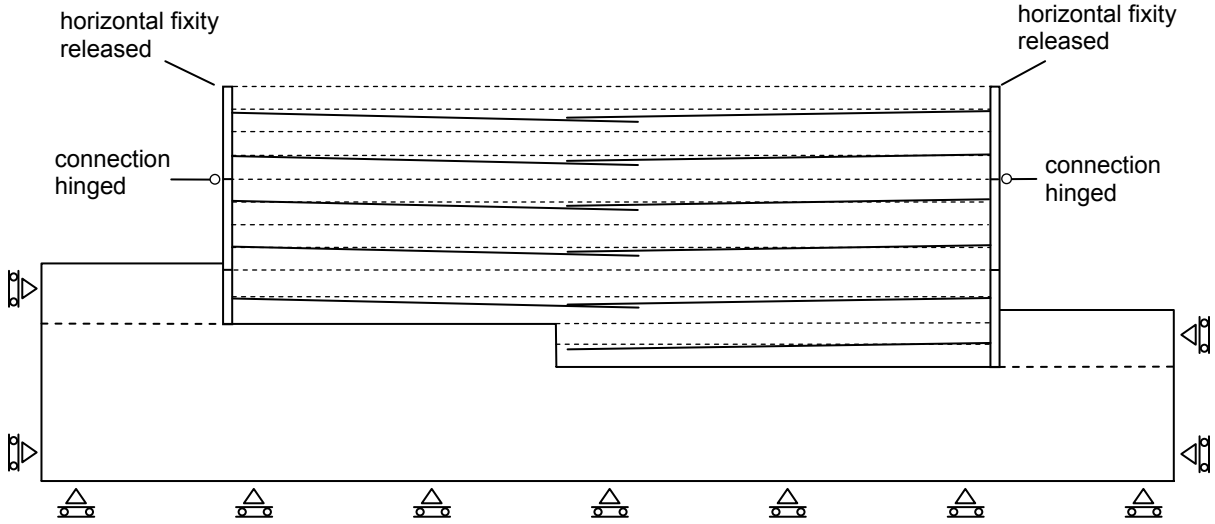


Figure 2-43. All lifts for the facing panels in place and the horizontal fixity of the top of the facing panels removed. Moment connection between the facing panels released and a hinge defined at the connection.

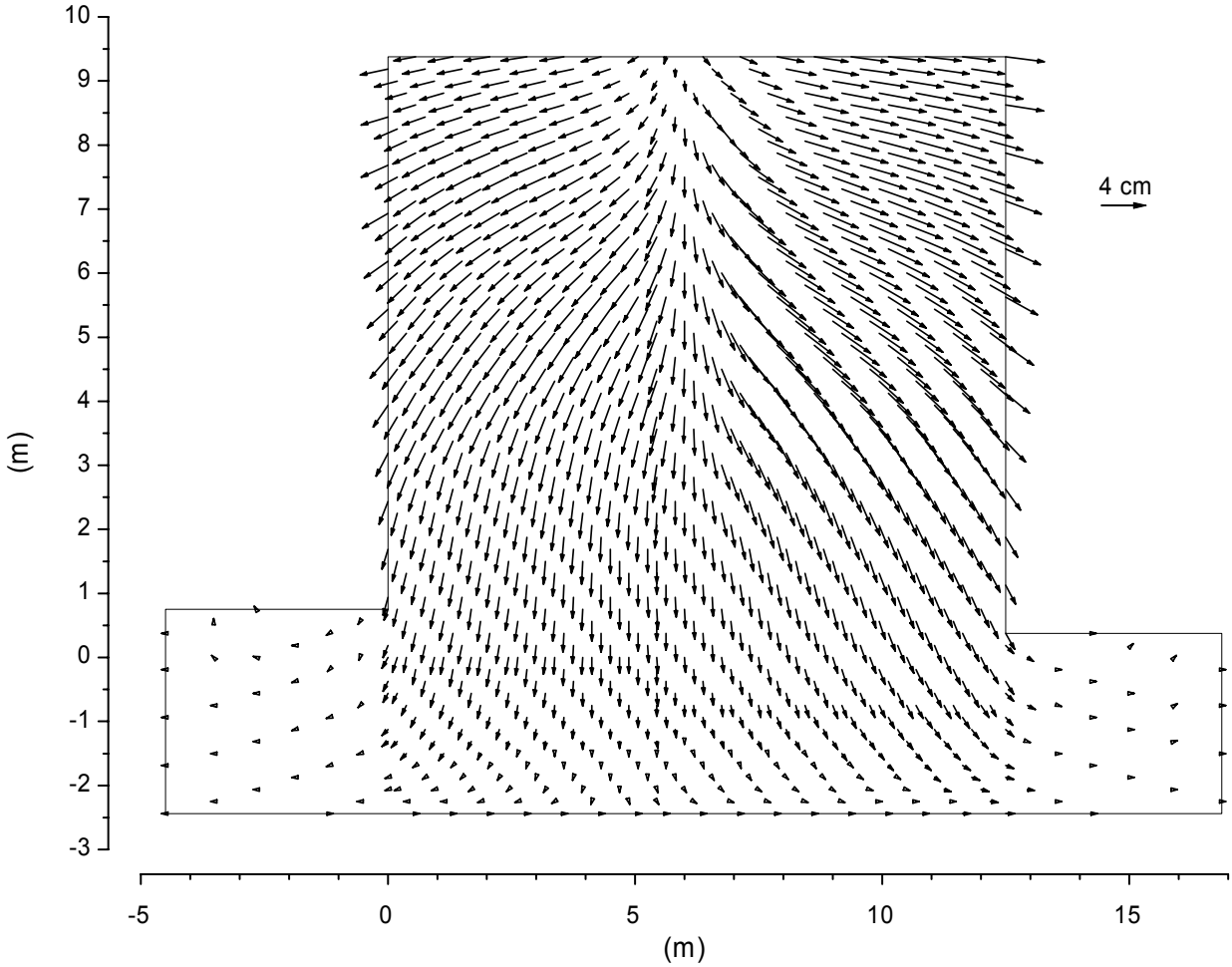


Figure 2-44. Displacement vectors at the end of construction

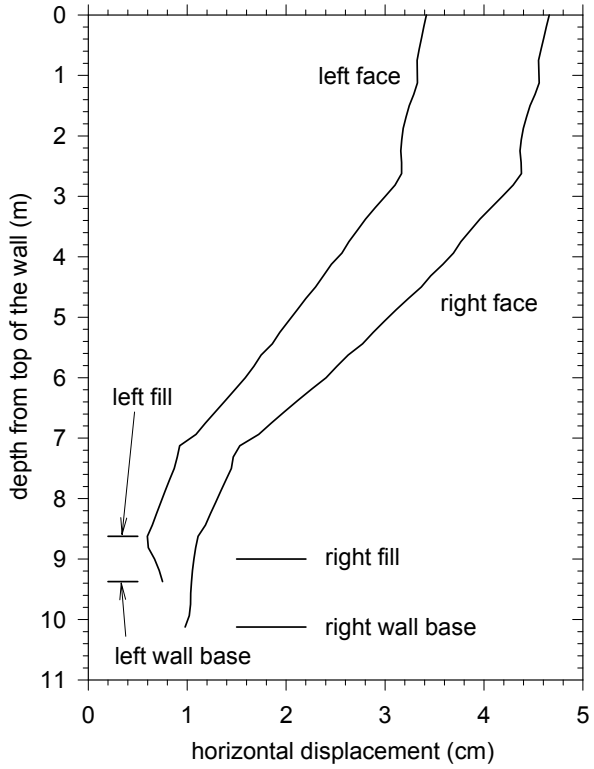


Figure 2-45. Horizontal displacement of the wall faces (end-of-construction)

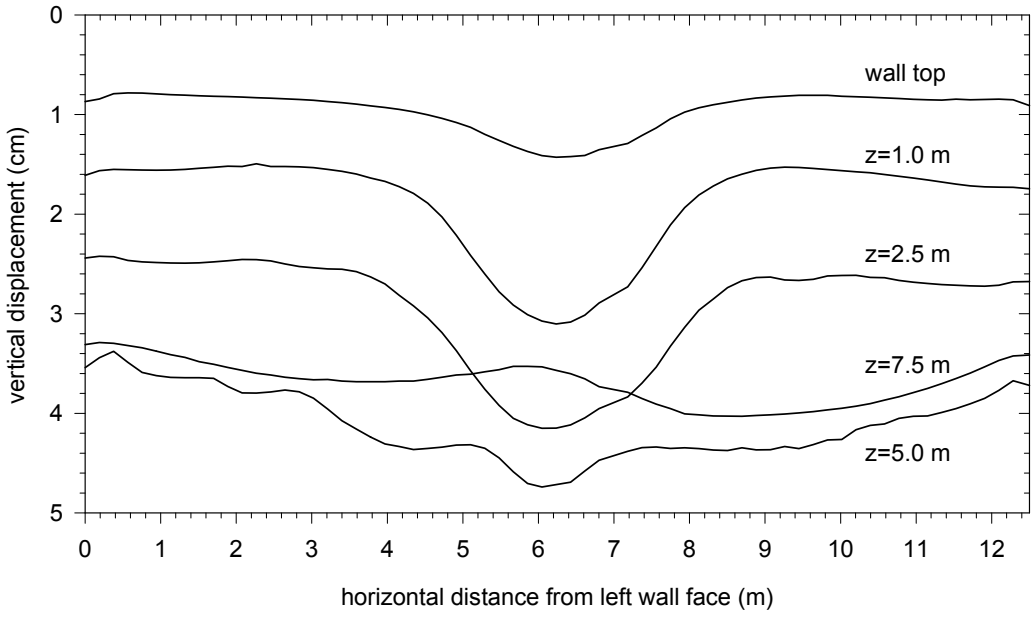


Figure 2-46. Vertical displacement along the wall height (end-of-construction)

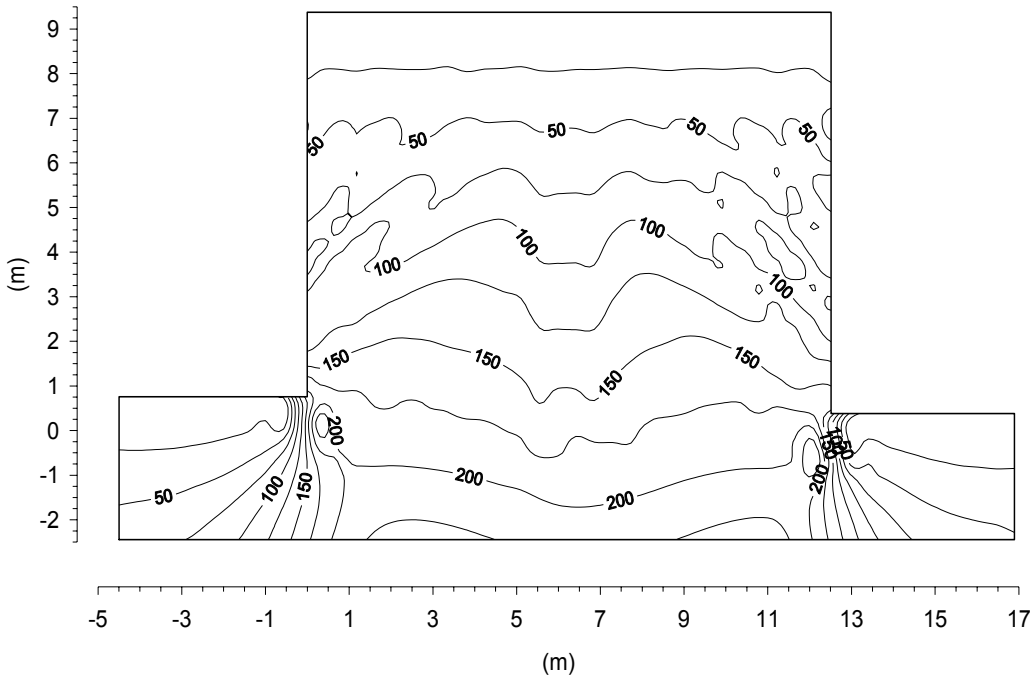


Figure 2-47. Vertical stresses in the model at the end of construction ($\sigma_{yy}$ in kPa)

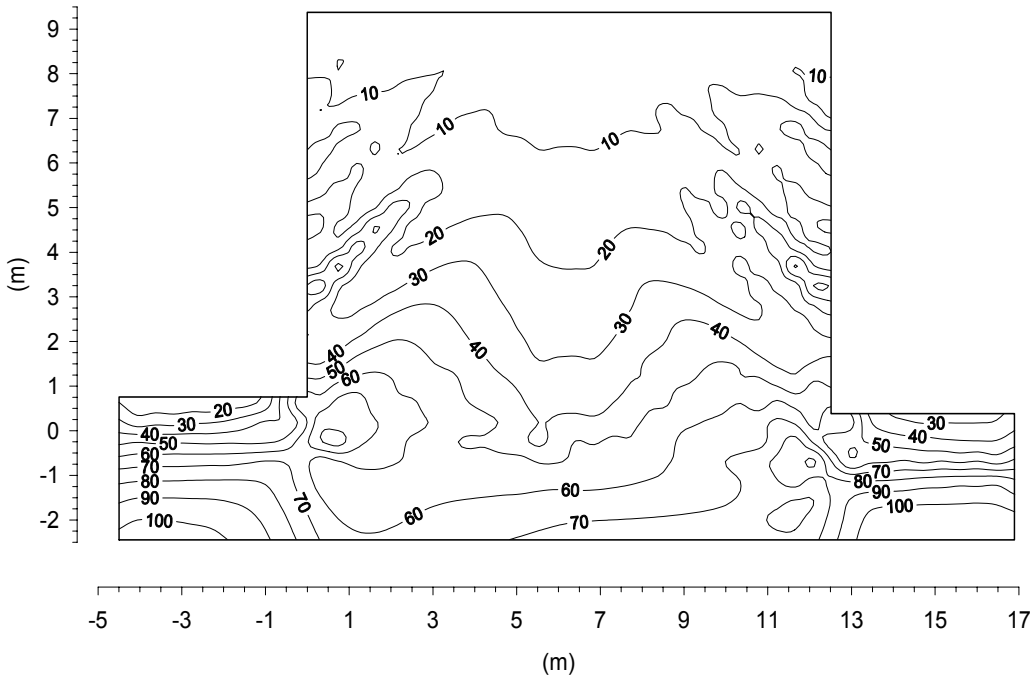


Figure 2-48. Horizontal stresses in the model at the end of construction ($\sigma_{xx}$ in kPa)

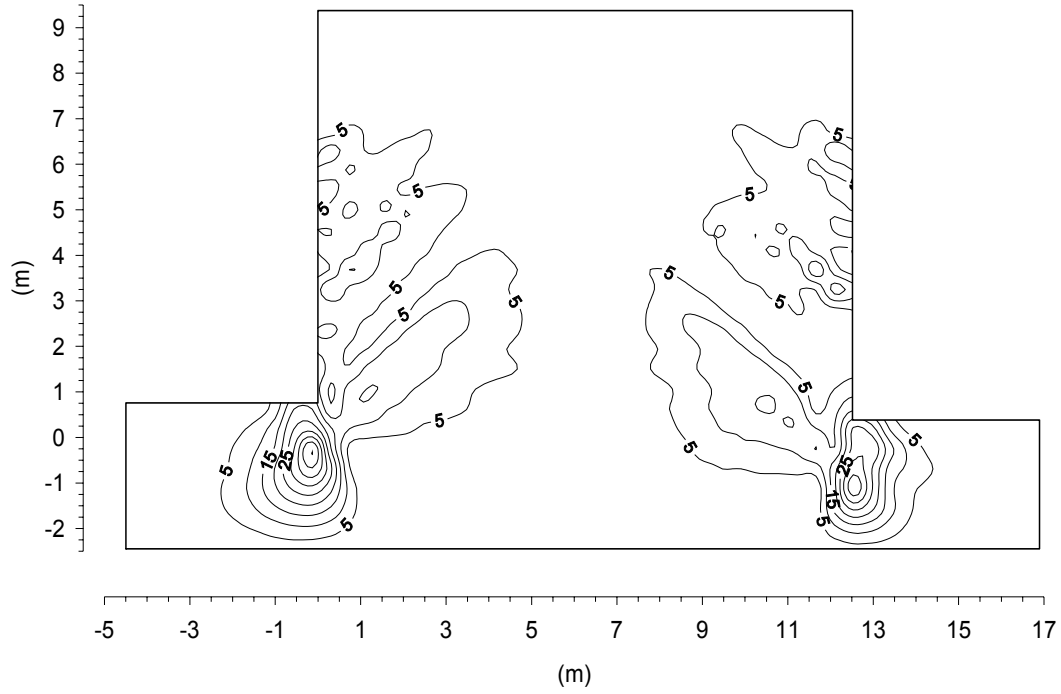


Figure 2-49. Shear stresses in the model at the end of construction ($\sigma_{xy}$ in kPa)

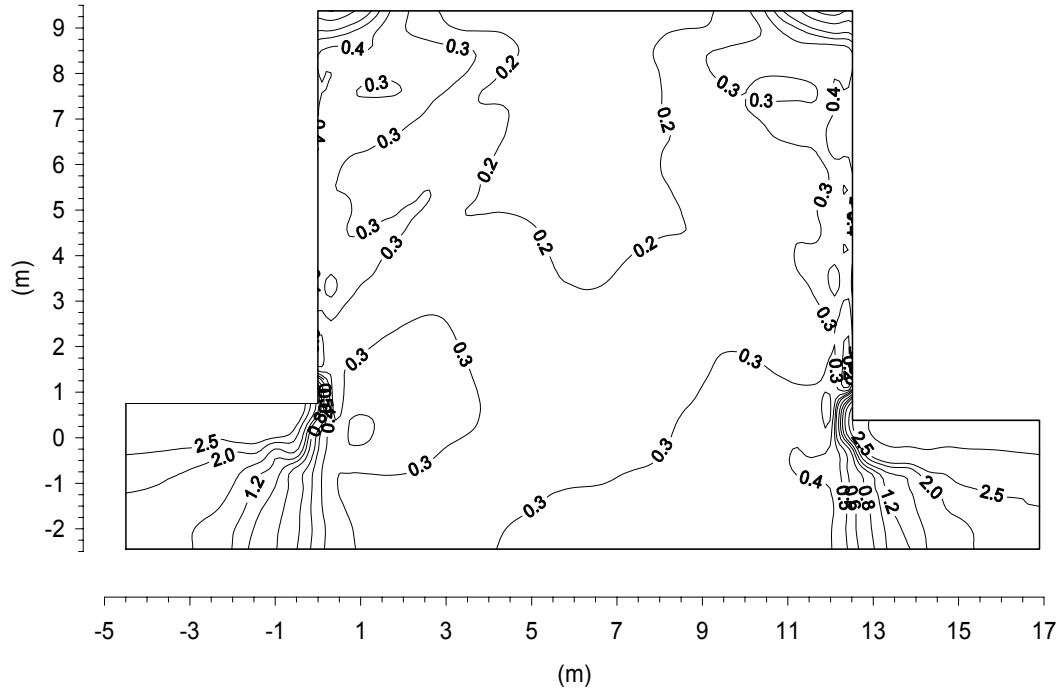


Figure 2-50. Earth pressure coefficient in the model ($K=\sigma_{xx}/\sigma_{yy}$)

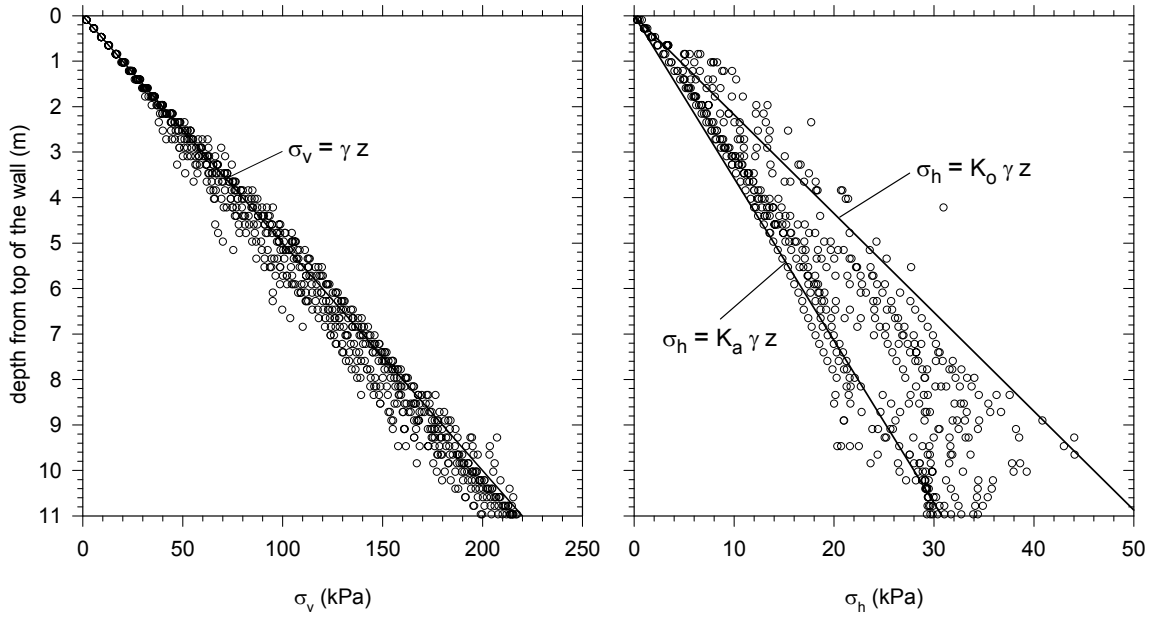


Figure 2-51. Vertical and horizontal stresses in the wall at the end of construction

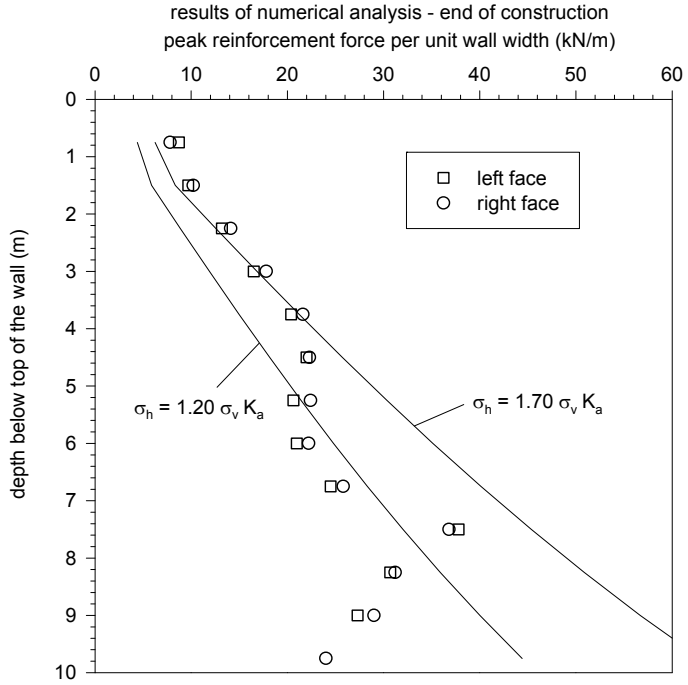


Figure 2-52. Maximum reinforcement forces following the construction simulation relative to the upper and lower bounds that would be used for static design

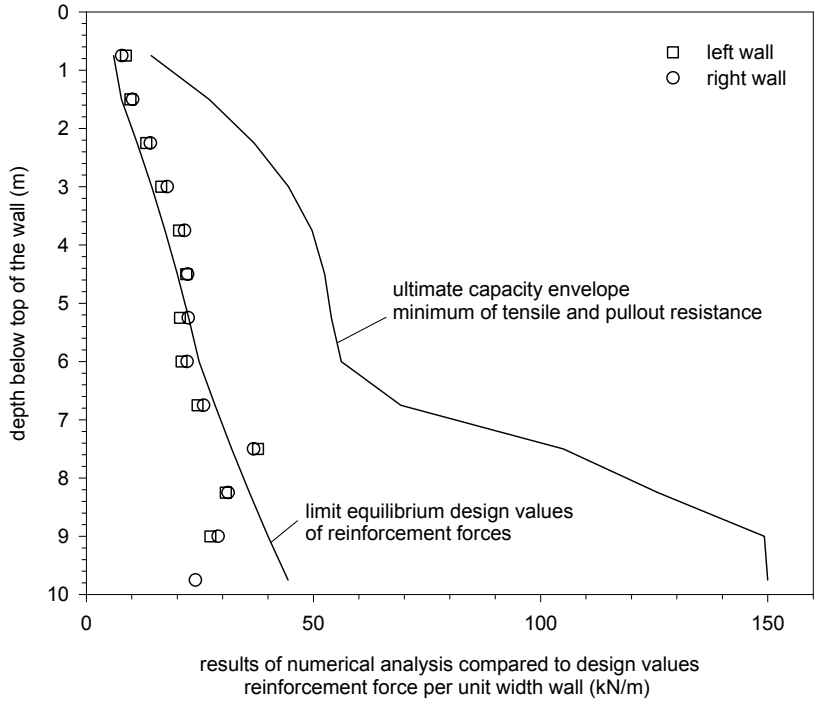


Figure 2-53. Calculated reinforcement forces in comparison to design values suggested by the limit equilibrium method and ultimate reinforcement capacity envelope

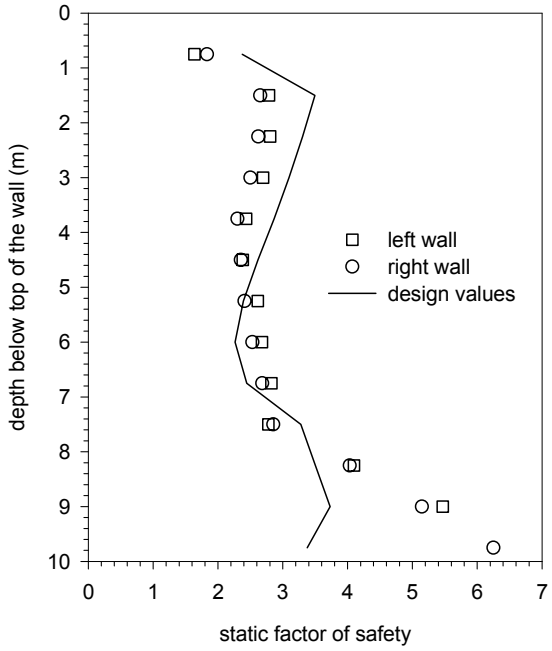


Figure 2-54. Static factor of safety from calculated values and design forces

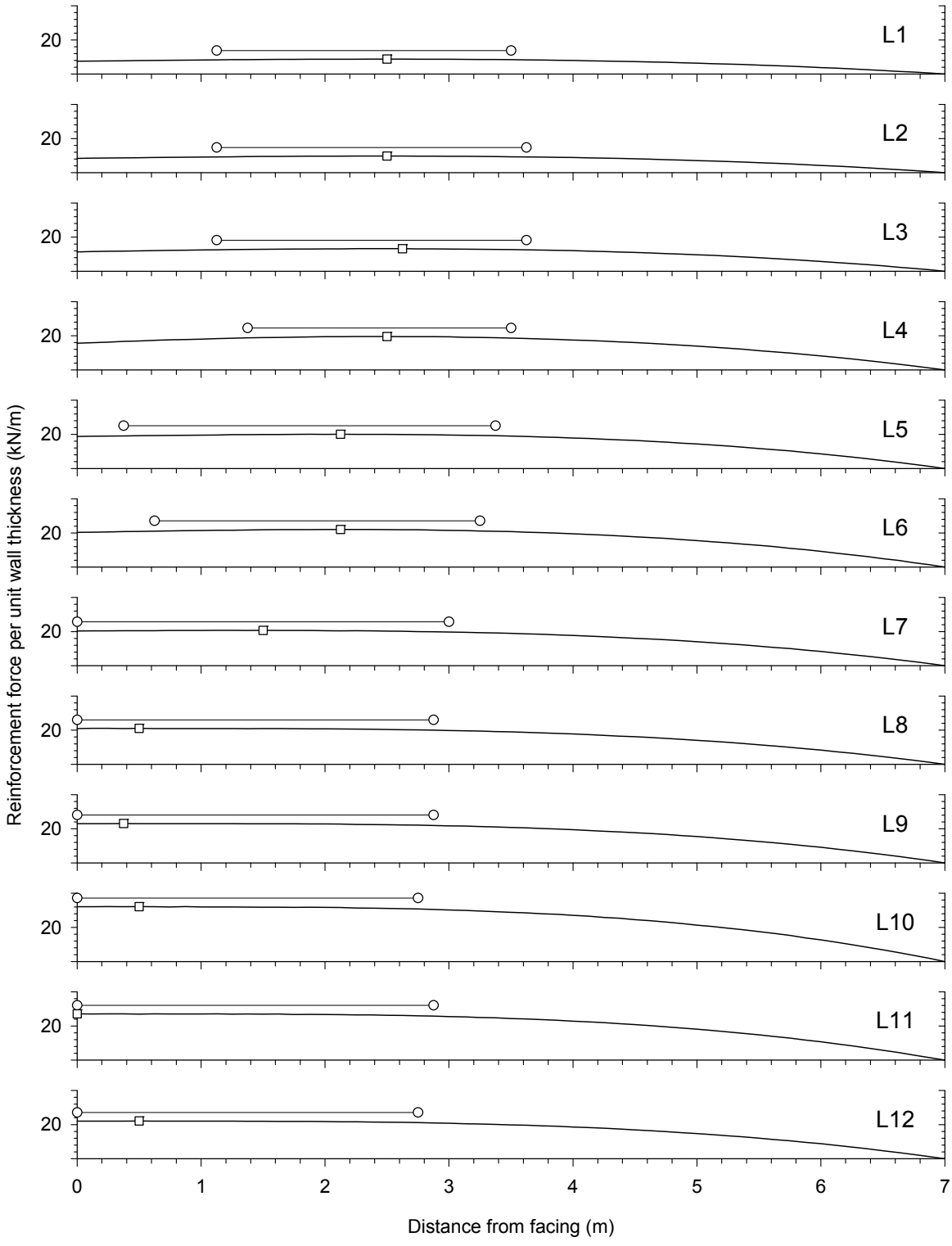


Figure 2-55. Distribution of reinforcement forces at the end of static analysis – left wall

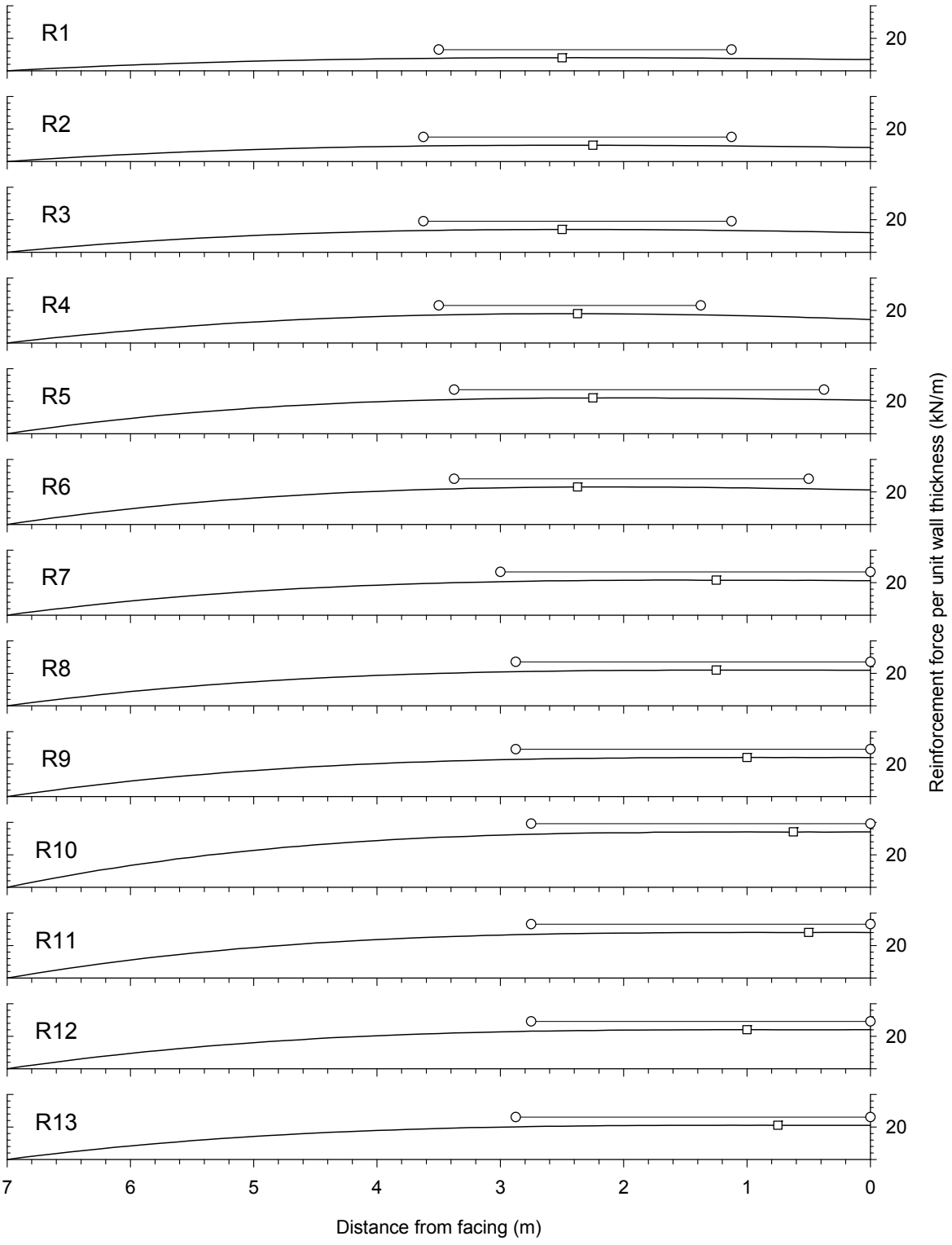


Figure 2-56. Distribution of reinforcement forces at the end of static analysis – right wall

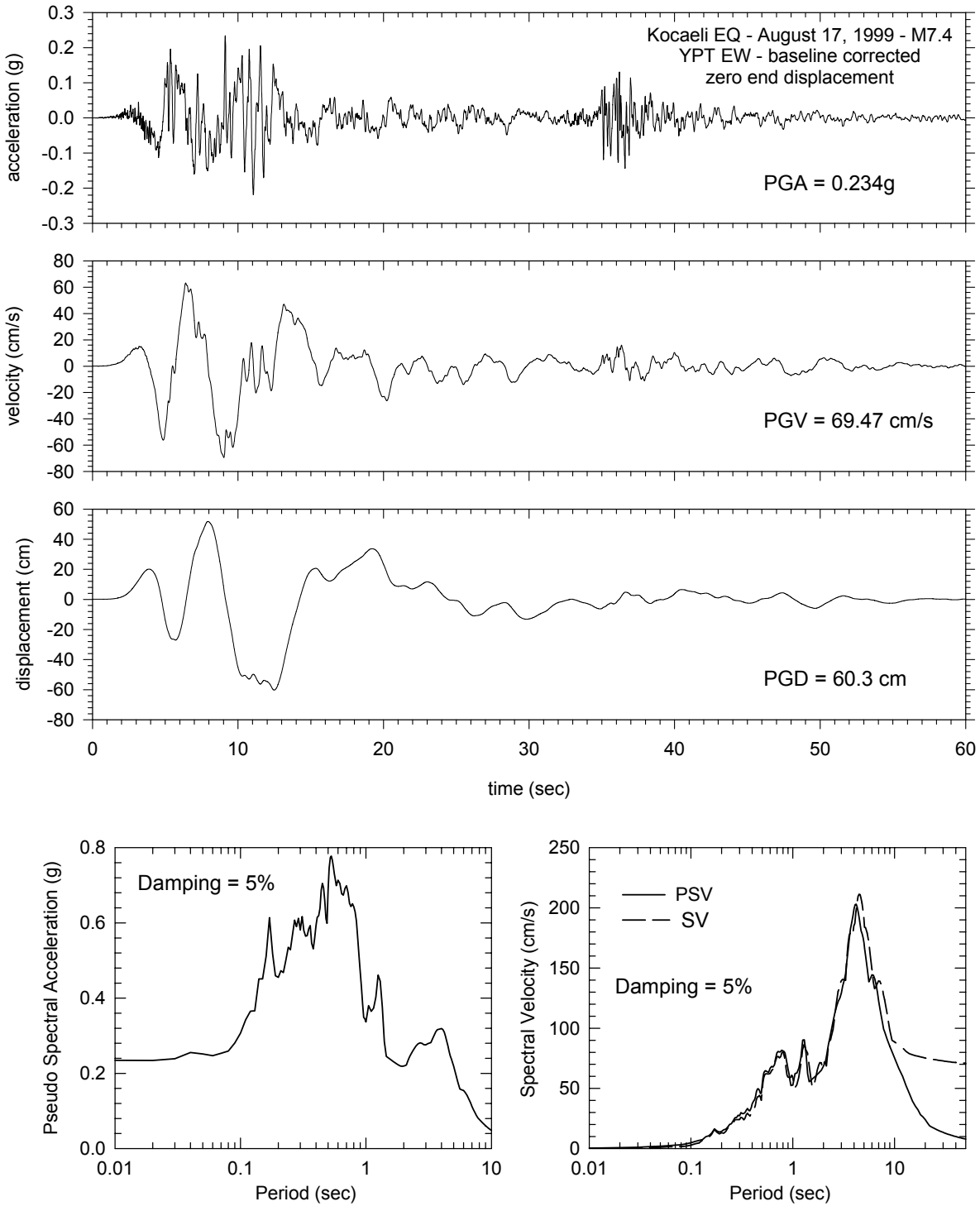


Figure 2-57. Time histories and response spectra of the record used in the analyses – Kocaeli Earthquake YPT Station EW component (record above is bandpass-filtered and baseline-corrected for zero end velocity and displacement).

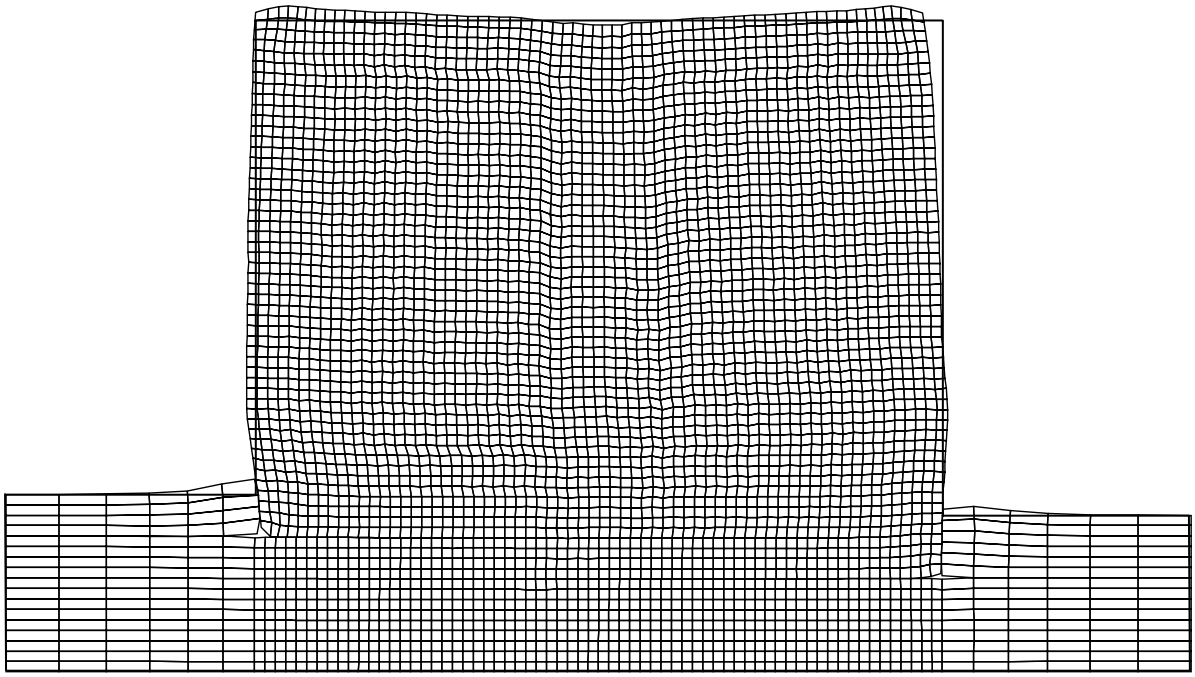

Figure 2-58. Deformed shape of the finite difference grid after shaking (no exaggeration) and comparisons between predicted and observed displacements.

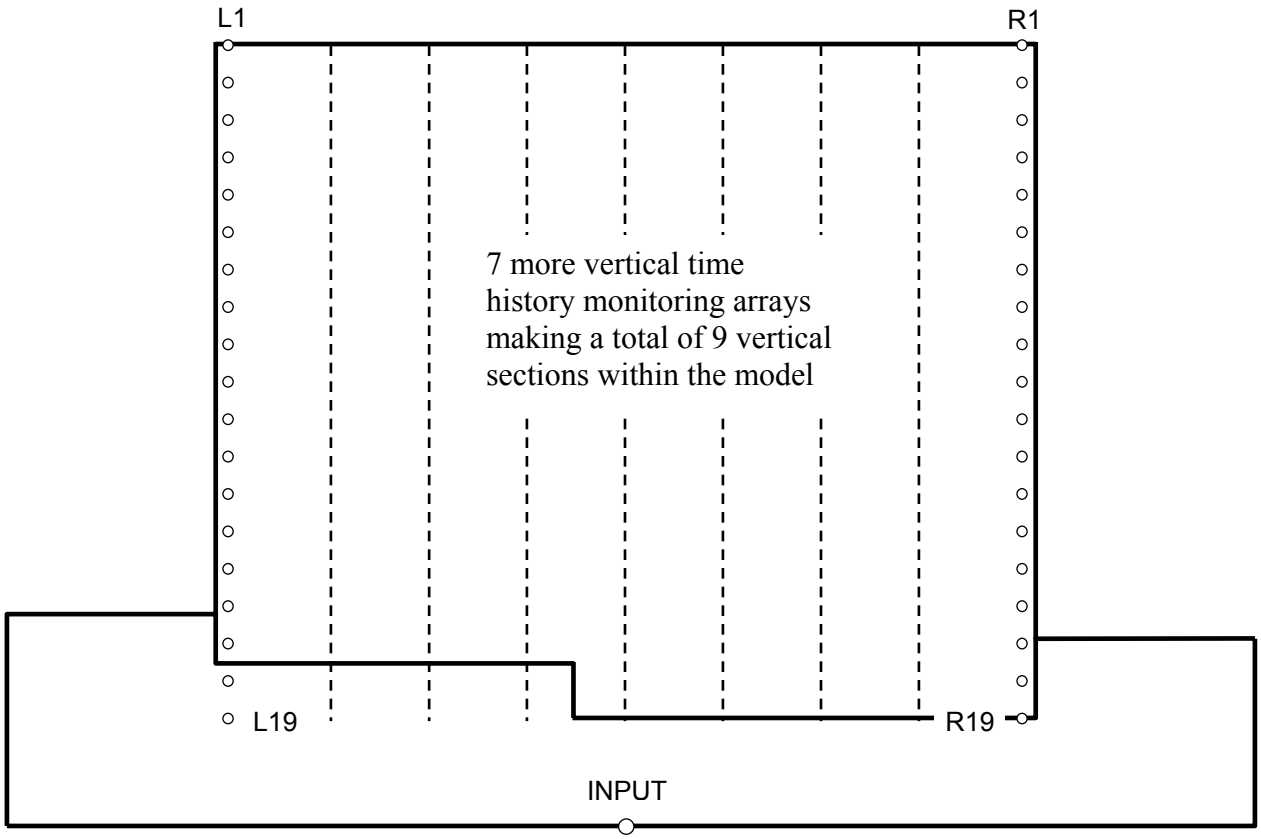


Figure 2-59. Location of nodal points where horizontal displacement is monitored throughout dynamic analysis. Nodal points are arranged to form 9 vertical arrays within the model. Two arrays shown in details whereas the remaining arrays just shown schematically.

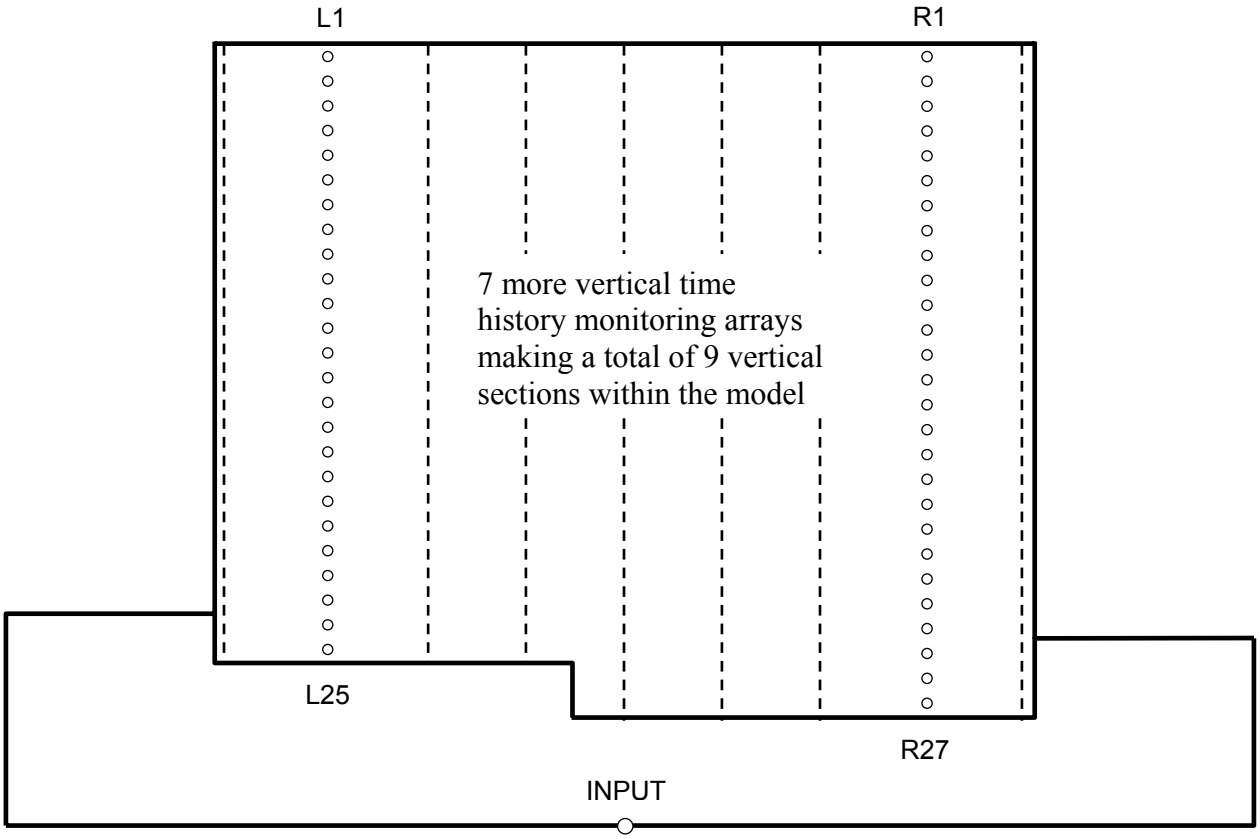


Figure 2-60. Locations where horizontal stress time histories were monitored during the dynamic analysis. Two vertical arrays behind each face shown with individual history locations and 7 other vertical sections of arrays shown with dashed lines.

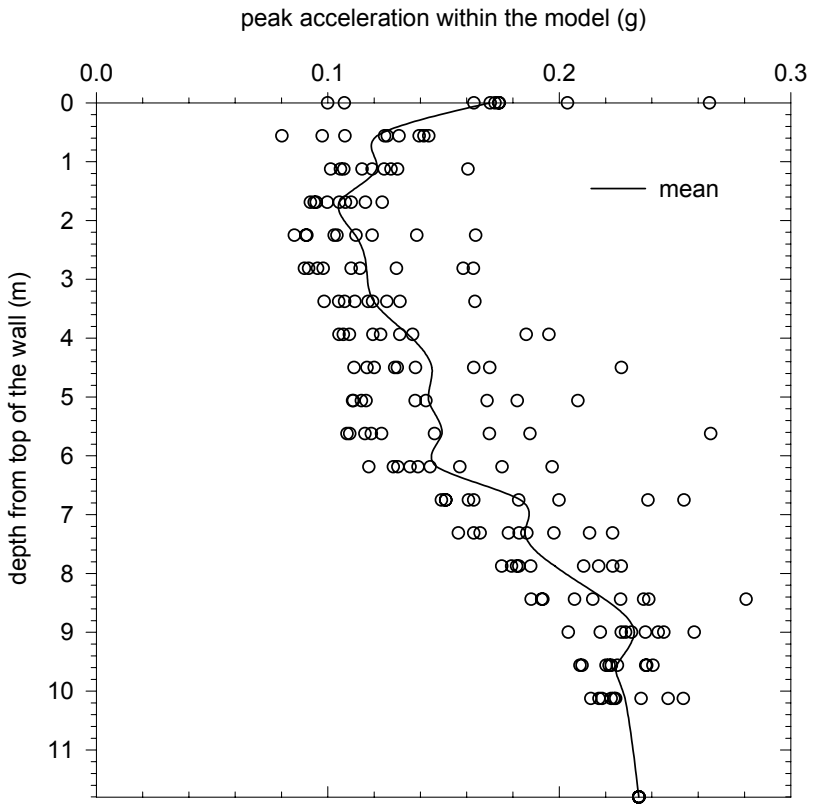


Figure 2-61. Variation of peak acceleration at various points within the wall

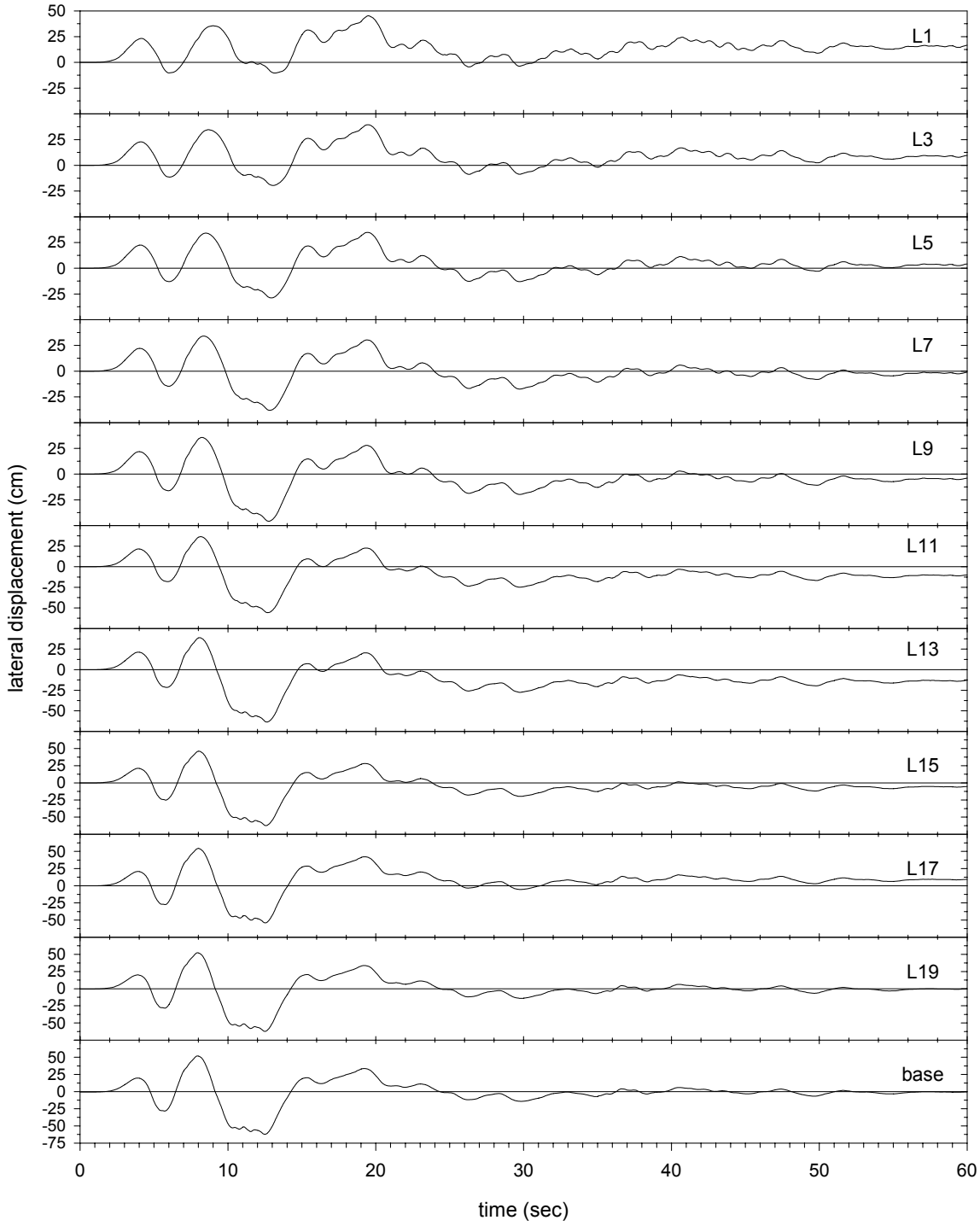


Figure 2-62. Displacement time histories along the left face of the wall (see key in Figure 2-59). Predicted maximum displacement was 16 cm, and the actual displacement was 10 cm

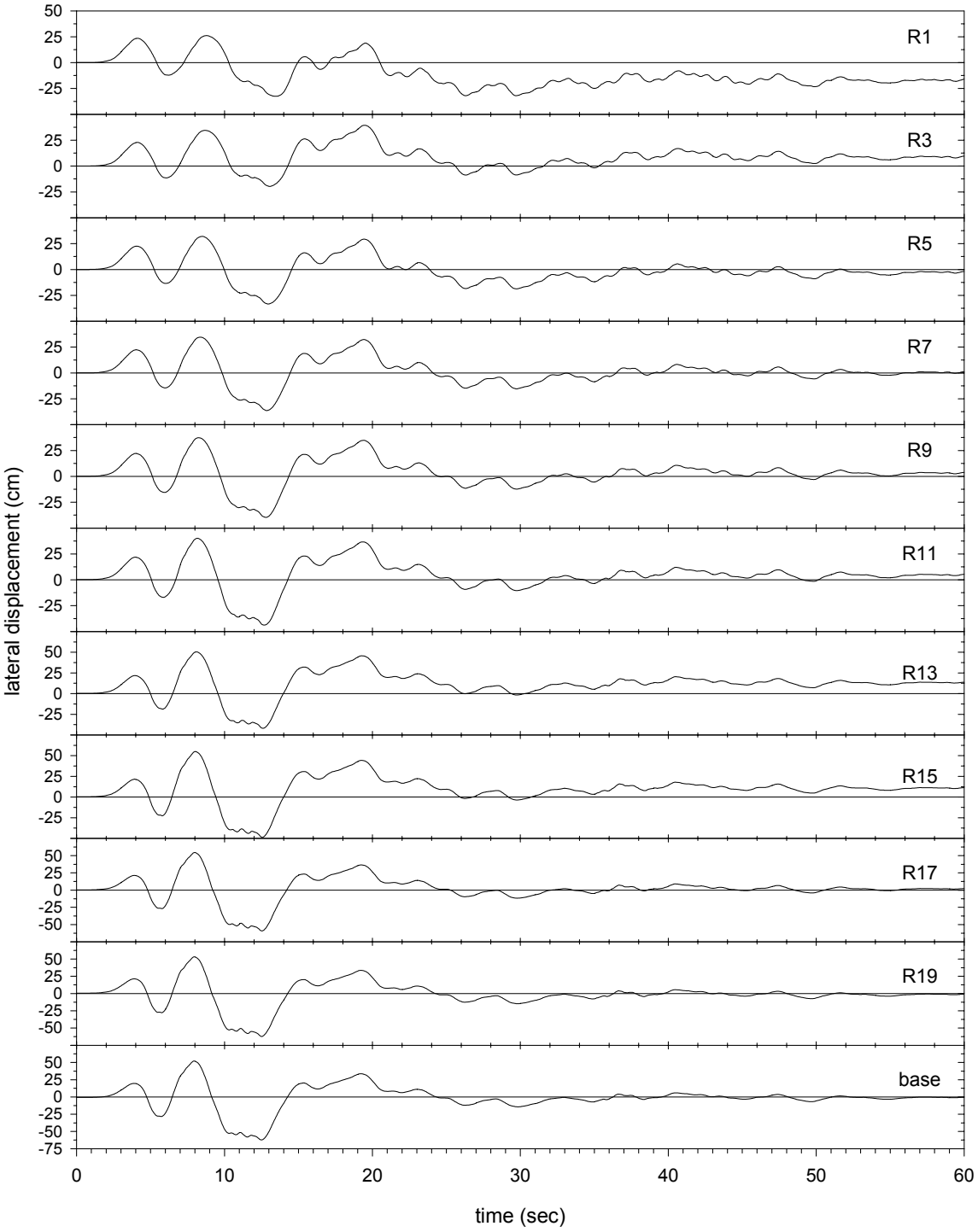


Figure 2-63. Displacement time histories along the right face of the wall (see key in Figure 2-59). Predicted maximum displacement was 16 cm, and the actual displacement was 10 cm.

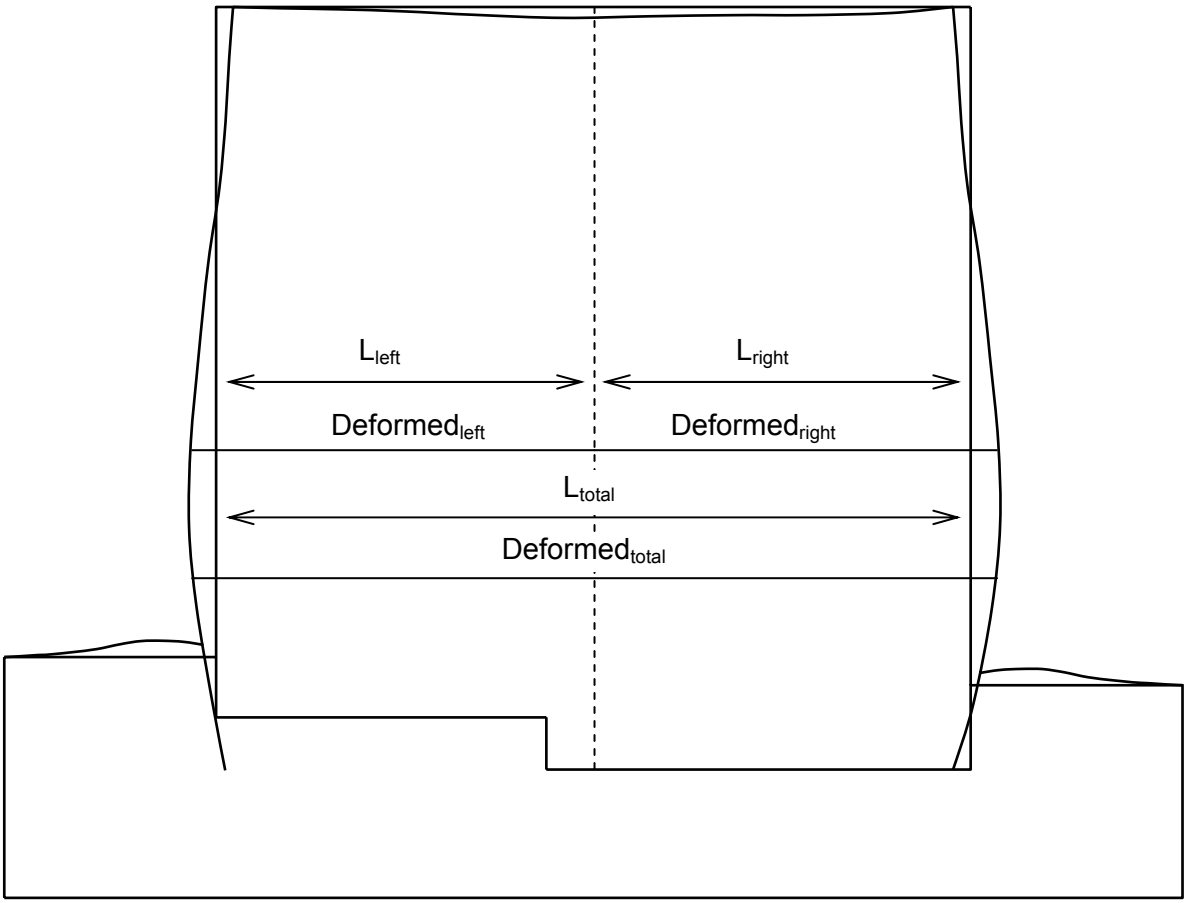


Figure 2-64. Typical deformed shape of the model at the end of shaking and the definition of deformations of respective wall sections (left, right and total).

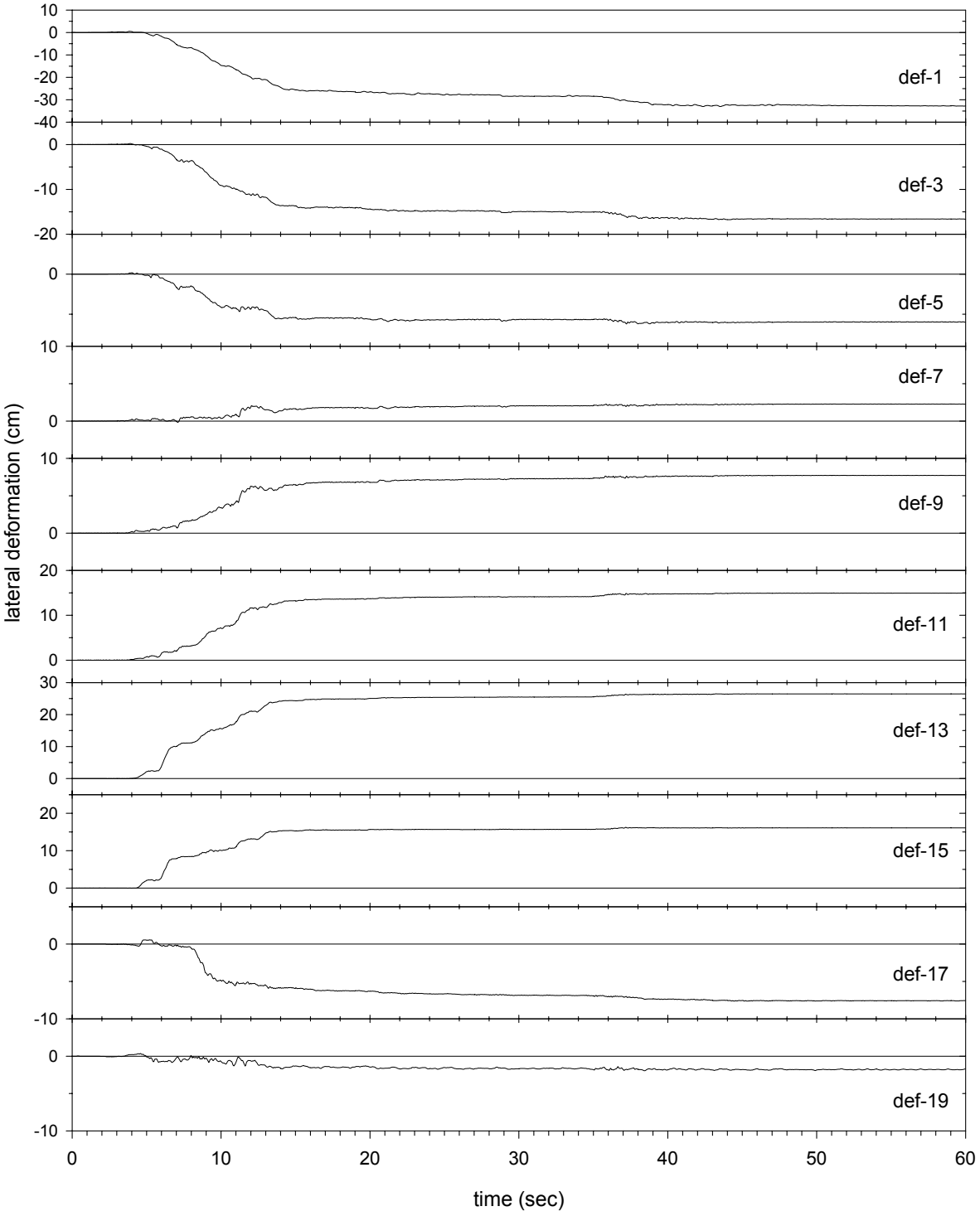


Figure 2-65. Horizontal deformation measured as the relative displacement of left and right face of the model wall. Positive values correspond to horizontal extension of model cross section.

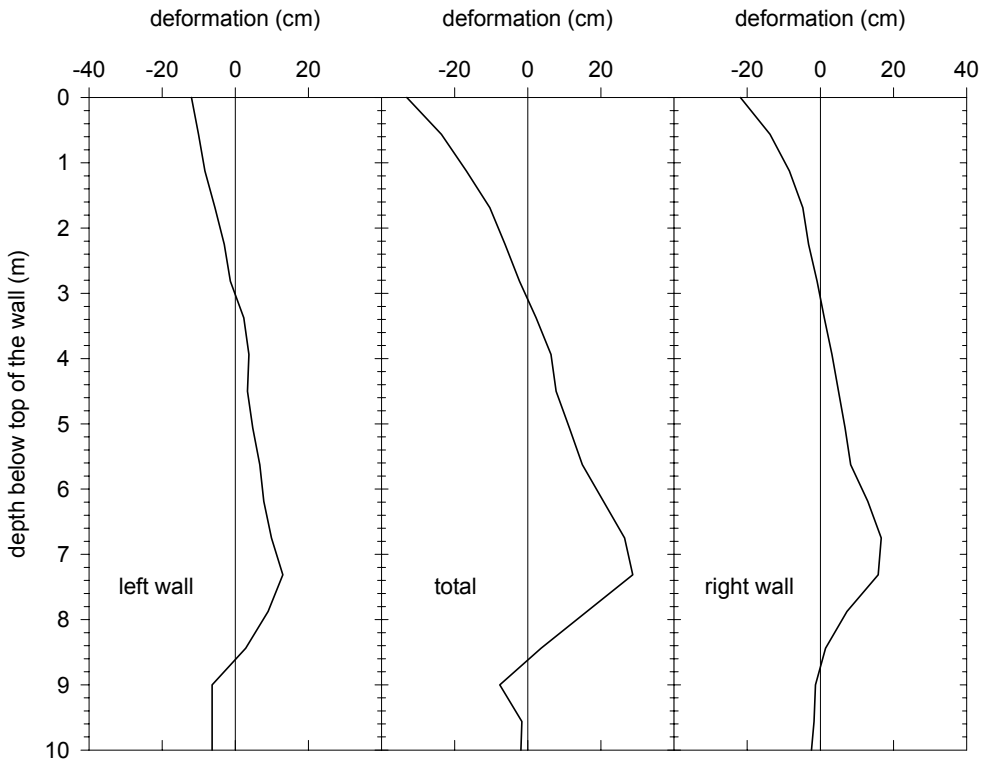


Figure 2-66. Permanent deformations along left and right sections of the wall

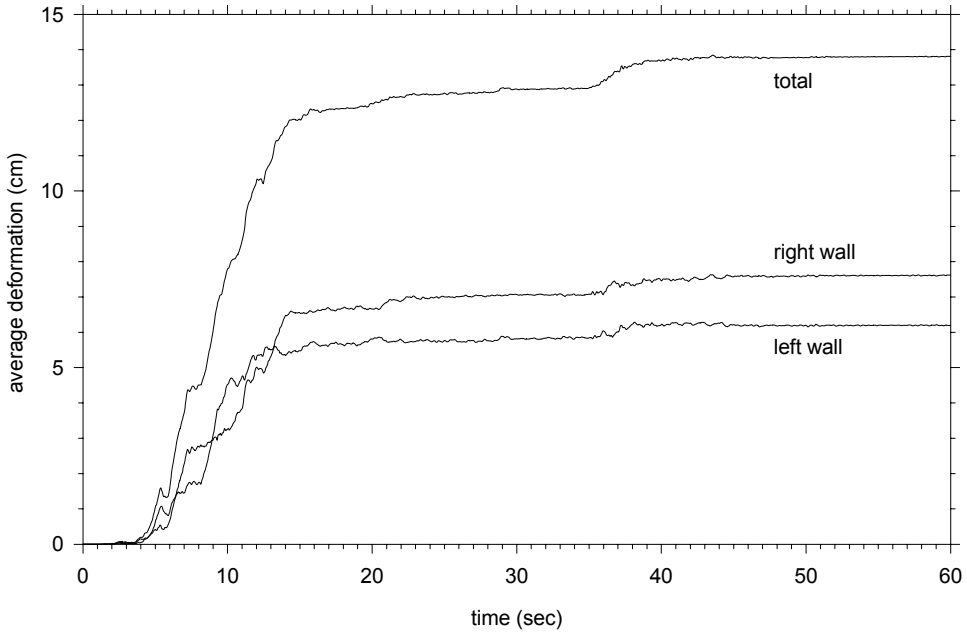


Figure 2-67. Average deformation in time. Left and right sections of the wall and total deformation

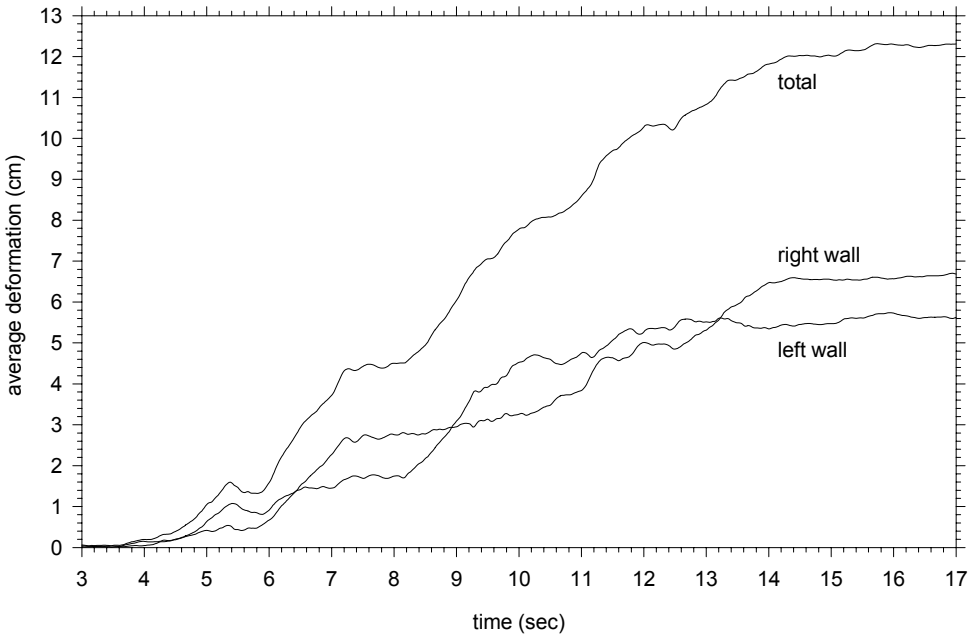


Figure 2-68. Average deformation in time. Left and right sections of the wall and total deformation. Closer look into the episode of strong shaking where majority of deformations accumulate.

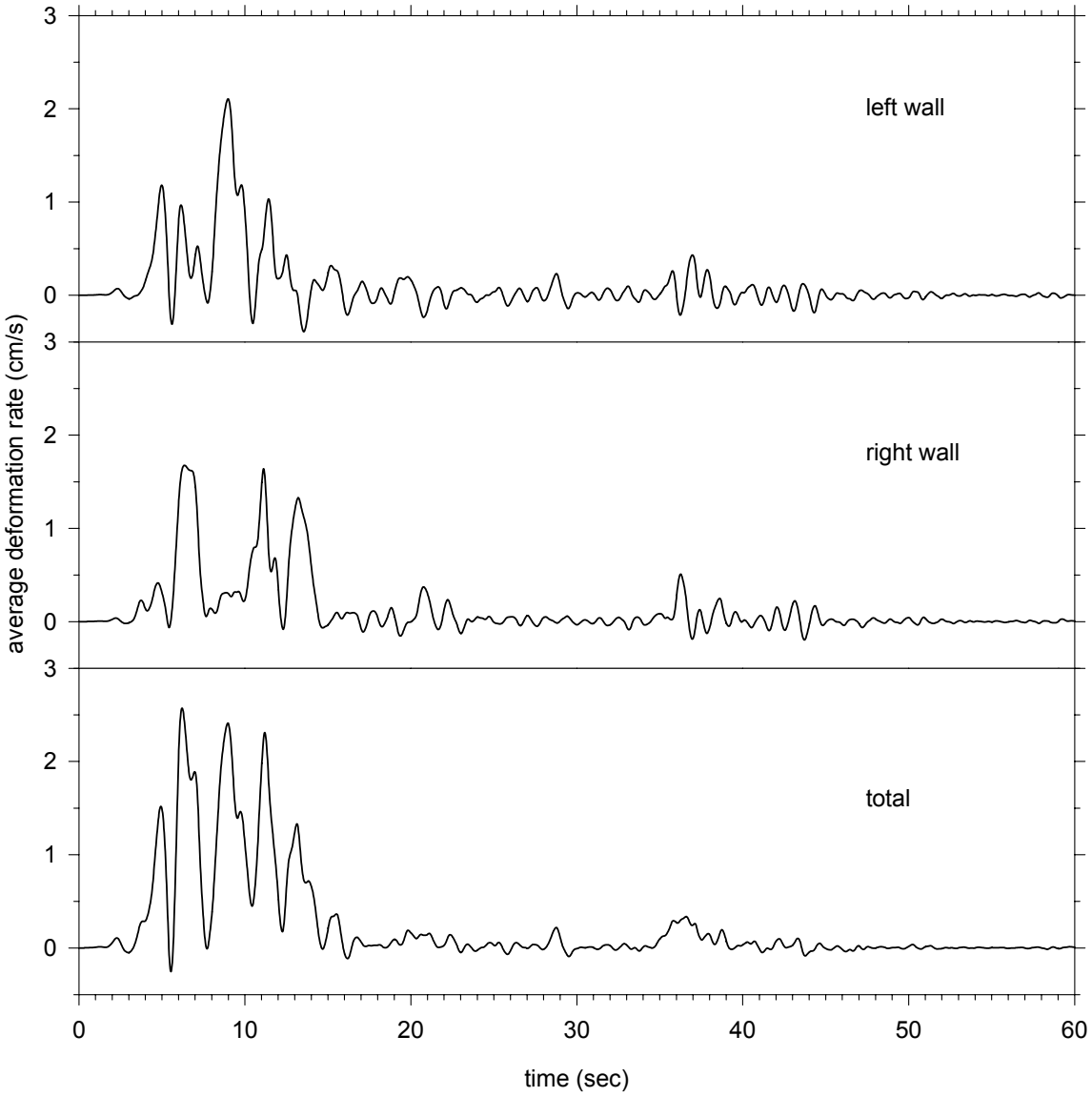


Figure 2-69. Deformation rate during shaking. Left and right sections of the wall and total deformation rate.

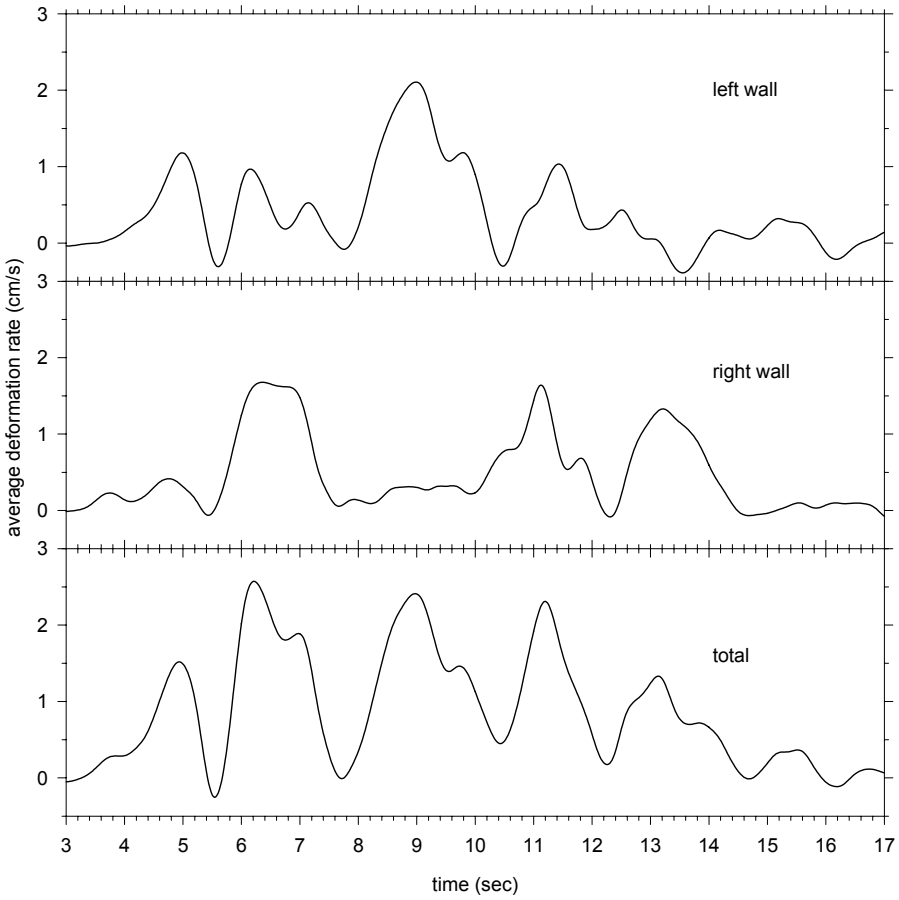


Figure 2-70. Deformation rate during shaking. Left and right sections of the wall and total deformation rate. Closer look into the episode of strong shaking where majority of deformations accumulate.

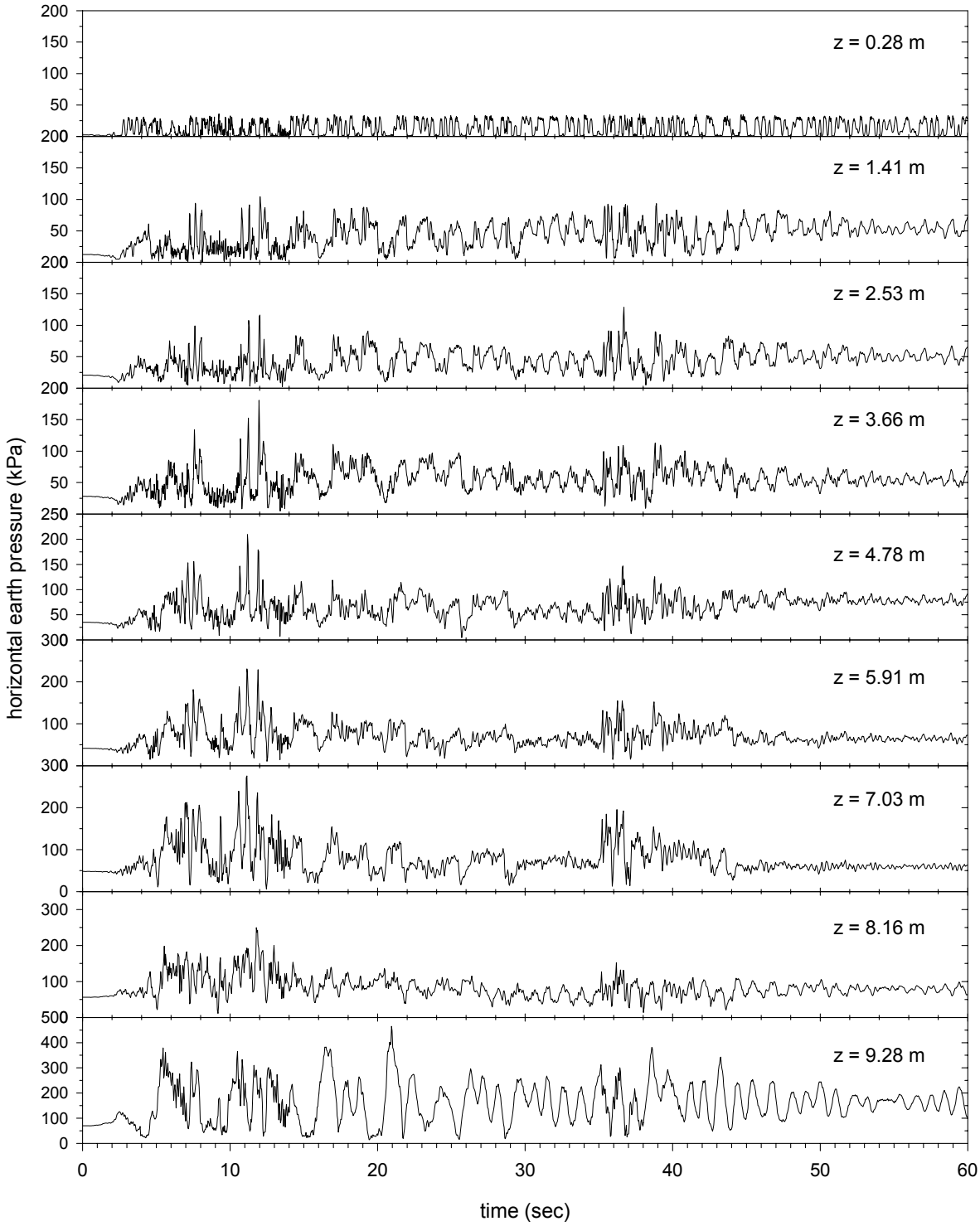


Figure 2-71. Horizontal earth pressure behind the left facing

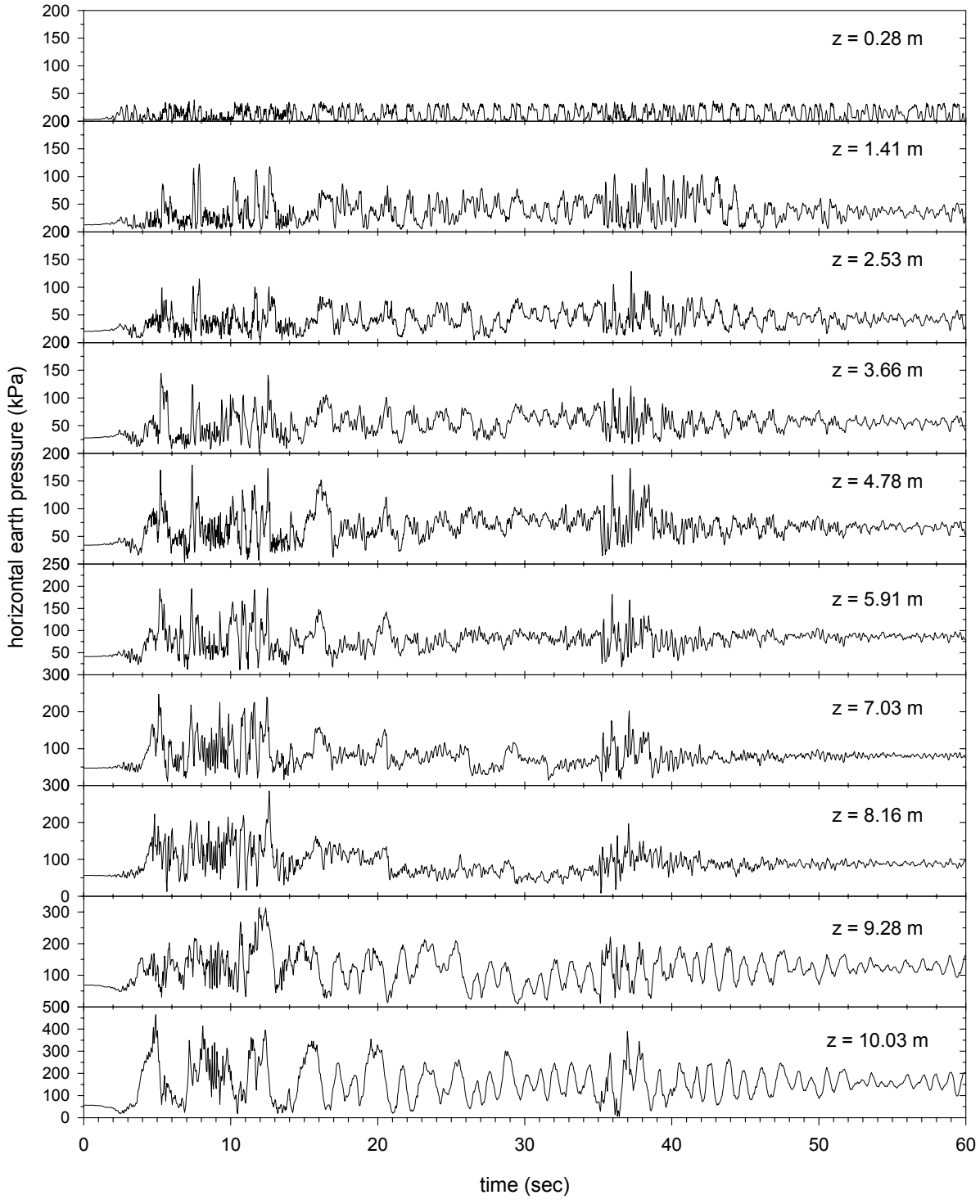


Figure 2-72. Horizontal earth pressure behind the right facing

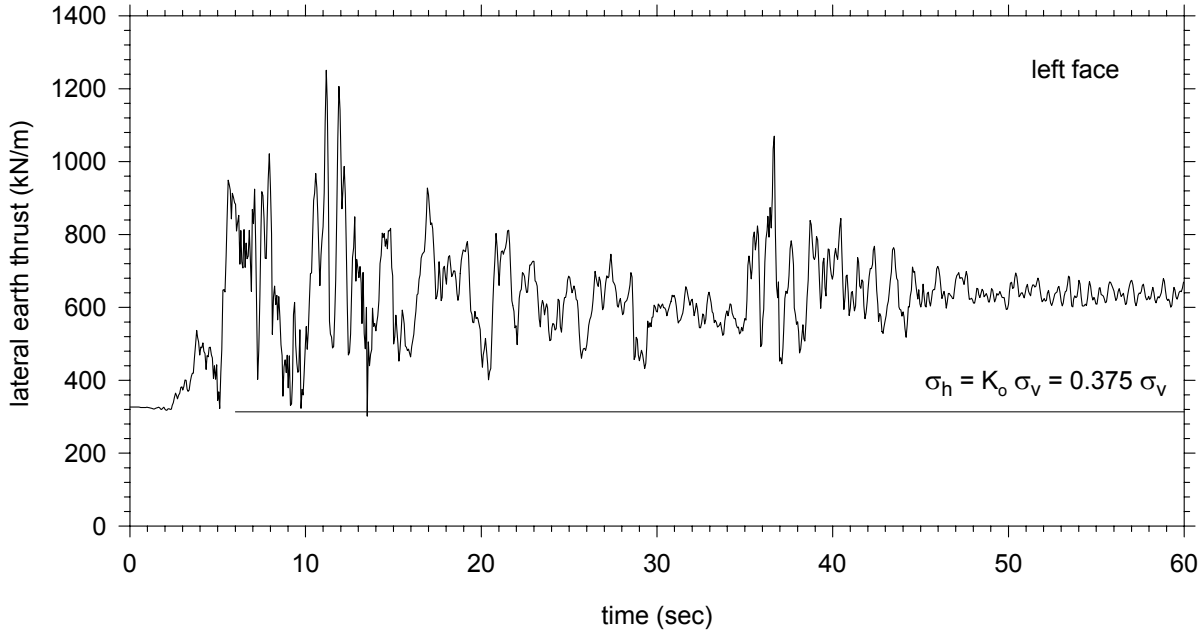


Figure 2-73. Total earth thrust behind the left facing during shaking

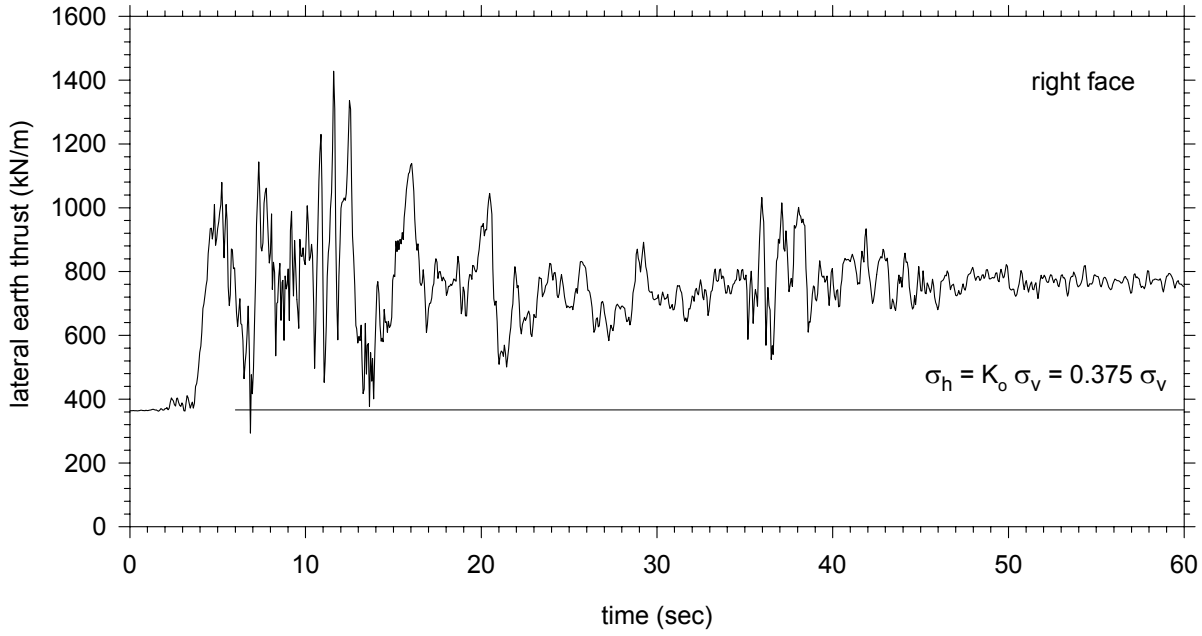


Figure 2-74. Total earth thrust behind the right facing during shaking

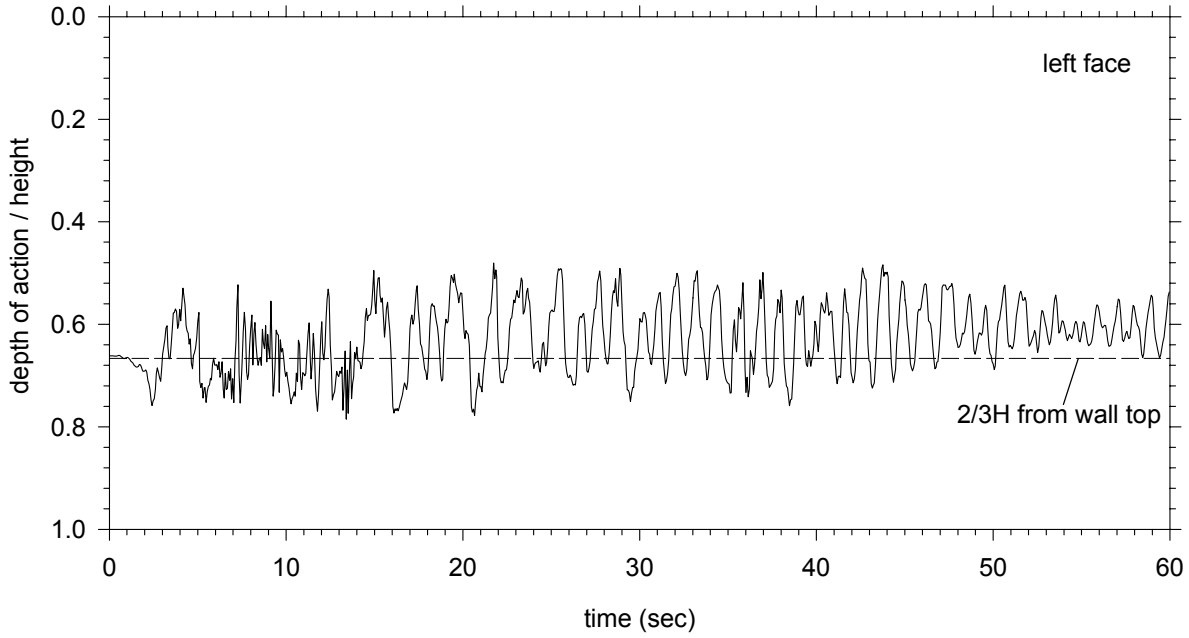


Figure 2-75. Equivalent location of action of the total earth thrust – left face.

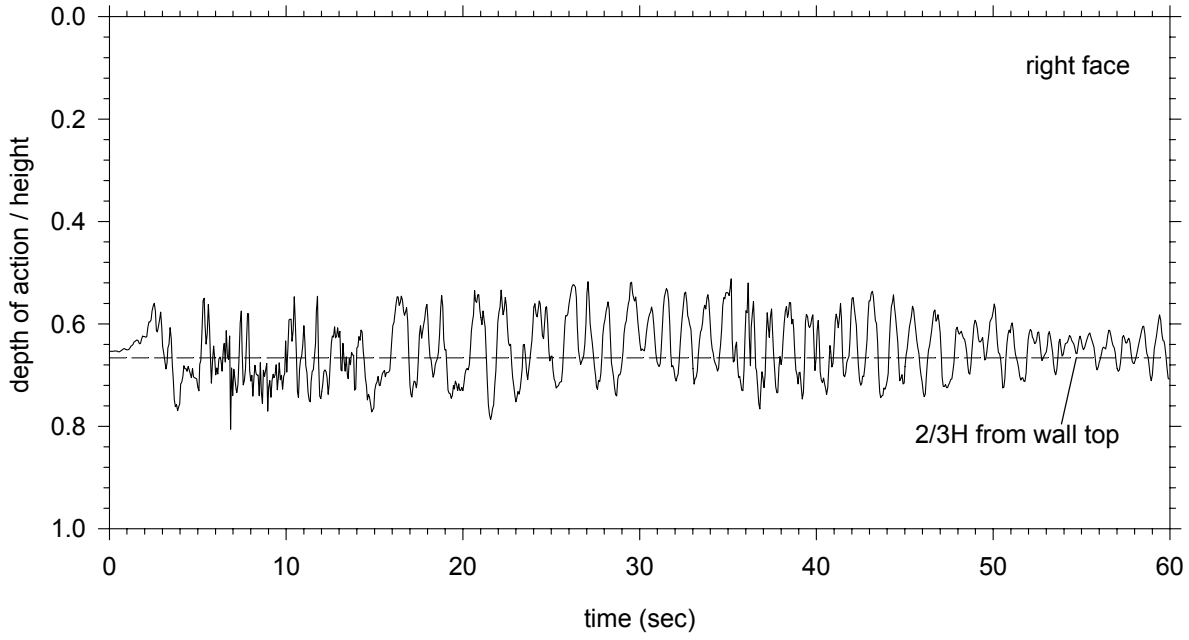


Figure 2-76. Equivalent location of action of the total earth thrust – right face.

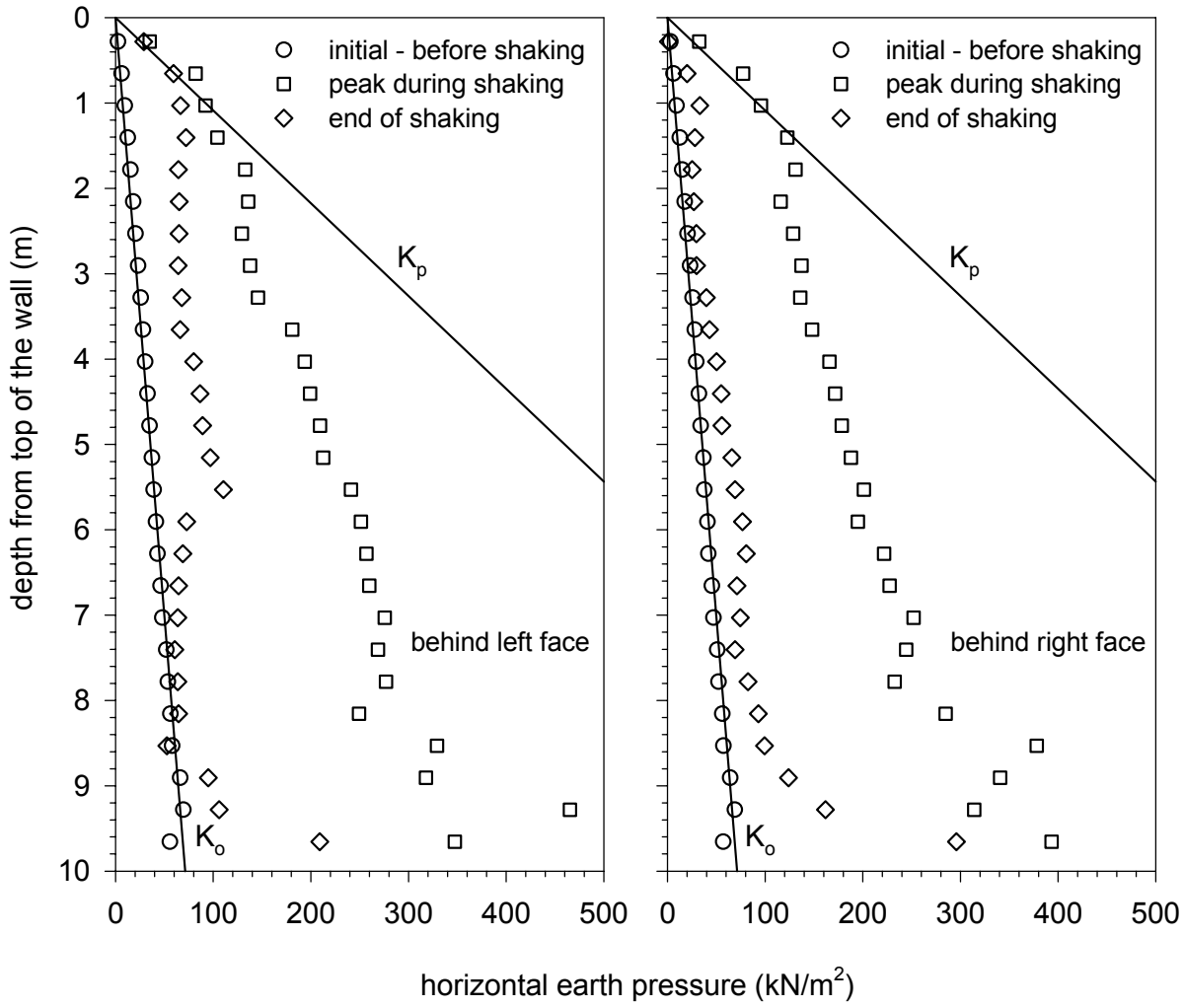


Figure 2-77. Horizontal earth pressures within the wall behind the wall faces. Peak values of earth pressure and earth pressure at the end-of-shaking in comparison to at-rest earth pressure and passive earth pressure conditions.

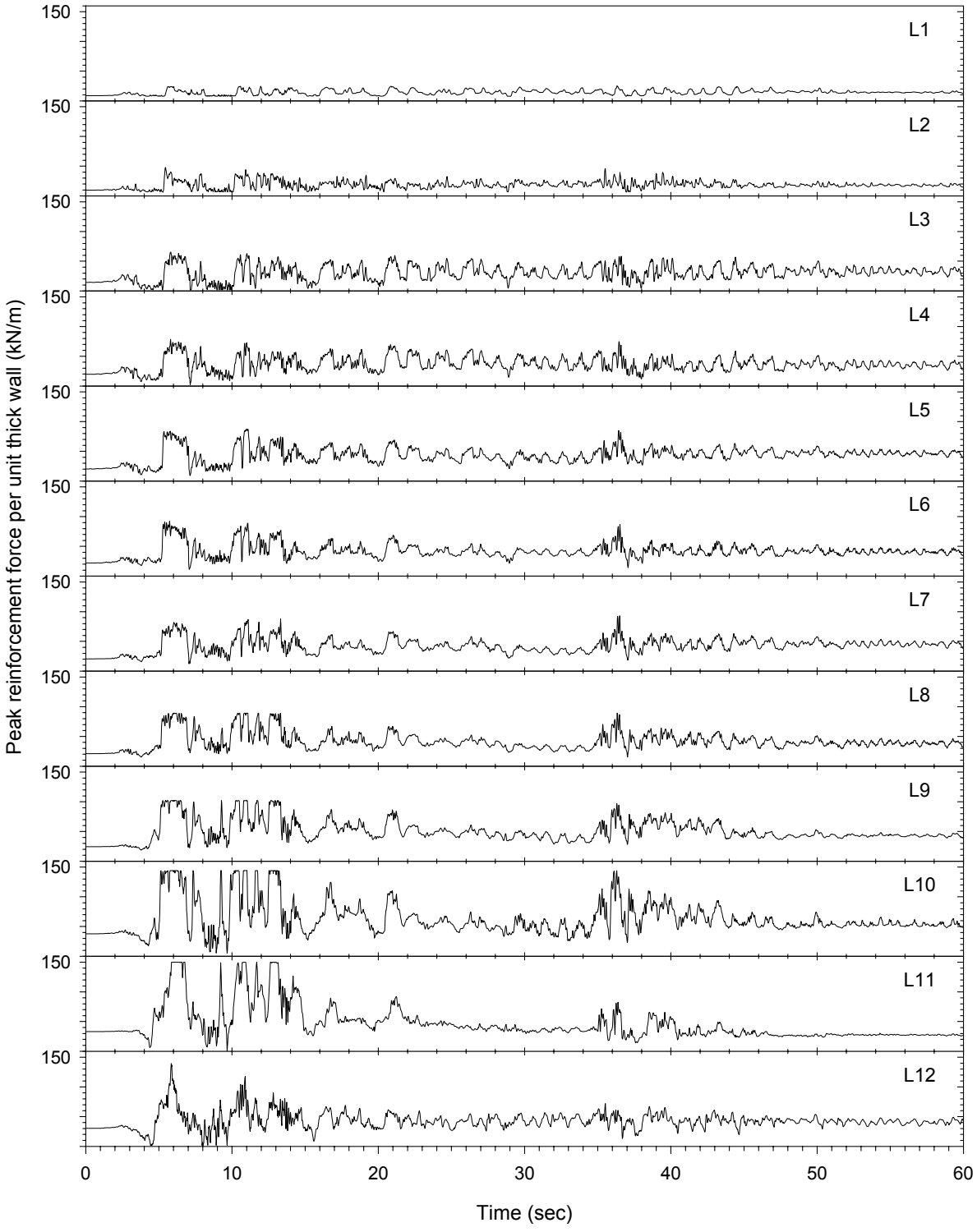


Figure 2-78. Peak reinforcement forces throughout shaking – left wall

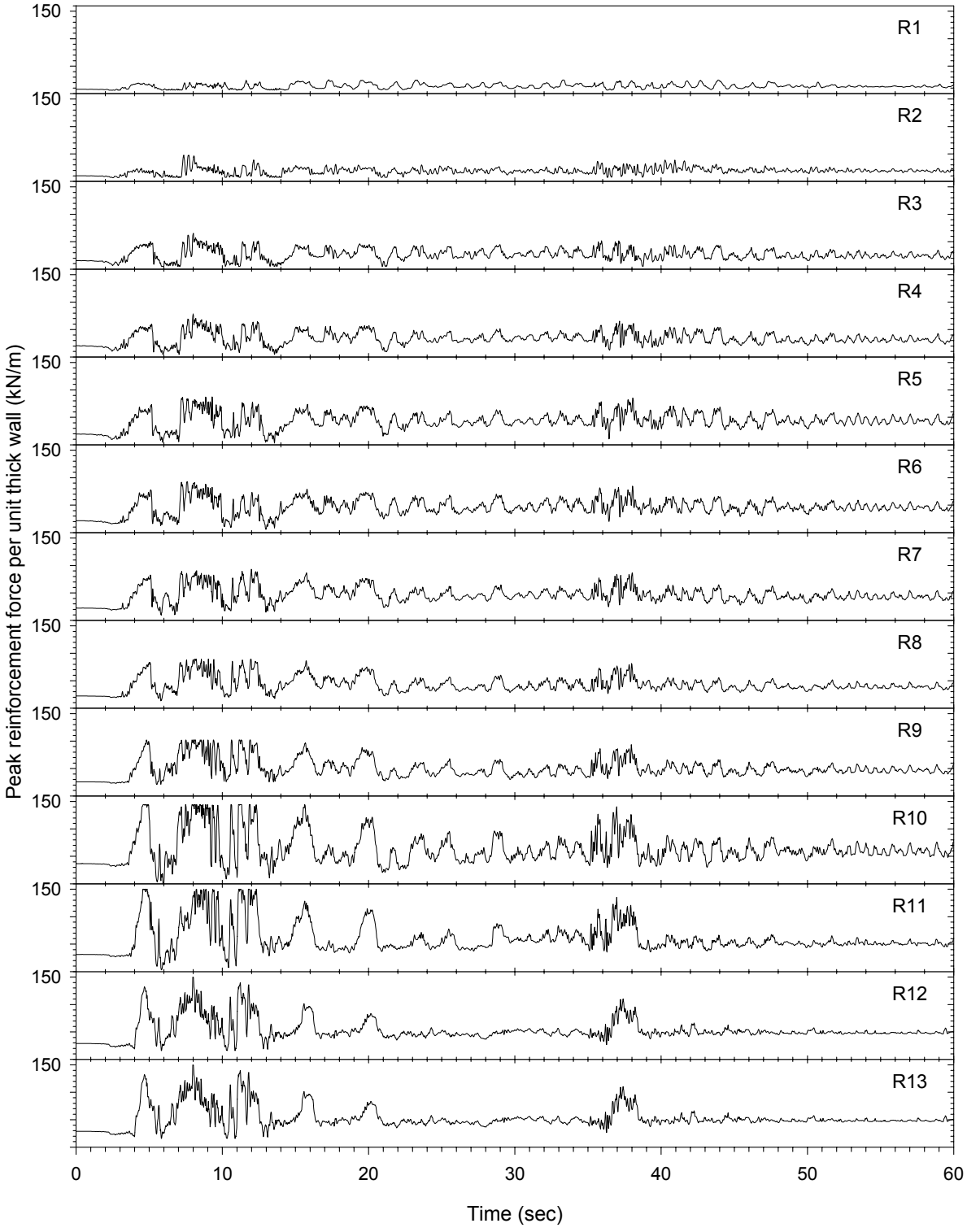


Figure 2-79. Peak reinforcement forces throughout shaking – right wall

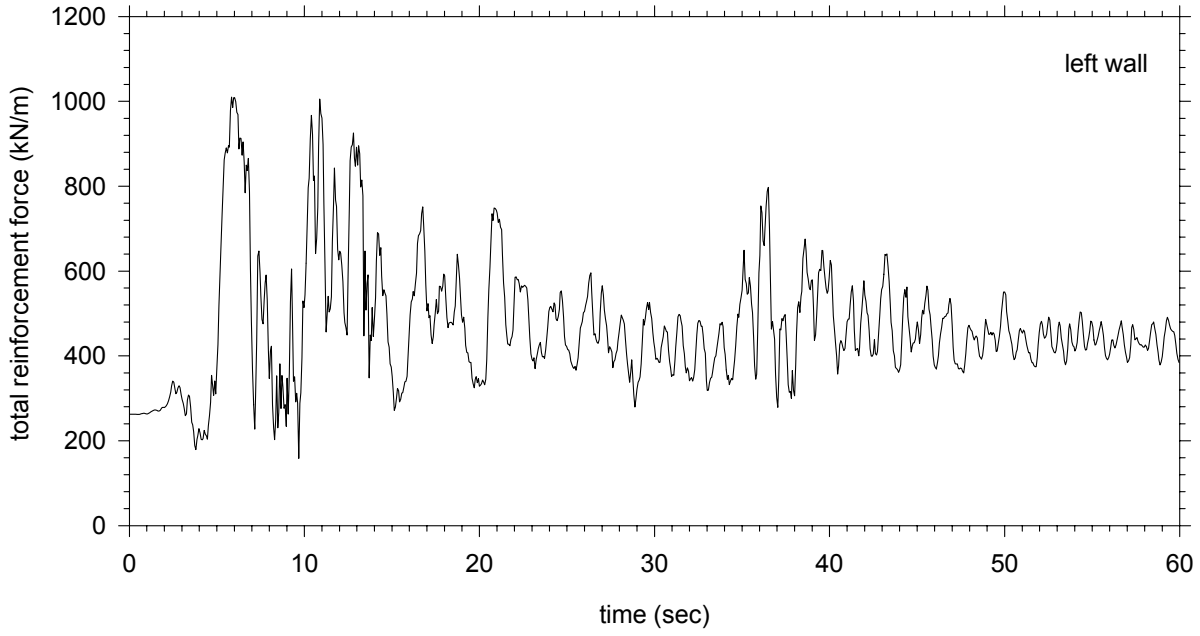


Figure 2-80. Total reinforcement force during shaking – left wall

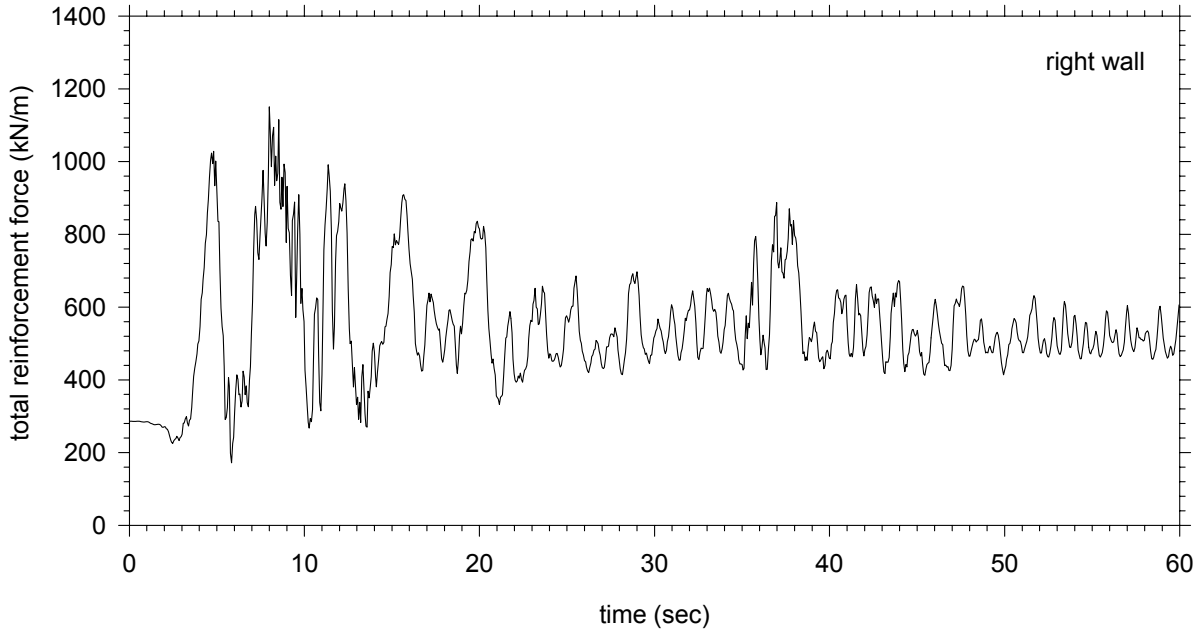


Figure 2-81. Total reinforcement force during shaking – left wall

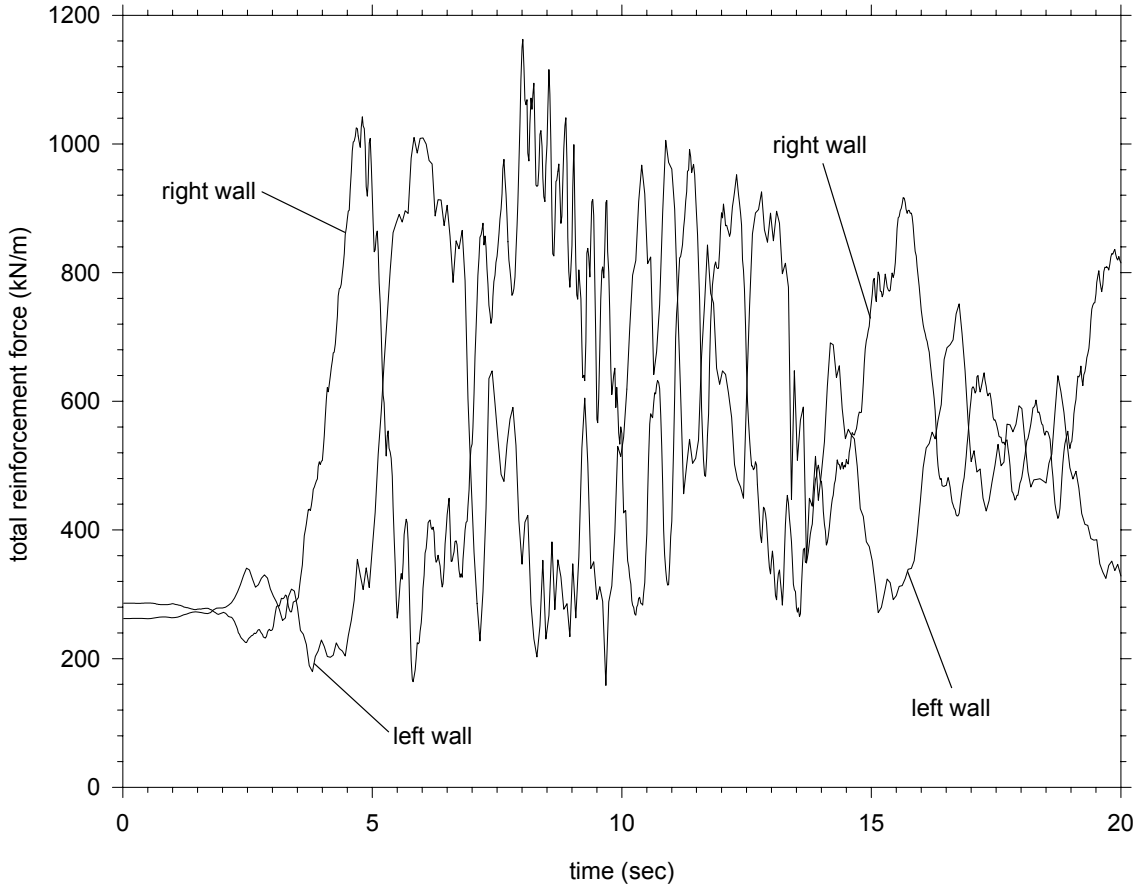


Figure 2-82. Total reinforcement force during shaking. Left and right wall forces compared to present how they are phased in time. Shaking in one direction increases the forces in that direction whereas the forces in the opposite wall are reduced.

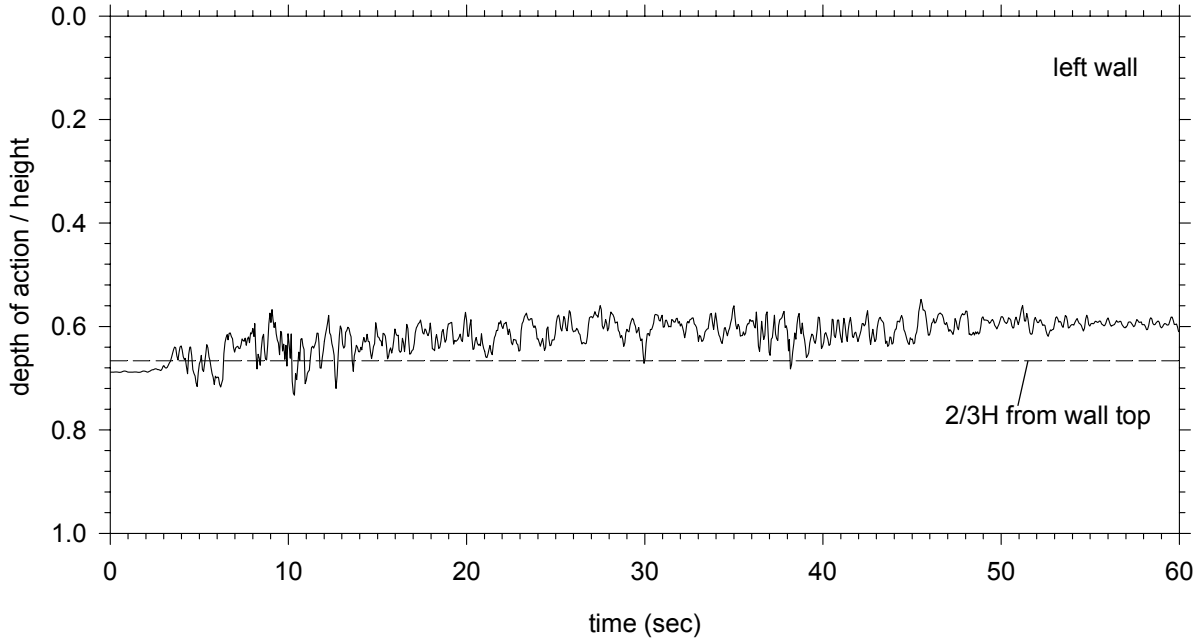


Figure 2-83. Equivalent location of action of the total reinforcement force – left face.

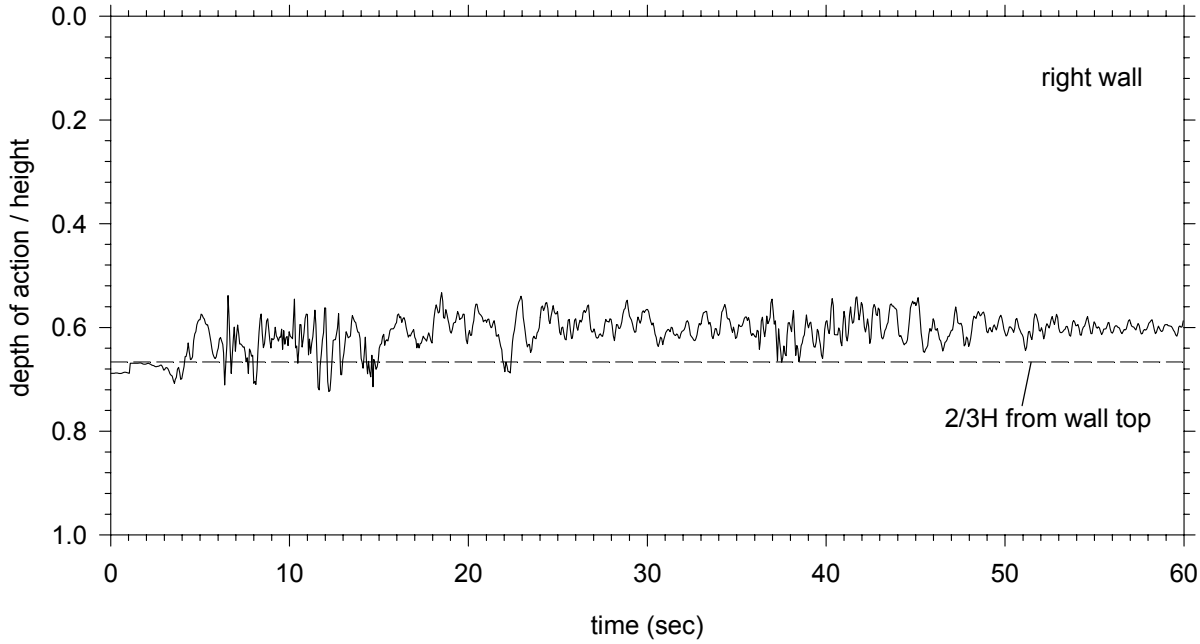


Figure 2-84. Equivalent location of action of the total reinforcement force – left face.

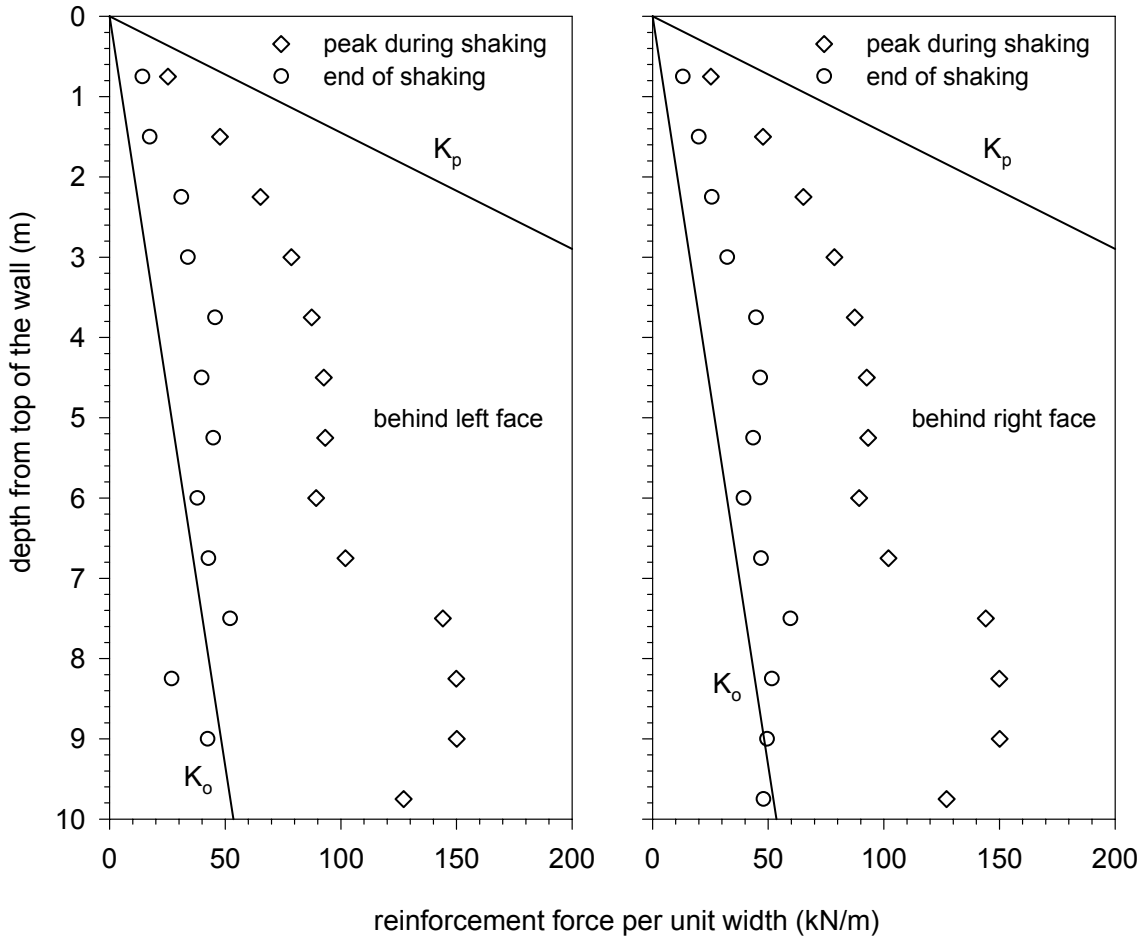


Figure 2-85. Reinforcement forces at left and right facing. Peak values and end-of-shaking in comparison to the reinforcement values that correspond to at-rest earth pressure and passive earth pressure conditions.

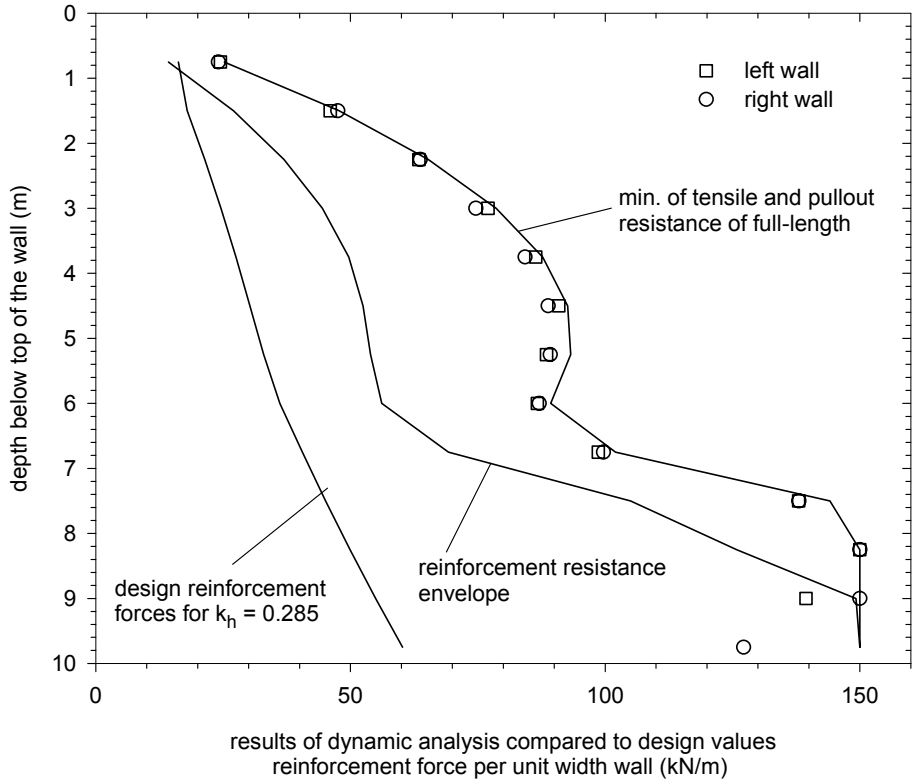


Figure 2-86. Computed peak reinforcement forces in comparison to design values

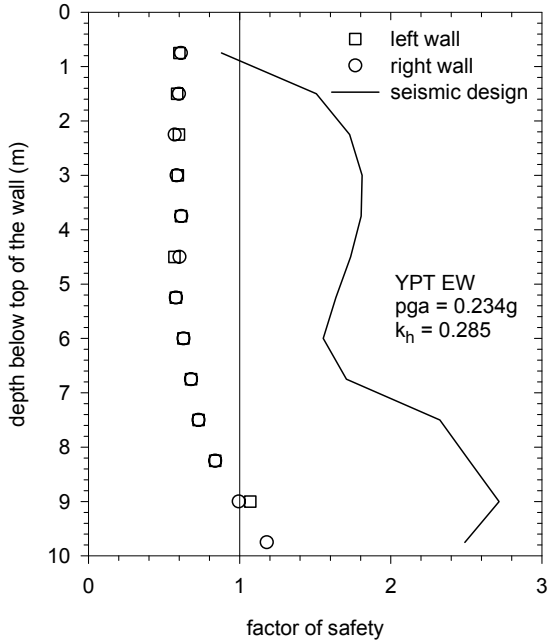


Figure 2-87. Seismic factor of safety – Design values and computed

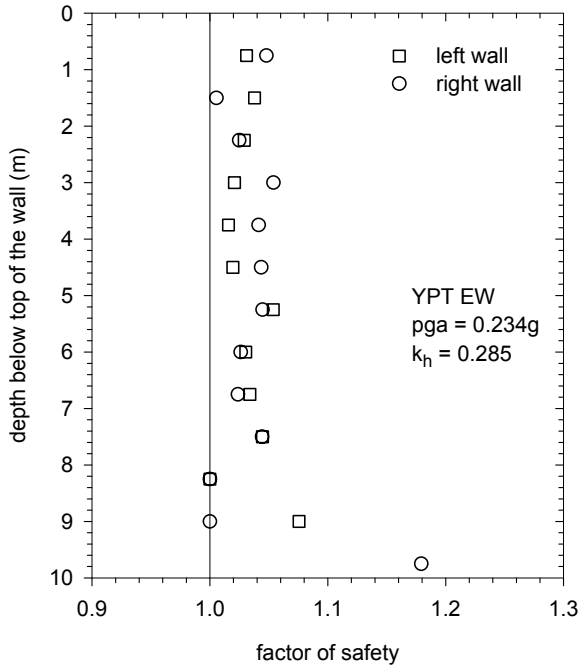


Figure 2-88. Seismic factor of safety calculated from computed peak reinforcement force and ultimate resistance envelope

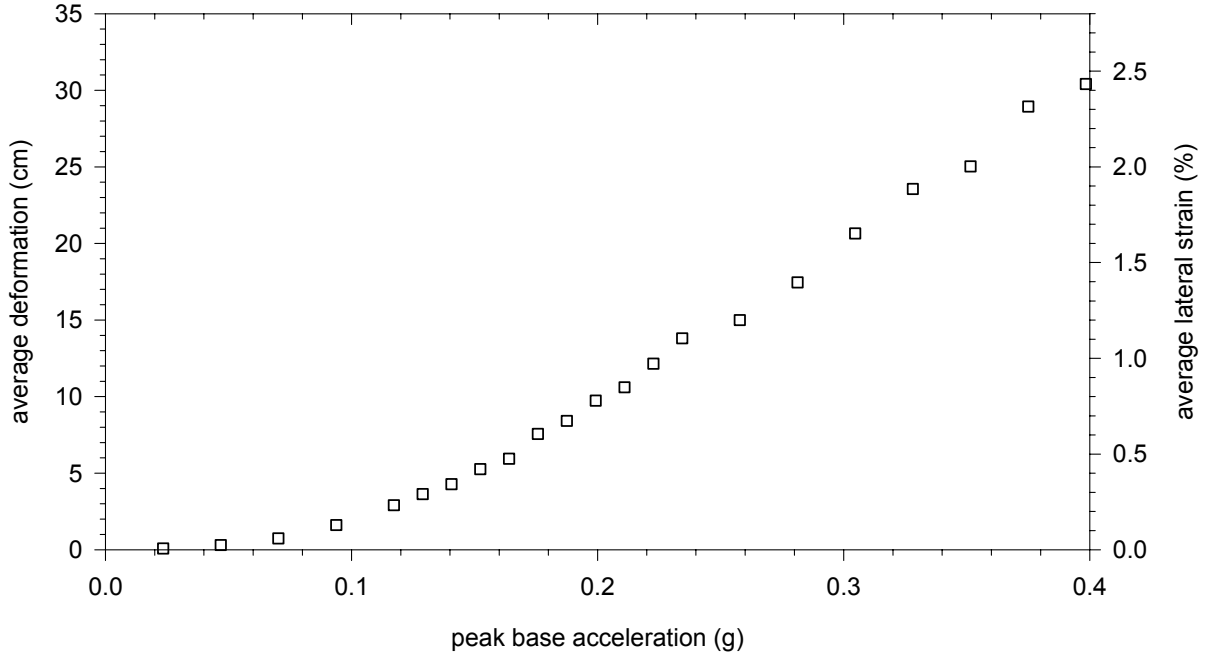


Figure 2-89. Average deformation and peak base acceleration – YPT EW

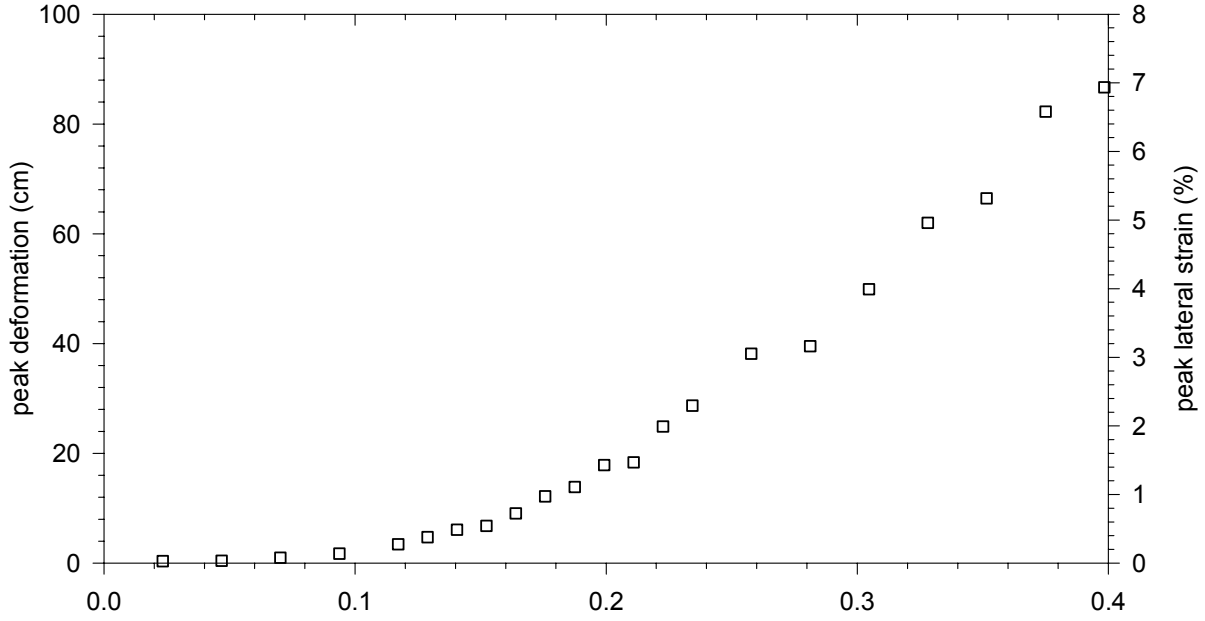


Figure 2-90. Peak deformation and peak base acceleration – YPT EW

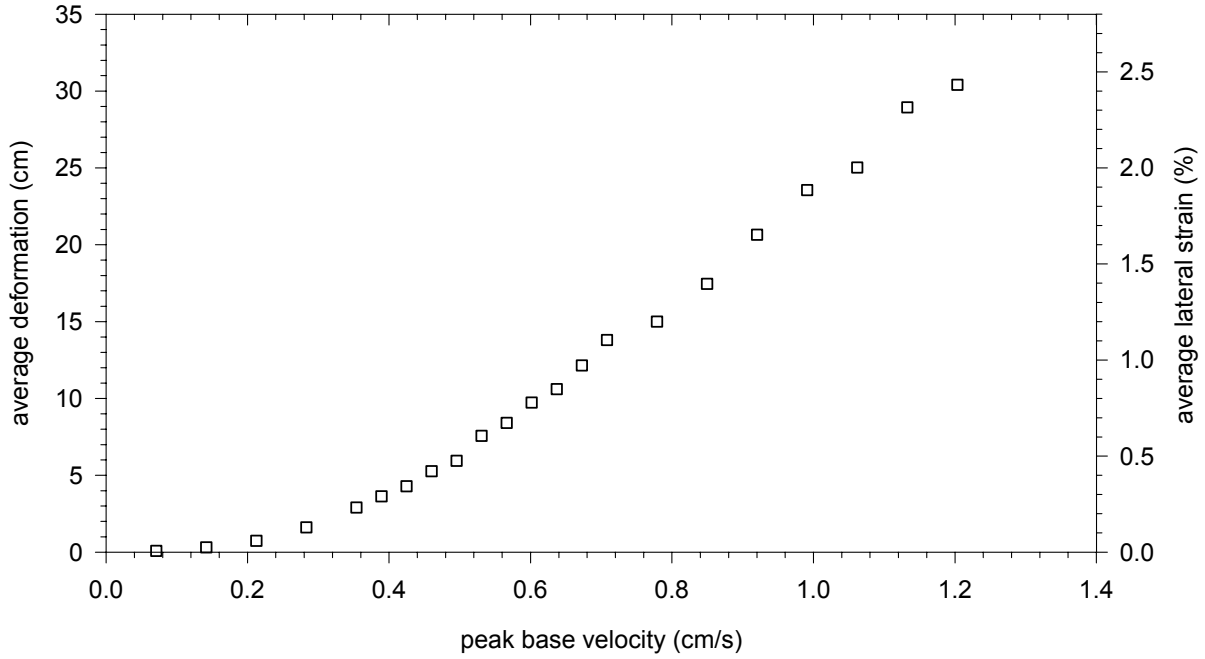


Figure 2-91. Average deformation and peak base velocity – YPT EW

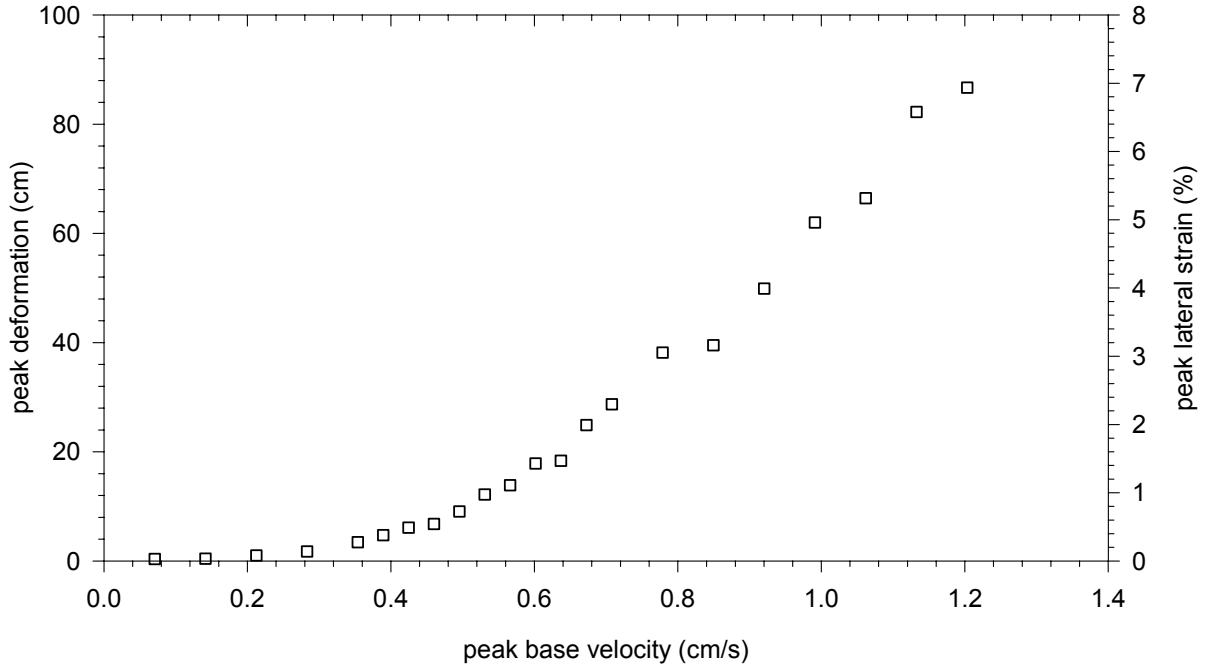


Figure 2-92. Peak deformation and peak base velocity – YPT EW

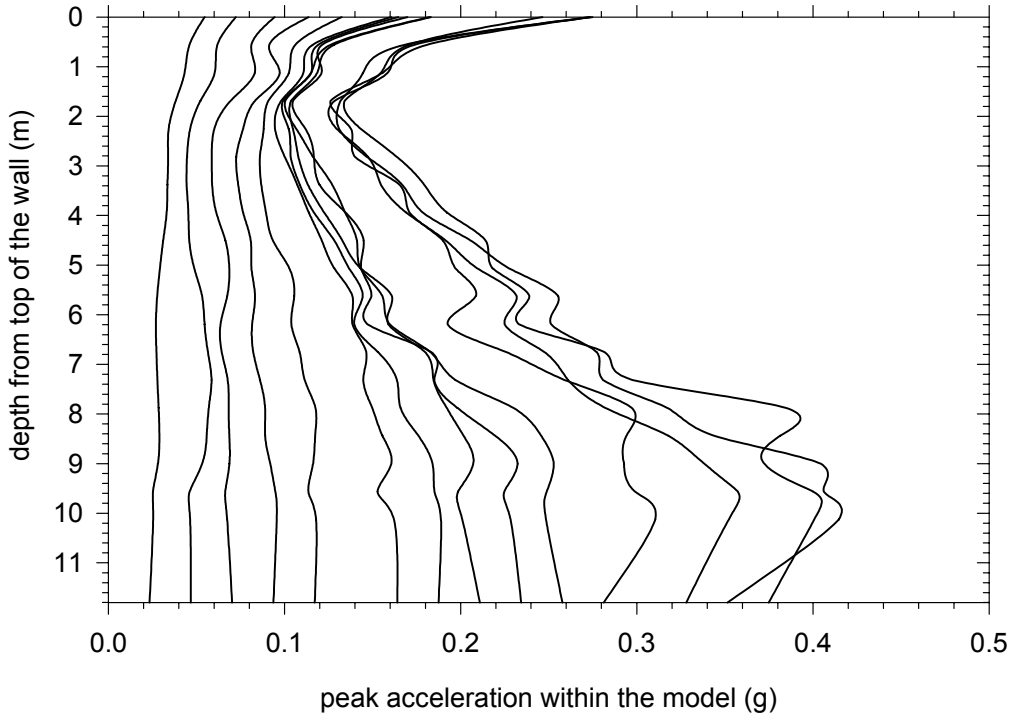


Figure 2-93. Variation of peak acceleration within the wall for different acceleration levels

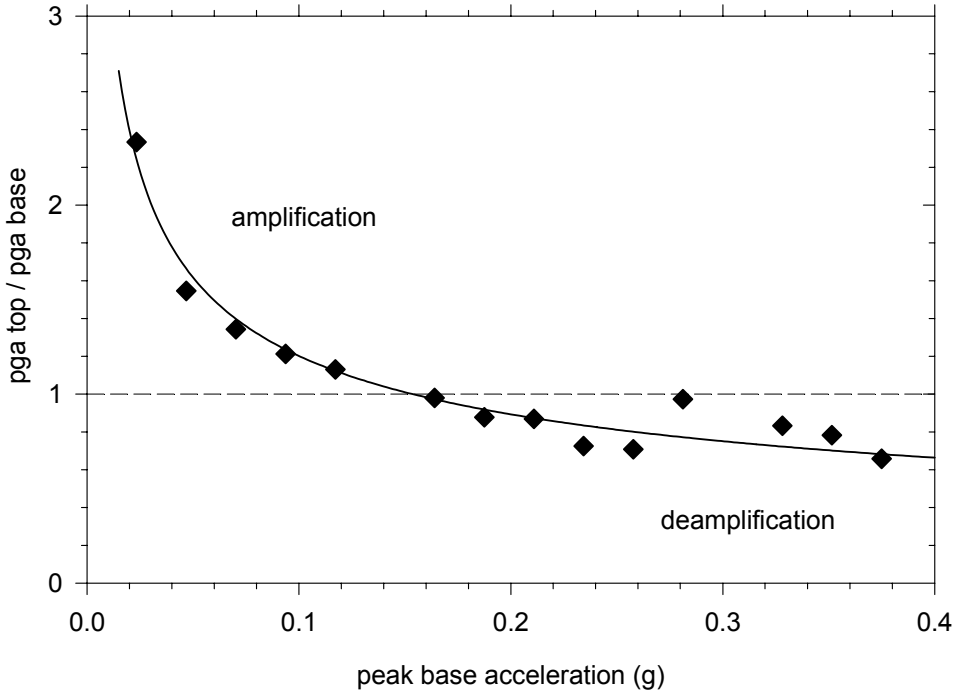


Figure 2-94. Ratio of peak acceleration at the top to the peak acceleration at the base

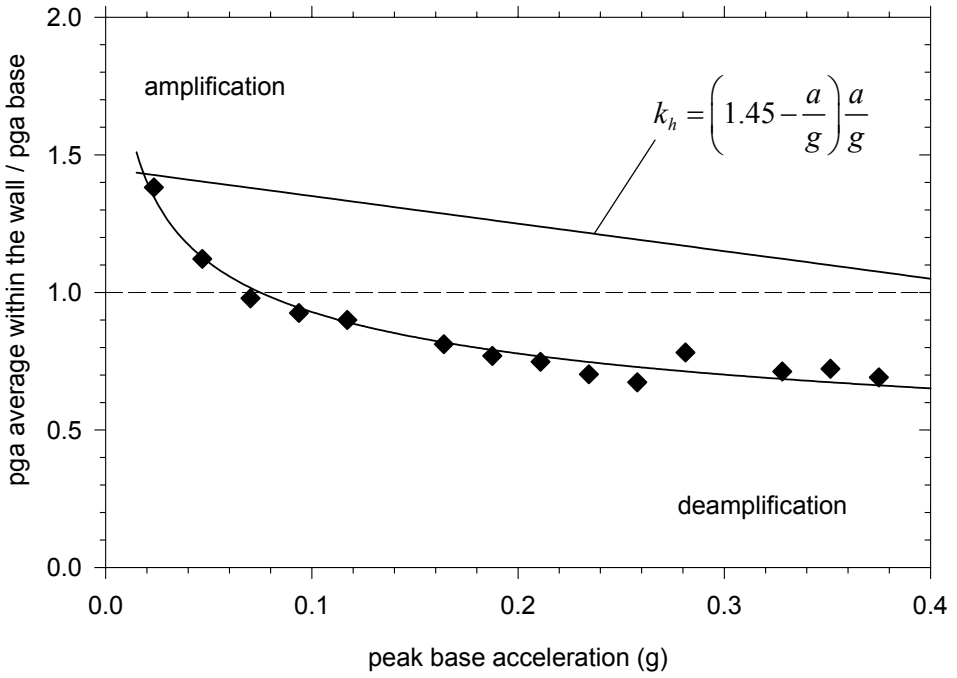


Figure 2-95. Ratio of average acceleration within the wall to the peak acceleration at the base

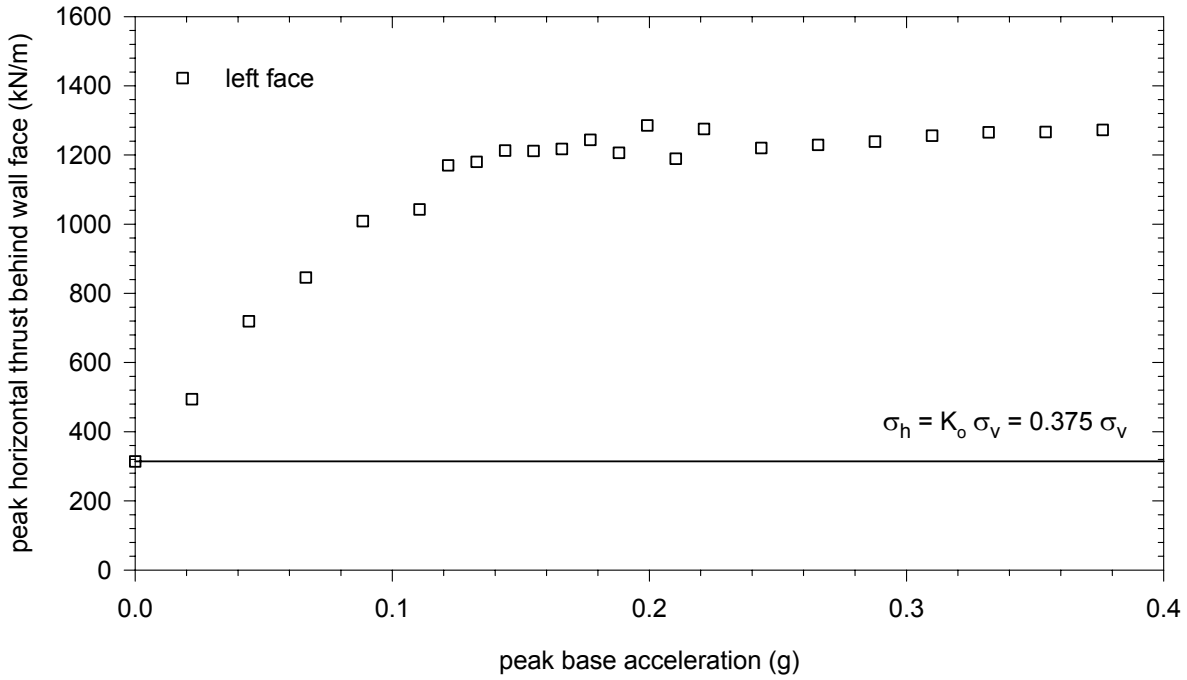


Figure 2-96. Peak horizontal thrust behind left face with respect to peak base acceleration

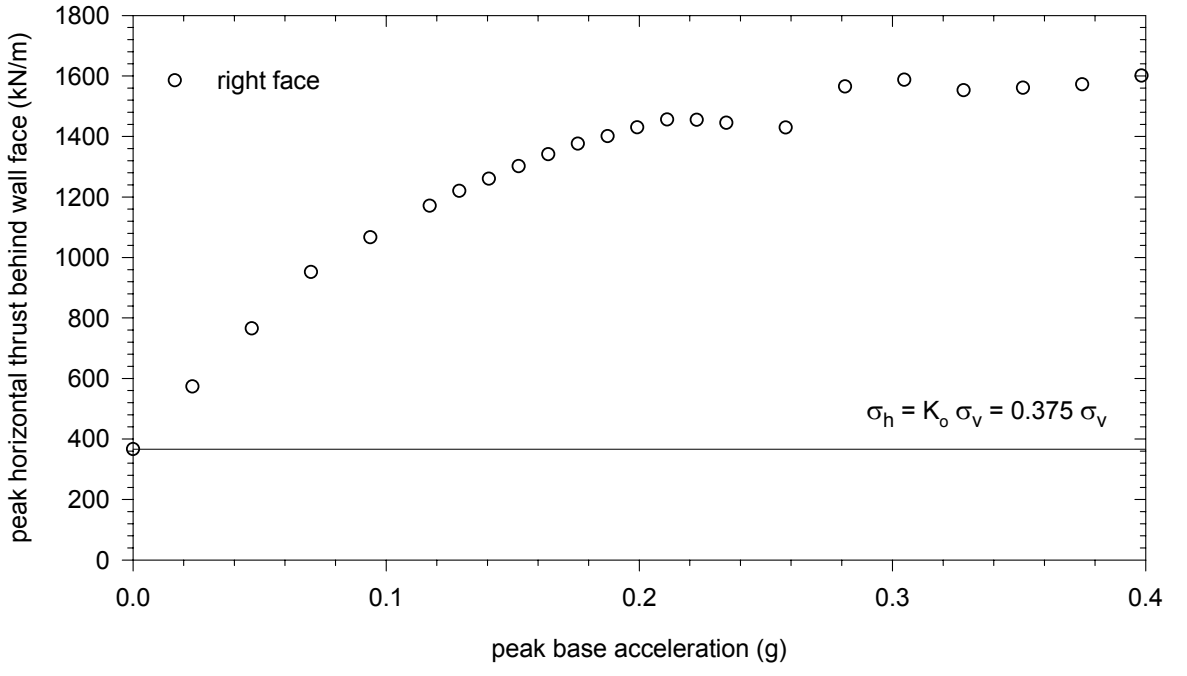


Figure 2-97. Peak horizontal thrust behind right face with respect to peak base acceleration

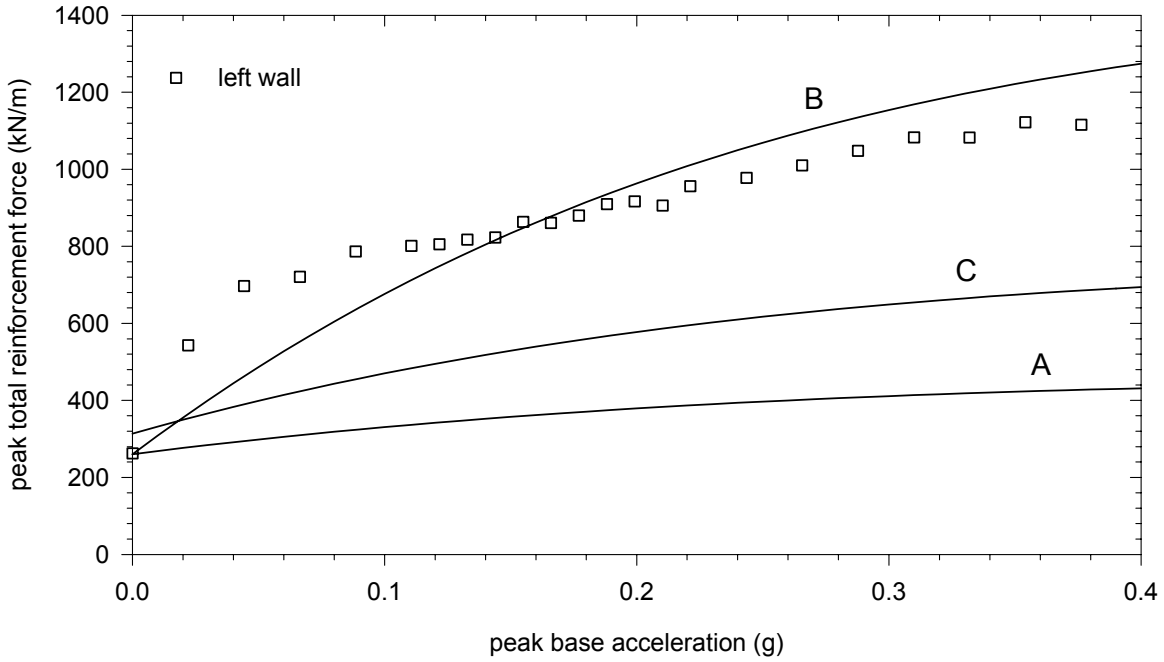


Figure 2-98. Peak total reinforcement force and peak base acceleration – left wall

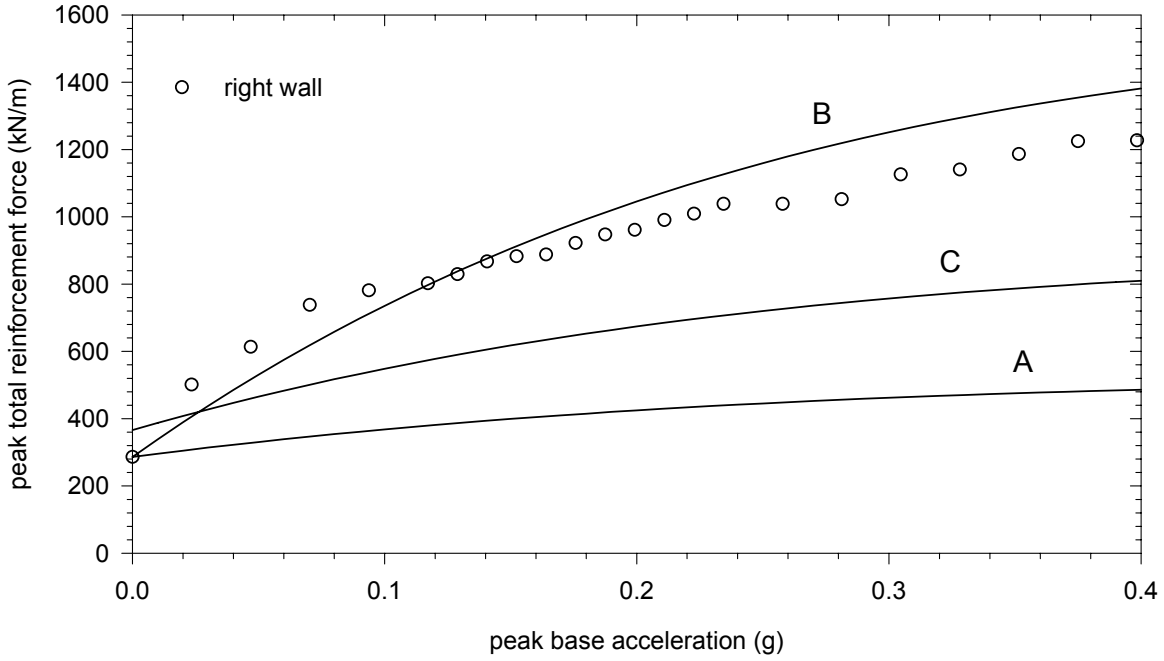


Figure 2-99. Peak total reinforcement force and peak base acceleration – right wall

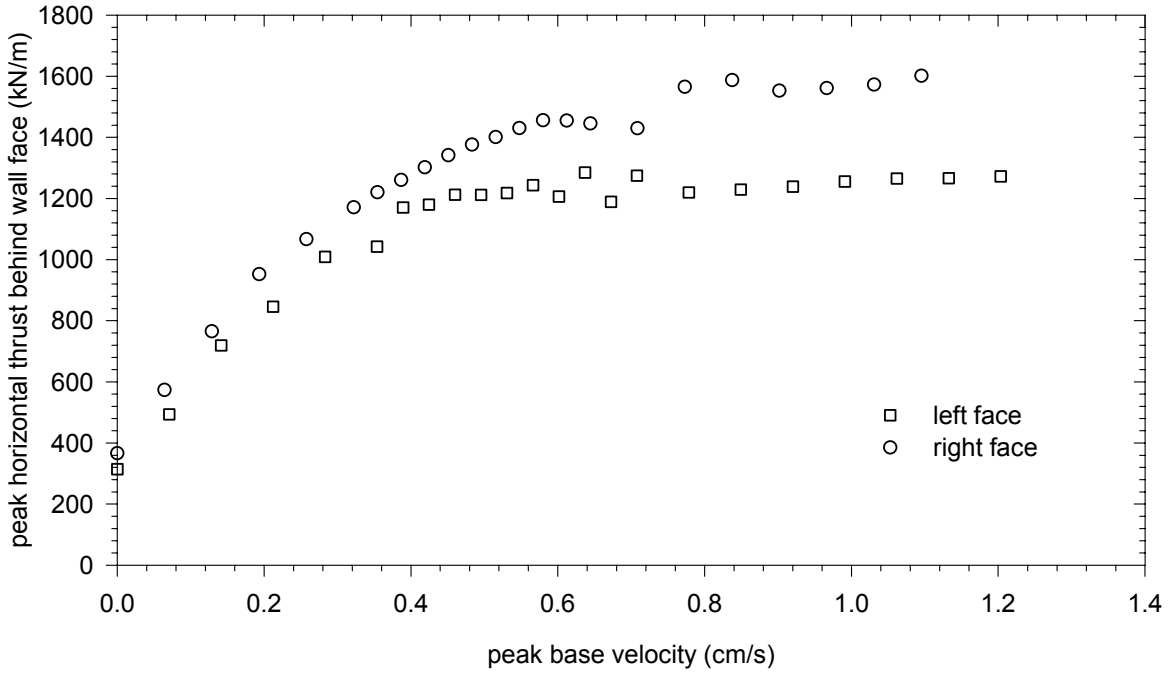


Figure 2-100. Peak horizontal thrust behind wall face with respect to peak base velocity

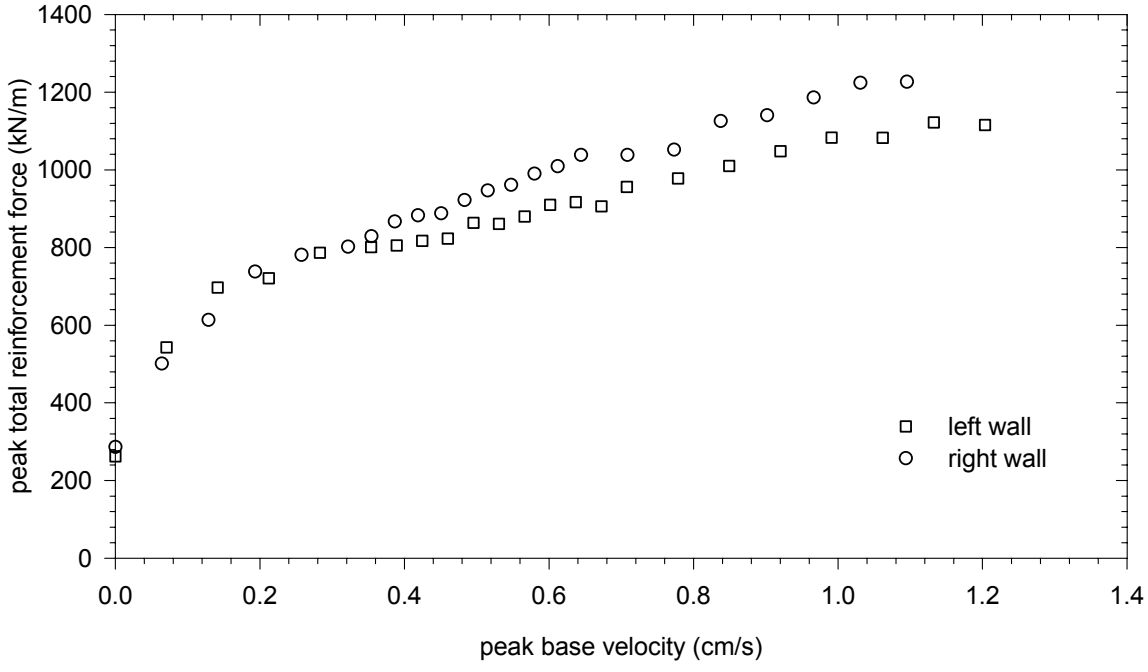


Figure 2-101. Peak total reinforcement force with respect to peak base velocity

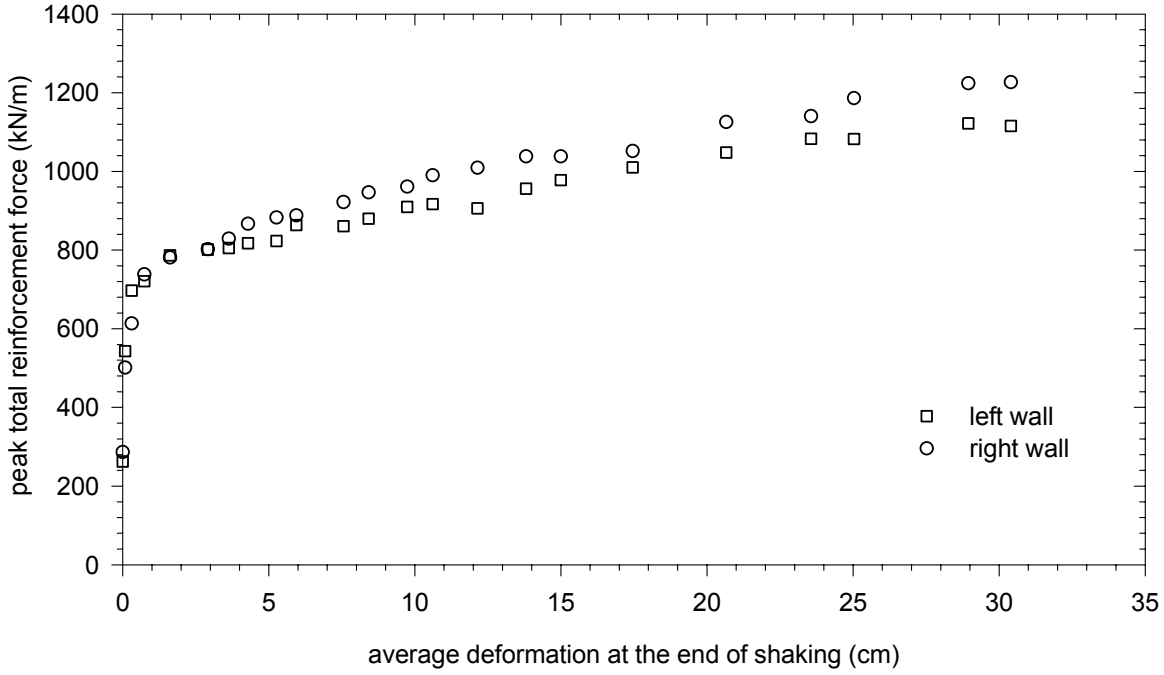


Figure 2-102. Peak total reinforcement force with respect to average deformation

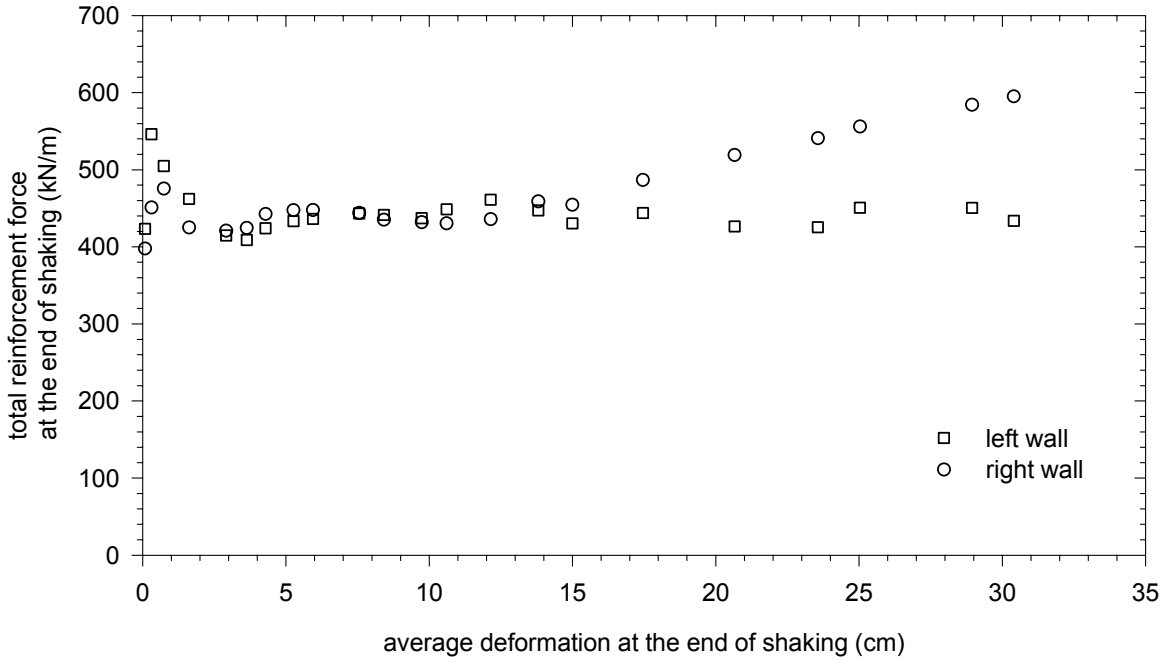


Figure 2-103. Total reinforcement force at the end of shaking with respect to average deformation

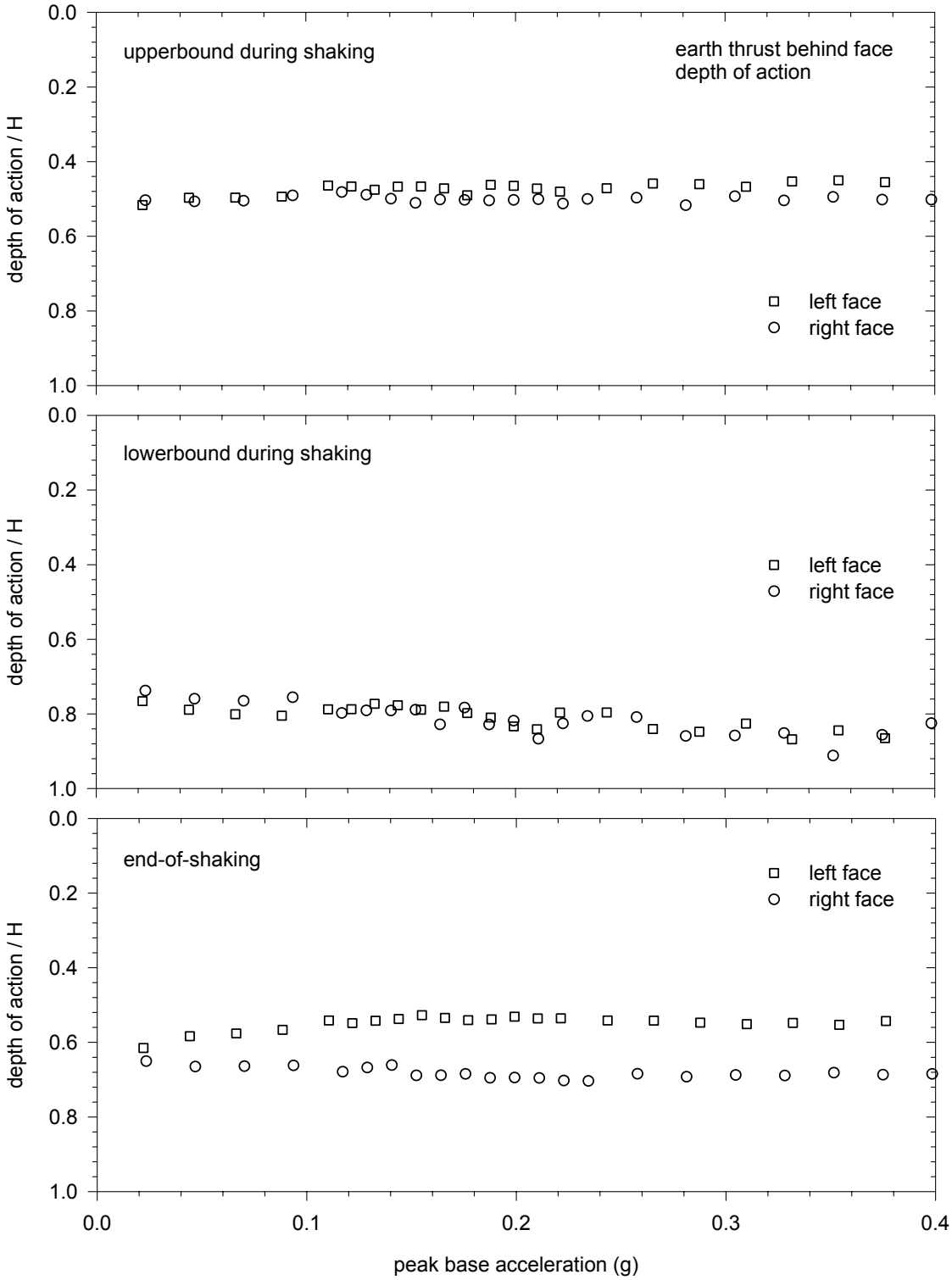


Figure 2-104. Location of action of equivalent horizontal earth thrust – depth from top of the wall. Upper and lower bound limits during shaking and end-of shaking values.

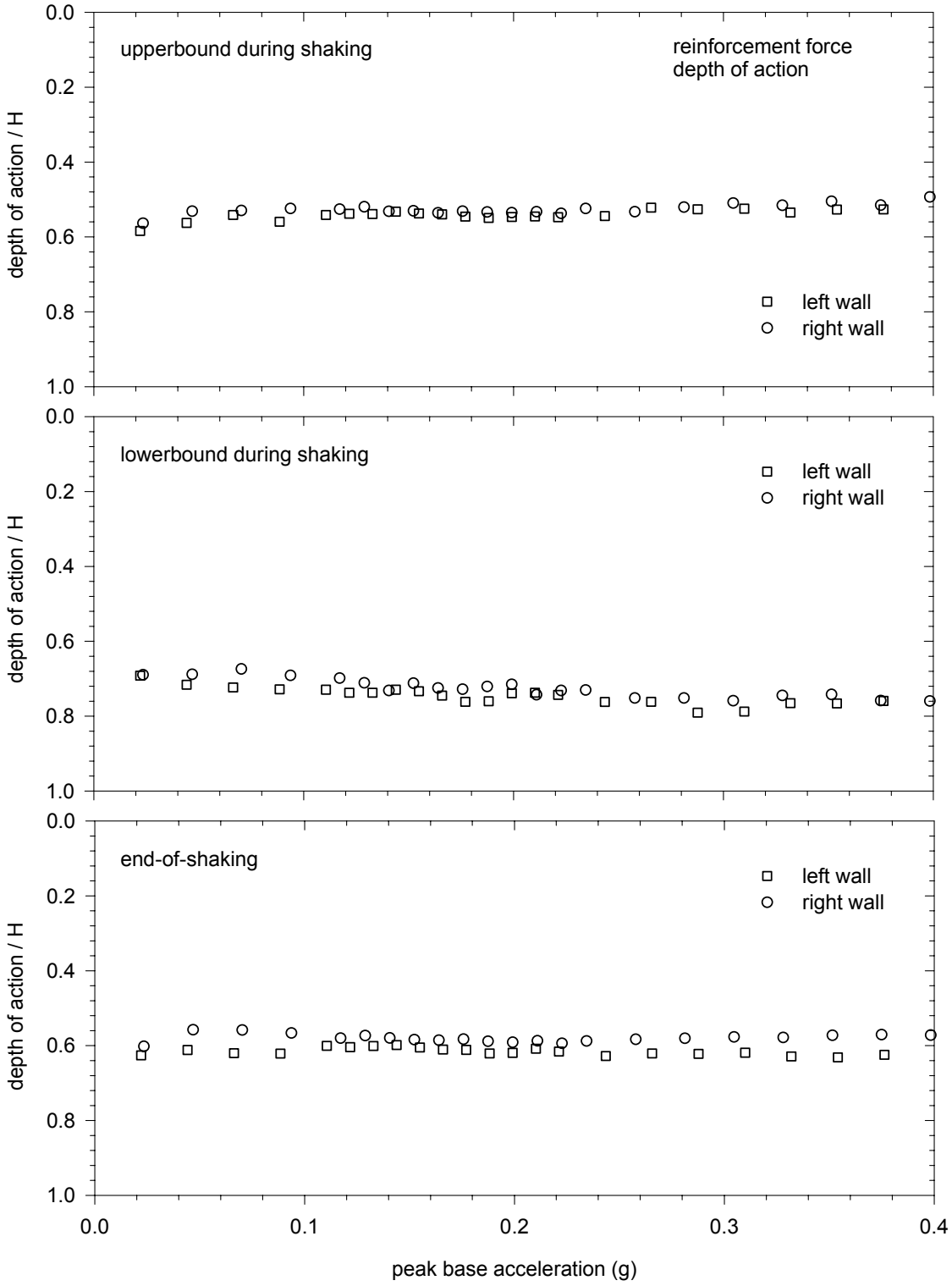


Figure 2-105. Location of action of equivalent total reinforcement force – depth from top of the wall. Upper and lower bound limits during shaking and end-of shaking values.

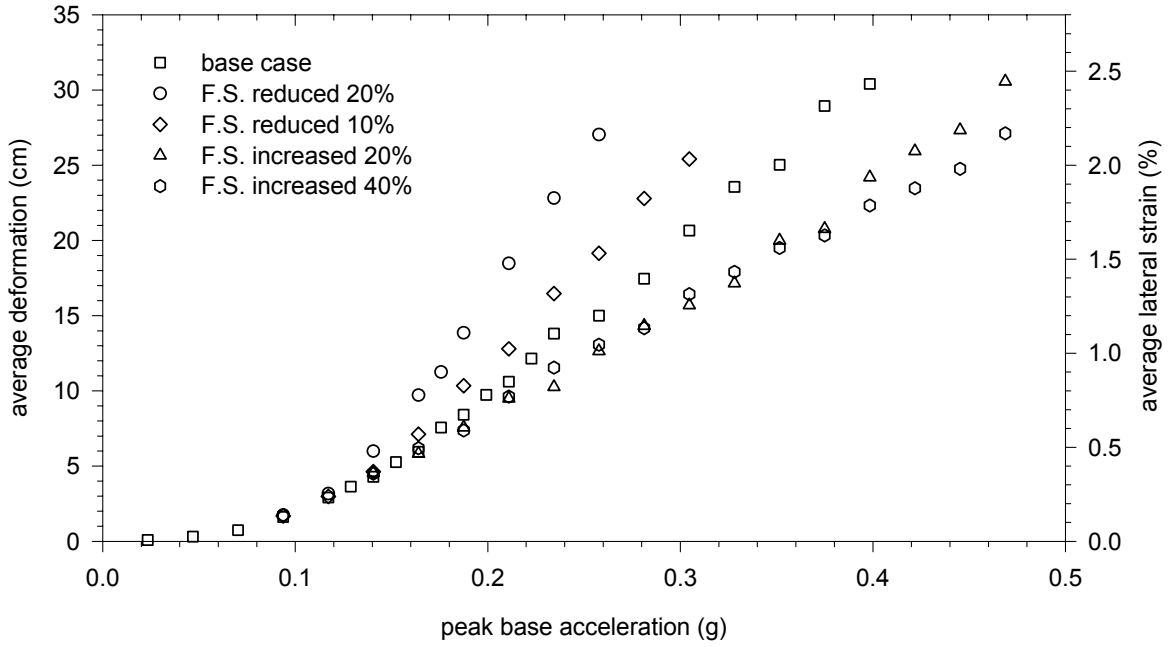


Figure 2-106. Average deformation with respect to peak base acceleration for models with different factors of safety

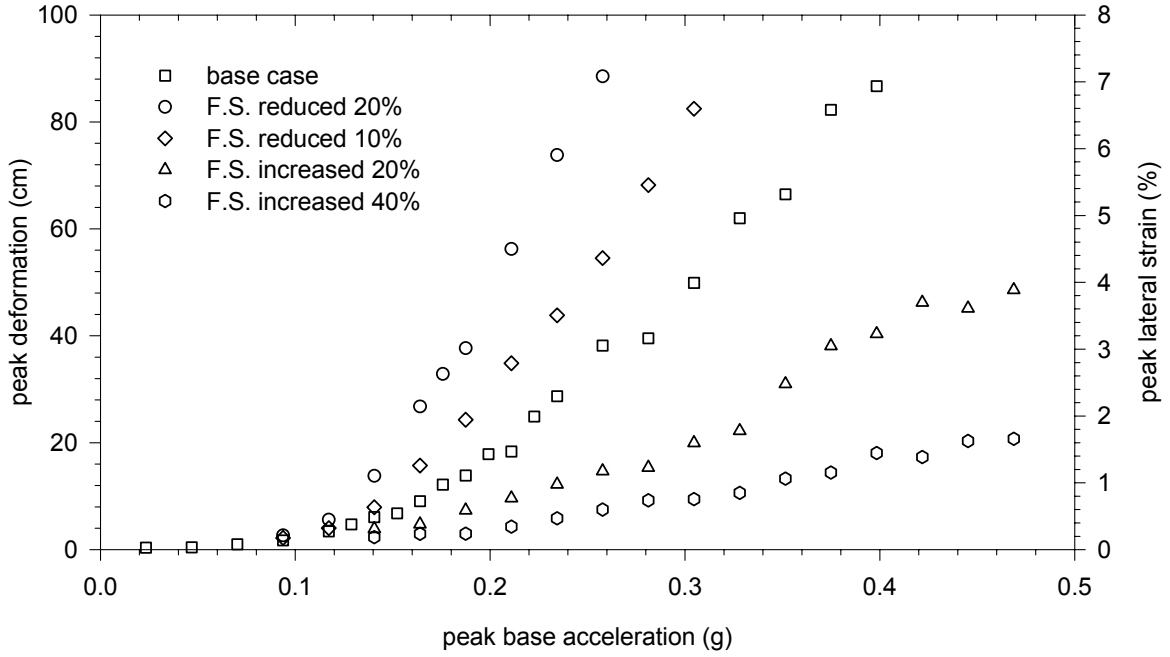


Figure 2-107. Peak deformation with respect to peak base acceleration for models with different factors of safety

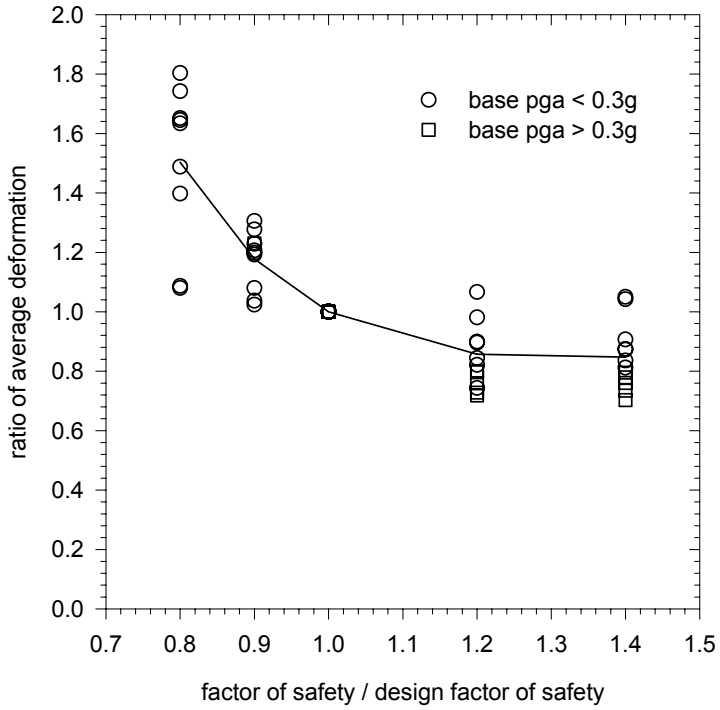


Figure 2-108. Ratio of average deformation for different safety factors

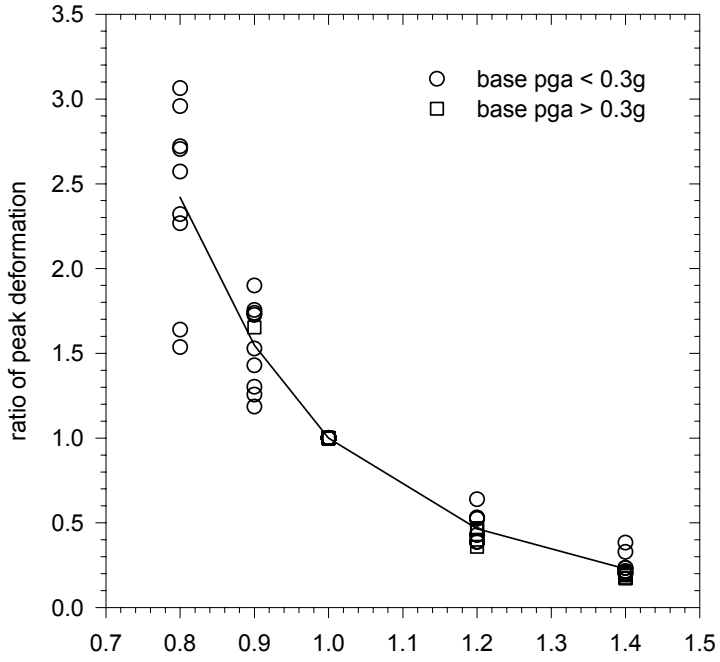


Figure 2-109. Ratio of peak deformation for different safety factors